Quantum-Enhanced Measurements with Atoms in Cavities: Superradiance and Spin Squeezing

by

Kevin C. Cox

B.S., College of William and Mary, 2011

M.S., University of Colorado, 2014

A thesis submitted to the

Faculty of the Graduate School of the

University of Colorado in partial fulfillment

of the requirements for the degree of

Doctor of Philosophy

Department of Physics

2016

This thesis entitled:
Quantum-Enhanced Measurements with Atoms in Cavities: Superradiance and Spin Squeezing
written by Kevin C. Cox
has been approved for the Department of Physics

_____

Prof. James K. Thompson

_____

Prof. Jun Ye

Date _____

The final copy of this thesis has been examined by the signatories, and we find that both the content and the form meet acceptable presentation standards of scholarly work in the above mentioned discipline.

Cox, Kevin C. (Ph.D., Department of Physics)

Quantum-Enhanced Measurements with Atoms in Cavities: Superradiance and Spin Squeezing

Thesis directed by Prof. James K. Thompson

Advances in engineering quantum systems are expected to lead to a new generation of quantum technology with fundamentally new capabilities and no classical analogue. Specifically, in the near future, quantum entanglement may become useful for enhancing state-of-the-art atomic clocks and sensors. I have performed experiments using laser-cooled rubidium atoms trapped in a high finesse optical cavity to explore quantum and collective enhancements to precision measurements.

In this thesis, I will present a recent experiment to create record amounts of entanglement-enhancement, or spin squeezing, in a proof-of-principle atomic sensor using entanglement-generating collective measurements. We have demonstrated up to a factor of 60 in directly observed spin squeezing beyond the standard quantum limit for an unentangled quantum sensor and have demonstrated squeezing with real-time feedback to create deterministic entangled states. Second, I will present a new method that has generated over a factor of 10 in homogeneous entanglement that could be resolvable in free-space quantum sensors such as matter-wave interferometers and discuss a new method to reduce errors in manipulating collective spin states using reversible dephasing. These experiments and methods are directly applicable to some of the world's best optical lattice clocks such as those housed here at JILA and NIST.

In addition, I have studied and demonstrated a proof-of-principle superradiant laser that relies on collectively enhanced laser emission. These lasers have the potential to realize state-of-the-art frequency purity useful for optical atomic clocks and long baseline interferometry. I will discuss an experiment that demonstrates injection locking of a superradiant laser for the first time as well as explores the collective synchronization behaviors in the system. This study of synchronization informs research on current and future narrow linewidth superradiant lasers and may also provide a platform for future studies of quantum phase transitions in open quantum systems.

Dedication

To Caitie, love beyond measure.

Acknowledgements

I have had a truly wonderful experience working in JILA. Working in the Thompson group has been exciting, challenging, nurturing, friendly, professional, and fun. Thank you James for being patient and kind in addition to being a world class physicist. It makes all the difference. Thank you to all the great labmates I have had over the years: Zilong, Justin, Josh, Matt, Graham, and Baochen. There are few places where one can find such excellent people to work with. Thank you Hans Green, Terry Brown and the other shop workers who are always willing to help students. I believe you are a big part of what makes JILA work.

Thank you to Mom and Dad for all the love and support over the last five years.

Once again, specific thanks to James Thompson, Justin Bohnet, Josh Weiner, Matt Norcia, Graham Greve, and Baochen Wu, who have all been primary contributors to the work herein.

Contents

Chapter

Appendix

Tables

Table

Figures

Figure

Chapter 1

Motivation and Introduction

1.1   Quantum capability

We already live in a world full of quantum technology. The development of quantum physics has lead to a rich and detailed understanding of atoms, solids, light, electricity, and magnetism: quantum building blocks that are essential for many modern devices. Computers, lasers, and advanced materials, to name a few, would not exist without modern quantum understanding.

On the other hand, even without modern quantum physics, the majority of modern technologies *could, in principle*, be realized through strictly "classical" means. For example, consider a transistor, the basic element of modern computers. Transistors are quantum devices made of joined semiconducting materials that display non-linear conduction versus applied voltage due to the structure of the available quantum energy levels in the solid. Despite this, transistors can be viewed simply as switches or amplifiers. Their relevant logical behavior can be achieved using components that are adequately explained without quantum mechanics. A fully "classical" computer, for example, that can calculate difficult polynomials was suggested by Charles Babbage in the 1800's and has since been built with Lego children's toys [37], a sufficiently classical infrastructure.

Quantum technologies with no classical analogue are difficult to find. This fact leads to an important broad question that motivates research in every sub-field of quantum science: What are the intrinsic capabilities of quantum systems? Researchers in quantum computing, for example, study which types of problems quantum computers can solve efficiently [126]. A large body of research is also aimed at understanding errors that occur in quantum objects or information and

how to control and correct them [153]. The Nobel prize was even awarded this year for the study of exotic phases exhibited by quantum matter, how they behave, and how they could be useful one day.

The question of quantum capability also forms a central theme for this thesis. Specifically, I will explore how quantum physics both limits and improves precision measurements.

1.2   Quantum certainty and uncertainty

Perhaps the most powerful, yet often under appreciated feature of quantum systems is their certainty or "identicality". Two ^{87}Rb atoms (the atoms used in this thesis) are identical. One can build two atomic clocks on opposite sides of the world and be certain that, given an ideal apparatus, they would tick at exactly the same rate. Atoms are so identical that when one considers a quantum wave function describing their behavior, the wave function fundamentally must have very specific symmetry when the particles are exchanged with one another.

Quantum identicality is the primary power of atomic clocks and quantum sensors that perform the most precise absolute measurements in the world [115, 66, 162]. I would argue that such devices are indeed a truly useful quantum technology with no classical analogue because their unmatched measurement precision is a direct outcome of quantum certainty. Similarly, in Section 1.3.2 and Chapter 3 of this thesis I will describe experiments to demonstrate a proof-of-principle superradiant laser that relies on the quantum identicality of the atomic gain medium to achieve a high degree of frequency purity. Superradiant lasers may one day be able to surpass the frequency purity of the current state-of-the-art lasers based on manmade reference cavities.

Quantum identicality comes with a price. For any quantum sensor, random collapse of the atom's, ion's, or photon's wave-function leads to uncertainty in the final readout of that sensor. This means that many identical quantum particles must be used to average down quantum uncertainty. Quantum noise is the "yang" to the identicality "yin".

Quantum sensors based on 2-level qubits work much like flipping coins. By flipping N coins, one can measure the error E in the coins' probability $E = P_H - P_T$ where P_H is the probability

for the coin to land on heads and P_T is the probability for the coin to land on tails. I assume that the coins are nearly fair ($E \approx 0$), but small biases could be detected around $E = 0$. Flipping a single coin would be a poor measurement of E. But by flipping many coins, an estimate of E, that I label $\tilde{E}$, can be obtained using the equation $\tilde{E} = (N_H - N_T)/N$ where N_H is the number of coins that landed in heads and N_T is the number that landed on tails. The error in this estimate can be shown to be, $\Delta\tilde{E} = 1/\sqrt{N}$ where ΔX refers to the standard deviation in the quantity X. This coin-flip noise is a classical analogue of the quantum noise that plagues quantum sensors.

For real atoms or qubits with two quantum states labeled $|\uparrow\rangle$ and $|\downarrow\rangle$, quantum collapse into $|\uparrow\rangle$ or $|\downarrow\rangle$ leads to uncertainty in measuring the quantum phases θ and ϕ in the superposition $|\psi\rangle = \cos(\theta/2)|\uparrow\rangle + \sin(\theta/2)e^{i\phi}|\downarrow\rangle$. A quantum sensor operates by biasing the probability in the angles θ or ϕ based on a measured quantity such as time, gravity, or electric or magnetic fields. For N unentangled atoms identically prepared in state $|\psi\rangle$, the random collapse of each atom causes an uncertainty in an estimate of θ and ϕ known as the standard quantum limit (SQL) $\Delta\theta_{SQL} = \Delta\phi_{SQL} = 1/\sqrt{N}$.

What would be required to to surpass the SQL in an atomic sensor? To gain insight for this process, the coin analogy still carries some insight. First, when flipping N coins with $E \approx 0$, the randomness of each coin cannot be avoided. Second, one cannot predetermine the outcome of any individual coin, because if you could, there would be no way to be sensitive to changes in E. From these two assumptions, the only way to improve the measurement of E is to engineer a non-local connection between the coins leading to correlation. If the true value that we wish to estimate is $E = 0$, then when one coin noisily lands on heads, another coin must, through the connection between the coins, know to land on tails. [1] The ability for quantum systems to display such nonlocal connection was pointed out in the famous EPR paradox [46]. Today such quantum connections, which are a manifestations of a non-factorable wavefunction, are generally referred to as entanglement. Most of this thesis deals with creating large amounts of quantum entanglement

---

[1] A reduction in $\Delta\tilde{E}$ could also be explained by the coins communicating a "hidden variable", but in quantum mechanics, theories of this type can be ruled out by Bell tests [63, 65, 51, 143]

to surpass the SQL in atomic sensors.

1.3   Brief overview of this work

A simplified diagram of our experimental system is shown in Fig. 1.1. We trap and cool a cloud of ^{87}Rb atoms (red) to a temperature of 10 μK inside an optical cavity (blue) using the now-standard techniques of laser cooling and trapping. The cavity resonance frequency is tuned near an atomic transitions in ^{87}Rb, between the qubit state $|\uparrow\rangle$ and an optically excited state $|e\rangle$. In this configuration, the optical cavity has a strong rate of coupling to atoms in the excited state $|e\rangle$, so that the ensemble and cavity exchange excitations (between atomic excitations and cavity photons) at a rate of up to $\Omega = 2\pi \times 6 \times 10^8$ Hz where Ω is often called the collective vacuum Rabi frequency. In this configuration, the cavity resonance frequency is highly sensitive to the qubit state of the atoms. Atoms in $|\uparrow\rangle$ affect the cavity strongly, and atoms in $|\downarrow\rangle$ do not. By measuring changes in the resonant frequency of the cavity we can infer the total number of atoms in $|\uparrow\rangle$, and therefore the superposition angle θ, very precisely.
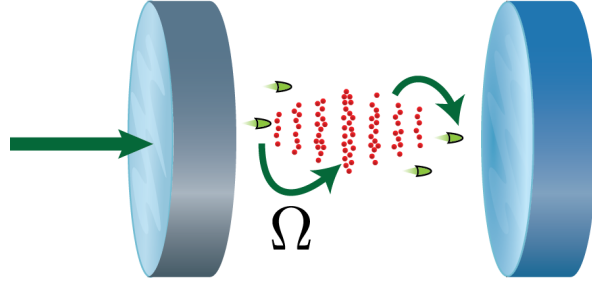
Figure 1.1: Simple experimental diagram. 10^5 to 10^6 ^{87}Rb atoms (red) are trapped in a 1D optical lattice, forming pancake-shaped layers of atoms. The atoms are cooled to 10 to 20 μK. An atomic transition is tuned near resonance with the mode of an optical cavity (blue). Collective atomic excitations and cavity excitations (green photons) are exchanged at rate Ω. By probing the optical cavity with a laser (green) we can perform precise measurements of the quantum noise of the atoms and project the ensemble into entangled states.

1.3.1   Entanglement-enhanced sensors

The majority of this thesis describes experiments to create entanglement enhancements in the atomic ensemble useful for precision measurements. By making a measurement of cavity resonance frequency we measure θ below the SQL while maintaining the quantum superposition of the atoms. By doing this, we essentially use the measured value of quantum noise in θ to subtract from subsequent measurements, allowing differential sensing in an atomic clock or sensor below the SQL. Equivalently, we can say that the first measurement projects the atoms into an entangled state that is characterized by improved resolution in the quantum angle θ. We have shown directly observed improvements in the variance in θ of up to a factor of 60 times lower than the SQL.

Although the concept of entanglement enhancements in sensors has been around for over 15 years (spin squeezing was first demonstrated in ions before the year 2000 [137, 159]), significant entanglement enhancements have been previously elusive. Figure 1.2 shows a historical perspective of directly observed entanglement enhancements, defined by $S \equiv (\Delta\theta/\Delta\theta_{SQL})^2$, usually called spin squeezing. For this data, noise subtraction was not allowed in order to highlight the actual observed sensitivity improvement relative to the SQL. The value $S = 1$ indicates no entanglement. Along with another very recent experiment [68], the enhancement observed in this thesis $S \equiv (\Delta\theta/\Delta\theta_{SQL})^2 = 59(8)$ is by far the largest entanglement enhancement observed to date in any system. This amount of squeezing, if implemented in a quantum-noise limited atomic clock or other sensor, would nominally mean that a particular quantum limited resolution could be achieved with a factor of 60 fewer atoms, or in a factor of 60 less time. Such a large enhancement establishes entanglement as a practical way to improve atomic clocks and other sensors. In addition to the generation of large amounts of spin squeezing, I will present, for the first time, a demonstration of spin squeezing with real-time feedback to a deterministic entangled state, where the result of the squeezing measurement is no longer necessary to observe entanglement. Using this real-time feedback we created one of the largest amounts of deterministic squeezing ever observed, comparable to the amounts generated by the best naturally deterministic schemes such as 1-axis twisting using

cavity feedback or collisions in an ultra-cold gas [95, 62].

Last, I will present another experiment to observe over a factor of 10 in squeezing that additionally has a homogeneous character. This squeezing, while still one of the largest enhancements ever observed, could also be used in free space measurements such as matter wave interferometers used for tests of gravity [135], Lorentz invariance [141], inertial sensing [9], probes of new physics [131, 61], and potentially as gravitational wave detectors [54].
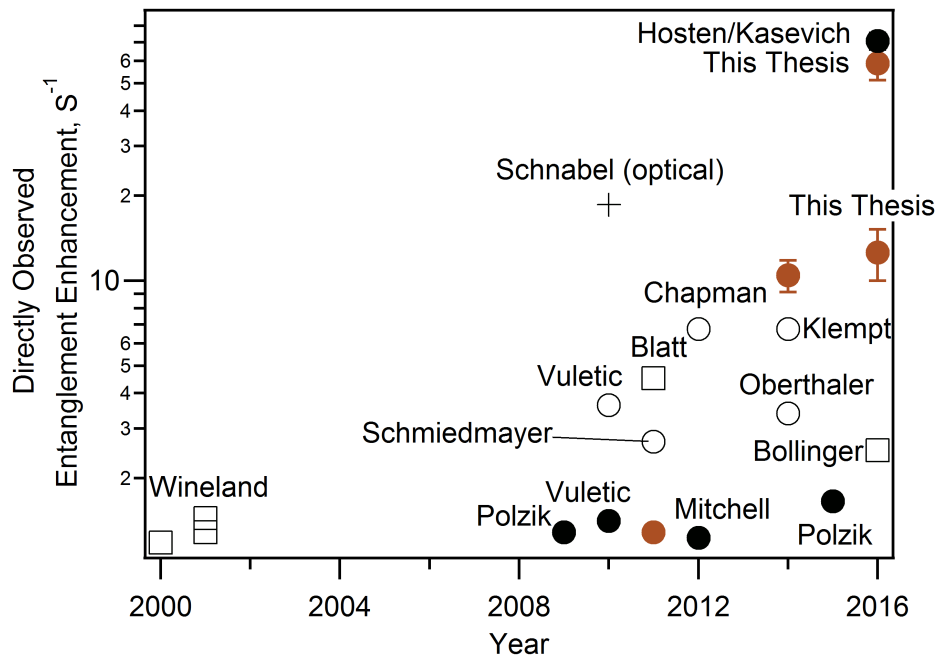
Figure 1.2: History of observed squeezing. Results from the Thompson lab are shown in brown [39, 40, 42, 31]. Experiments using collective measurements are shown as solid circles [68, 4, 142, 180, 164]. Experiments using other schemes with neutral atoms (non-linear Hamiltonians from collisions or cavity feedback) are shown as open circles [62, 101, 95, 114, 28]. Experiments with ions are shown as open squares [111, 113, 92, 93, 24]. The largest observed squeezing in an optical field is shown as a cross [163].

1.3.2   Superradiant Lasers

As well as creating a proof-of-principle entanglement-enhanced sensor, I have also worked on experiments to demonstrate cold-atom based superradiant lasers. Lasers are the best rulers for both space and time. Lasers have not only become ubiquitous in everyday life but are also used for

some of the most precise measurements in the world, including gravitational wave interferometers [1] and optical atomic clocks [115].

The most frequency-precise laser beams are formed by actively stabilizing the frequency of a laser to an optical reference cavity [77]. The primary limit to these classical, manmade length references has been thermal, Brownian motion of particles on the mirror surface that create fluctuations in the cavity's length and therefore impose fluctuations on the laser's frequency. Engineering more stable reference cavities remains a major effort to improve atomic clock performance [77].

As previously mentioned in Section 1.2, the motivation behind cold-atom superradiant lasers is to replace these manmade length/frequency references with nature's identical quantum frequency references, atoms. This can be accomplished by building a laser where the gain medium is a laser-cooled ensemble of atoms with a narrow optical transition such as strontium or ytterbium [108, 122, 120]. Such a laser would operate in the bad-cavity, superradiant regime where the atomic coherence times are much longer than the cavity decay time [83]. In this regime, atoms form the phase flywheel for the laser and emit collectively into the cavity mode, leading to a superradiant enhancement in the emitted power.

Superradiant lasers were suggested as a powerful type of frequency reference by Meiser et al. in Ref. [108] and a proof of principle Raman laser was first demonstrated in the Thompson lab soon before I arrived as a first year graduate student [23]. We have continued to study the properties and relevant physics behind superradiant lasing over the subsequent years [21, 171, 22], and due to the success of this work, a new Strontium superradiance project has begun, aimed at realizing a narrow optical superradiant laser [122, 120].

In Chapter 3, I will describe an experiment observing the synchronization physics of a superradiant laser by injection locking the laser to an external drive and discussing synchronization behavior of the superradiant ensemble. I derive a phase diagram for the superradiant laser and demonstrate similarities and differences between the superradiant oscillator and standard classical models of synchronization. By studying superradiant synchronization, we develop a framework for understanding the sensitivity of future narrow-linewidth superradiant lasers to external fields.

Additionally, it is common in atomic systems to have multiple possible lasing transitions. By studying the interaction of these different lasing transitions, this work has informed and lead to recent experiments to interfere multiple lasing transitions to observe the fundamental linewidth of the superradiant laser [122]. Lastly, the synchronization threshold is an example of a second order phase transition in an open quantum system, and may be useful in the future for studies of phase transitions in open quantum systems with similarities to recent experiments on the Dicke model [10, 6].

1.4   Format and goals of this thesis

Chapter 2 will be devoted to an overview of various experimental techniques used in this work, and Chapter 3 will discuss experiments related to superradiant synchronization. I will give a basic review of the relevant physics for describing and creating entanglement enhanced, spin squeezed states in Chapter 4, and I will review an experiment to use reversible dephasing to improve coherent rotations of the atomic state in Chapter 5. Then, I will focus on the current largest entanglement enhancement observed in our lab, based on the third generation squeezing experiment in Chapter 6 as well as present a demonstration of squeezing with real-time feedback to create deterministic entangled states. In Chapter 7, I will discuss a recent experiment that used a time averaging scheme to observe a large entanglement enhancement in a homogeneous configuration that would be appropriate for matter wave interferometers.

All of the experiments in this thesis have been (or are in the process of being) published in journal articles. Since much effort was given to clearly describe the experiments in those documents, the bulk of each chapter will rely heavily on these previous writings. Apart from this introduction, I have spent the majority of my original writing focus on experimental details that have not been previously published. These can be found in Chapters 2, 4, and the appendices. I hope that in addition to giving a complete collection of my thesis work and compiling many relevant results, some of these additional details will be useful as a detailed resource for readers wishing to utilize our techniques in the future.

Chapter 2

Experimental System Overview

Many of the experimental details for this work can be found in previous writings [32, 38, 39, 170, 20, 30]. However, I will provide a brief overview of the experimental apparatus here. In addition to the general information in this chapter, additional experimental details that are more relevant or specific to a particular experiment can be found in the chapter describing that experiment. Additional information about homodyne and heterodyne detection as well as the use of feedback loops in our lab can be found in the Appendices.

2.1 Laser cooling and trapping

The first step in the experiment is to laser cool and trap a large ensemble of up to 10^6 ^{87}Rb atoms inside the TEM$_{00}$ mode of an optical cavity. The relevant energy level structure is shown in Figure 2.1. Cooling and trapping is performed in two stages. First the atoms are cooled an trapped in a magneto-optical trap (MOT). Second, the atoms are transferred from the MOT into an optical lattice formed by a resonant cavity TEM$_{00}$ mode and cooled to a final temperature of 10 to 20 μK.

2.1.1 Magneto-optical trap

MOTs are a very robust technology that have become a standard tool in atomic physics [110]. Our MOT is described in detail in refs [20, 30], and relies on 6 laser beams that provide Doppler cooling in every direction as well as repumping from the F=1 ground states where the cooling is not active. A quadrupole magnetic field with gradient of approximately 10 G/cm works in concert
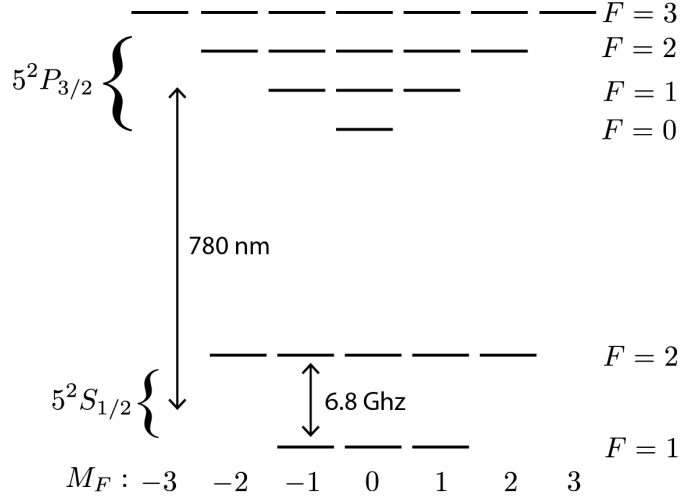
Figure 2.1: Level diagram for the D2 transition in ^{87}Rb. The $F = 1$ and $F = 2$ ground state manifolds are metastable and the excited state lifetime is $\Gamma = 2\pi \times 6.06$ MHz.

with these Doppler cooling beams to form a trapping potential. In our experiment, each MOT laser beam has a characteristic diameter of approximately 1 cm and a power of 10 mW. The MOT beams are red-detuned by around 3 MHz from the $F = 2$ to $F' = 3$ transition with circular polarization. The repumper laser operates on resonance with D2, $F = 1 \rightarrow F' = 2$ transition with a total power of 6 mW. For simplicity, we overlap the MOT and repumper beams before splitting into the 6 orthogonal beams although this is not critical. Atoms in the MOT are cooled near the Doppler temperature, set by the linewidth $\Gamma = 2\pi \times 6.06$ MHz of the optical transition, of $T_{\mathrm{D}} = \hbar\Gamma/(2k_b)$ where k_b is Boltzmann's constant. For Rubidium this is 145 μK.

2.1.2 Vapor pressure

The MOT is loaded directly from a background vapor. The background Rb pressure is observed to be the limiting contribution to the vacuum pressure and is measured using an ion gauge to be approximately 4×10^{-9} Torr. As a useful note, the background vapor pressure can also be approximately measured from the MOT loading time [5], that is of order a second for our system. The vapor pressure is created by heating a Rb ampule to between 50 and 100 degrees C. Recently, we observed that the small aperture in the ampule that allows Rb to escape can get

plugged with an unknown layer, presumed to be rubidium oxide. When this happens, Rb will not be sufficiently released into the main chamber. To avoid this, care should be taken with these objects not to expose the Rb to any air.

2.1.3   Polarization gradient cooling

Sub-doppler cooling occurs very naturally in laser cooling schemes with Rb. In fact, the effect was a mystery for several years leading to a Nobel prize award for the observation and theoretical explanation of sub-Doppler cooling mechanisms [43]. In our experiment, we use the same circular polarized MOT cooling beams to achieve the polarization gradient cooling (PGC). This cooling works best with beams detuned from the optical transition. PGC cooling also requires a zero magnetic field so that Zeeman sublevels are degenerate. This is achieved with bias coils in all three dimensions that can zero the earth's magnetic fields as well as any other biases in the system. In the PGC cooling step, the MOT quadrupole magnetic field is shut off, and atoms are PGC cooled and loaded into the optical trap for around 20 to 50 ms before they have a chance to fall away from the cavity region. After this step, their temperature is measured to be 10 to 20 μK.

2.1.4   Optical lattice and cavity stabilization

The final optical trap of the atoms is created by a cavity standing wave at 823 nm, that we refer to as the optical lattice. This lattice forms an attractive potential for the atoms due to the optical dipole force [110]. The lattice typically has 0.3 W of circulating power and forms a trap with a depth of 115 μK, mode waist of 71 μK and Rayleigh length of 2.05(5) cm. The radial and axial trap frequencies are 1 kHz and 180 kHz respectively. Atoms load the central 1 to 2 mm of the Lattice, and once they are loaded, the ensemble has a rms thermal displacement in the radial direction of approximately 7 μm and a thermal rms displacement in the axial direction of 40 nm at each lattice cite. We load between 10^5 and 10^6 atoms, which means there are 100 to 1000 atoms per site.

Fig. 2.2 shows a simplified experimental diagram of the science cavity frequency stabilization
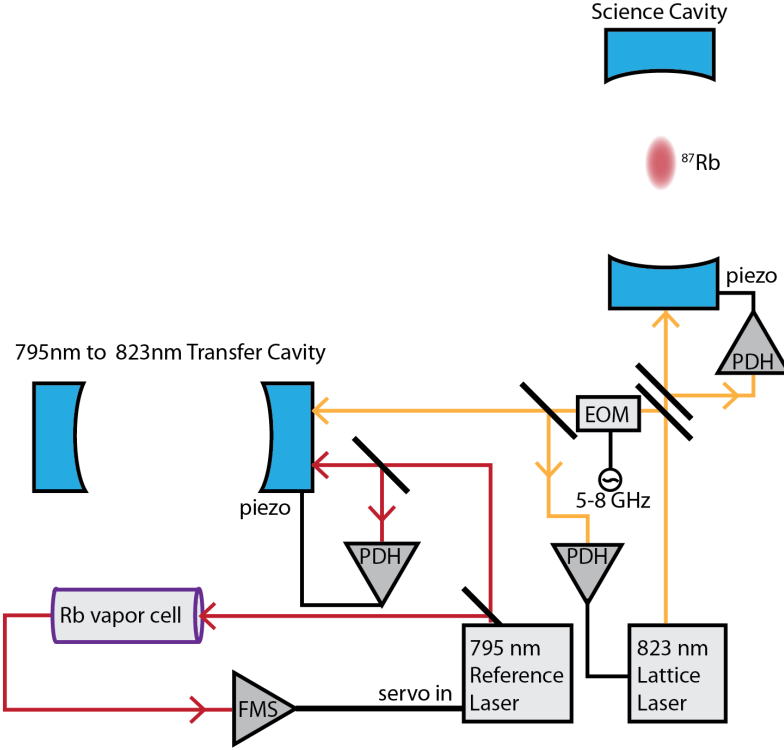
Figure 2.2: Experimental diagram for science cavity frequency stabilization. The main optical cavity is stabilized to an optical lattice using Pound-Drever-Hall (PDH) spectroscopy and feedback to a piezo. A lattice laser sideband created with a tunable EOM is locked to the transfer cavity that bridges the gap between the 795 nm and 823 nm laser frequencies. The transfer cavity is locked using PDH spectroscopy and feedback to a piezo to a 795 nm reference laser. The reference laser is stabilized to an atomic transition in rubidium using FM saturated spectroscopy (FMS).

chain. First a 795 nm reference laser (red) is stabilized to a Rb vapor cell using FM saturated spectroscopy [59] and feedback to the laser's current and piezo. An optical transfer cavity is then stabilized to this laser via the Pound-Drever-Hall (PDH) stabilization method [16, 45] and feedback to a cavity piezo. This cavity serves as an effective "gear" to transfer stabilization to the 823 nm optical lattice. Specifically, phase modulation sidebands are applied to the lattice laser and one of those sidebands is stabilized to the transfer cavity using PDH spectroscopy and feedback. After these three steps, the optical lattice frequency is set. Then, the science cavity is PDH-locked to the lattice laser giving absolute frequency stability to the optical cavity mode. Feedback to the cavity piezos occurs with a bandwidth of approximately 1 kHz limited by resonances in the piezos. As a

note, since the transfer cavity length is not known precisely enough to give an absolute frequency conversion between the 795 nm reference laser and the 823 nm lattice laser, we usually probe the science cavity with a "probe" laser beam with well defined frequency relative to the Rb transition, and then empirically adjust the lattice laser frequency by changing the EOM sideband frequency in Fig. 2.2.

2.2   Vacuum system and optical cavity

The central element to the experiment is the atom cavity system under ultra-high vacuum. A SolidWorks CAD drawing of the cavity is shown below in Fig. 2.3. The cavity was constructed by gluing piezos (Piezomechanik HPCh 150/12-6/2) and mirrors (custom from Advanced Thin Films) to a ZeroDur spacer machined in the JILA machine shop. In order to assemble the system, the mirrors and piezos were first glued together on a clean-room workbench using a Delrin plastic jig that controlled the placement. Meanwhile, an additional "hat" constructed of Macor was used to join the piezos and the cavity spacer, and was secured with additional drops of Torrseal. Vacuum-compatible Kapton-dipped wires were glued to the piezo electrodes with low-outgassing silver epoxy (Epoxy Technology H21D). Additionally, before gluing the mirror-piezo combination to the spacer, the mirror was wrapped with 5 turns of 140 μm diameter Kapton wire purchased from Kurt J. Lesker and secured with thermal epoxy (Epoxy Technology H77), to allow for heating the mirror to expel Rb that can stick to the surface. A plot of the mirror temperature, as measured in vacuum, versus current through the heater wires is shown below in Fig. 2.4.

The measured cavity parameters are shown below in Table 2.1.

One important note is that the cavity linewidth is measured to be 3.15 MHz versus an expected linewidth from construction of approximately 2.8 MHz. During curing, we observed that some epoxy outgassed onto the mirror surface and initially raised the cavity linewidth to approximately 6 MHz. We were able to clean the mirrors and achieve the observed linewidth using the plasma cleaner in the JILA clean room.

The optical cavity is mounted to the vacuum chamber using a vibration isolation mount that

Cavity Parameters (probe $\lambda = 780$ nm)

Single-atom cooperativity $\mathcal{C} = \frac{4g^2}{\kappa\Gamma}$	0.044(6)
Input coupling κ_1	$2\pi \times 2.60(5)$ MHz
Output coupling κ_2	$2\pi \times 0.17(1)$ MHz
Internal losses κ_L	$2\pi \times 0.38(8)$ MHz
Linewidth κ	$2\pi \times 3.15(10)$ MHz
Q.E. due to internal losses κ_1/κ	0.83(3)
Finesse	2532(80)
Free spectral range	8.105(2) GHz
Frequency difference TEM$_{00}$-TEM$_{10}$	2.290(5) GHz
TEM$_{00}$ waist size w_0	70(1) μm
Cavity length	1.849(1) cm
Mirror radius of curvature	4.999(5) cm

Cavity Parameters (lattice $\lambda = 823$ nm)

Input coupling κ_1	$2\pi \times 4.40(10)$ MHz
Output coupling κ_2	$2\pi \times 0.23(1)$ MHz
Linewidth	$2\pi \times 5.8(6)$ MHz
Finesse	1400(150)
Trap depth	115 μK
Power Buildup (P_{circ}/P_{inc})	800(130)
TEM$_{00}$ waist size w_0	71(1) μm

Table 2.1: Relevant cavity parameters at the atomic and cavity probe laser wavelength $\lambda = 780$ nm and at the lattice laser wavelength $\lambda = 823$ nm. The cavity's mirror transmission coefficients, T_1 on the probed end (1) and T_2 on the closed end (2), are expressed in terms of coupling rates $\kappa_{1,2} = T_{1,2} \times$ (free spectral range).
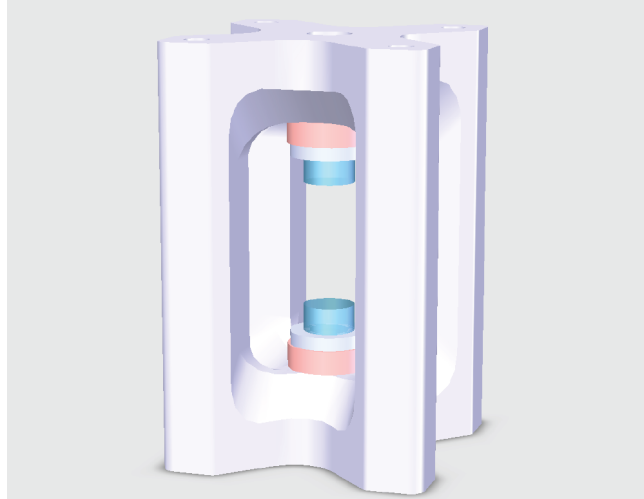
Figure 2.3: Optical cavity CAD diagram. A Macor "hat" (red) is used to join the Zerodur cavity spacer (light purple) and a piezo (white). The piezo and mirror (blue) were glued together beforehand using a plastic (Delrin) alignment jig. Optical cavity parameters are shown in Table 2.1.
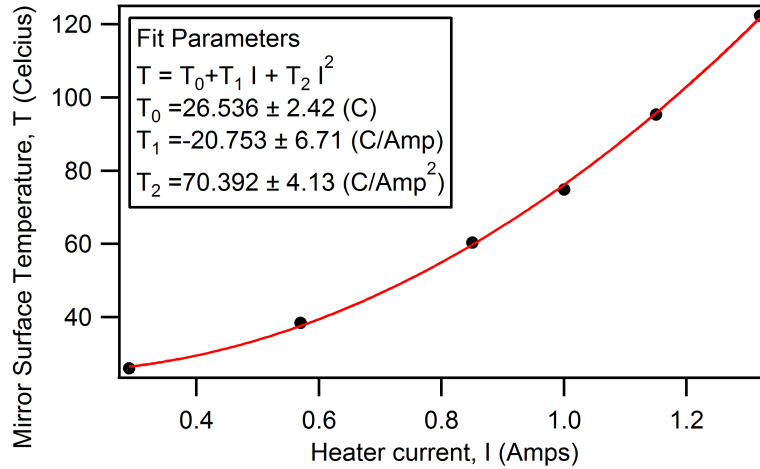
Figure 2.4: Mirror heater calibration. The mirror surface temperature is plotted versus applied current in a vacuum test under the same configuration as the final science cavity.

was adapted from an old version that is described in [30, 20]. However, the previous version was observed to oscillate at 17 Hz leading to oscillations in the transmission power of an optimally aligned, on-resonance laser of up to 20%. In the new version, we simply inserted a clamp to the Viton isolation system to increase the rigidity of the system and rely on the higher quality vibration isolation of the JILA X-wing. Oscillations in the probe laser's coupling to the cavity due

to vibrations have not been observed in the new system.

The cavity system is mounted inside of a large vacuum chamber that extends down through a hole in the optical table. The system is pumped with an ion pump and also has a Titanium-sublimation pump that can be engaged if desired. The system reaches a base pressure of approximately 1×10^{-9} Torr that may be limited epoxy outgassing and the small conductance of the upper part of the vacuum chamber. However, this base pressure should only limit the vacuum lifetime of atoms to nearly a second or greater [5], and has allowed plenty of time to perform current spin squeezing and superradiance experiments.

2.3   State preparation

For most of the experiments described in this thesis we use the qubit states $|\uparrow\rangle = |5^2S_{1/2}, F = 2, M_F = 2\rangle$ and $|\downarrow\rangle = |5^2S_{1/2}, F = 2, M_F = 1\rangle$, the stretched hyperfine ground states. The advantage of these states is that the $|\uparrow\rangle$ state can be probed on an optical cycling transition from $|\uparrow\rangle$ to $|e\rangle = |5^2P_{3/2}, F = 3, M_F = 3\rangle$. In order to prepare the atoms in the $|\downarrow\rangle$ state, we use the optical pumping scheme shown in Fig. 2.5. An $F = 1$ beam is tuned between $F = 1$ and the excited $F' = 0$ state, leaving a dark state in $|\downarrow\rangle$. An $F = 2$ beam is tuned from $F = 2$ to excited $F' = 2$ to clear out all the $F = 2$ levels. The quantization axis is defined by the magnetic field, which is aligned with the cavity axis as shown in Fig. 2.5(a). The polarization is set to a combination of σ_+ and π-polarization along the z-axis. In all, this allows atoms to accumulate in $|\downarrow\rangle$ as shown in Fig. 2.5(b) with approximately 95% of the atoms in the correct state. A small number of atoms in other F=1 sub-states do not significantly affect experiments, but atoms remaining in $|\uparrow\rangle$ can cause serious errors. For this reason, after optical pumping, we often apply a strong final F=2 depumping pulse which ensures that less than 1% of atoms remain in the F=2 manifold. After this step, the various experimental sequences of chapters 3-7 can be performed at will.
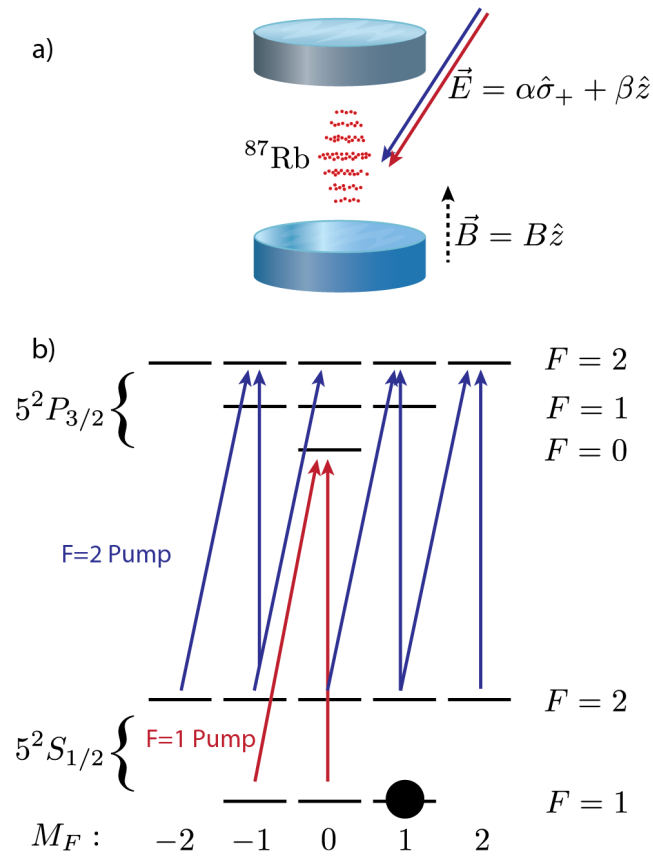
Figure 2.5: Optical pumping scheme to stretched state. a) Two optical pumping beams co-propagate at an angle from the vertical axis with polarization that decomposes into σ_+ and π along the quantization axis set by the magnetic field $\vec{B}$. b) Energy level diagram for optical pumping. Pumping channels are shown by red and blue lines for the F=1 and F=2 pumps respectively. Atoms accumulate in $|\downarrow\rangle = |5^2S_{1/2}, F = 2, M_F = 1\rangle$.

Chapter 3

Superradiant Injection Locking

3.1   Introduction

In a superradiant (or "bad-cavity") laser, the atomic coherence decays much more slowly than the optical cavity field. As such, the atomic coherence primarily stores the laser's phase information and is initially established via spontaneous synchronization of the individual atomic dipoles (as in Fig. 3.1(a)). Unlike in conventional good-cavity lasers, coherence has been shown to persist with less than one, and even zero, intracavity photons [23, 21, 171]. This bad-cavity regime of laser physics has generated recent interest because it offers a promising route for overcoming fundamental thermal mirror noise in order to realize laser linewidths of one milliHertz or less [109].

More broadly, cold atom-cavity systems are extremely well-controlled experiments useful for observing many-body phenomena with the cavity mode providing strong long-range interactions between the atoms. For example, the spontaneous spatial ordering [73, 14, 148, 55] and realization of the Dicke model [11] in cold atom-cavity systems are examples of nonequilibrium phase transitions and provide insights into our fundamental understanding of phase transitions in condensed matter physics [158]. Further, atomic ensembles coupled to many cavity modes may allow the creation of exotic phases of matter with emergent crystallization and frustration [52, 152], and could serve as a model system for associative memories [53]. Superradiant lasers have been identified as an interesting system in which to study the problem of synchronization of quantum oscillators [104, 167].

3.2 Experiment: superradiant injection locking

In this chapter, I will discuss an experiment to study synchronization of a superradiant laser to an externally applied optical field that is injected into the lasing cavity mode (Fig. 3.1(a)). The synchronization is analogous to injection locking in a good-cavity laser, but in this superradiant system phase locking is manifested as collective synchronization of an ensemble of cold atoms to the applied drive. For a weakly injected optical driving field, the system can be approximately mapped to a driven Van der Pol self-oscillator, a canonical system in synchronization physics [125, 124]. We directly observe the two synchronization behaviors predicted for such a system. However, when the applied drive's poer and/or detuning from the self-lasing freqeuency are large, we observe two additional effects which are not explained by either the Van der Pol model or traditional injection locking theory [145]. First, the stimulated emission component at the self-lasing frequency is repulsed from, rather than attracted to, the drive frequency. Second, as the drive strength is increased the stimulated output power at the self-oscillation frequency actually decreases. These two effects arise from the full three-dimensional description of the atomic spin or Bloch vector dynamics, in comparison to a two-dimensional description of a Van der Pol oscillator. The new, third degree of freedom corresponds to the atomic inversion, which is no longer approximately constant at large detunings or drive strengths. In each regime we show good quantitative understanding of our system, providing a solid foundation for future work in fundamental physics using superradiant lasers.

Complex injection locking behaviors beyond the simple Van der Pol description, including instability, chaos, and repulsion, have been theoretically studied and observed in lasers which operate in the crossover regime of laser physics where the cavity decay rate and one or more atomic decay rates are similar [90, 112, 147]. Frequency repulsion is predicted in these lasers from a coupling between the injection locking dynamics and relaxation oscillations [123]. In a distributed feedback (DFB) laser, a one-sided frequency repulsion was seen to arise from tuning of the cavity frequency [99]. In our system, frequency repulsion and three-dimensional dynamics are a direct
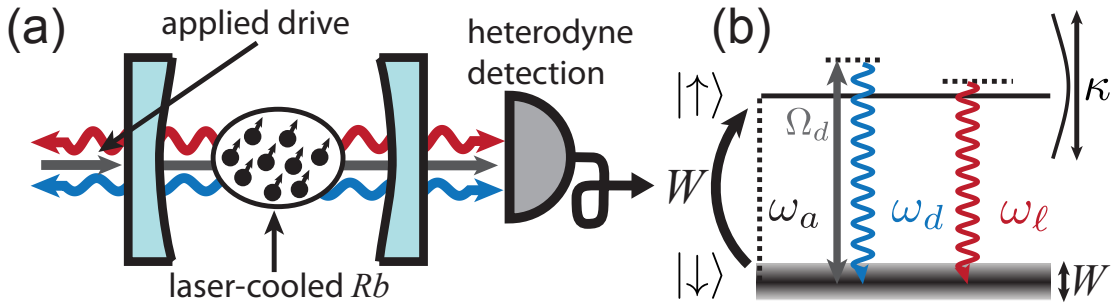
Figure 3.1: Experimental setup and level diagram. (a) Atoms interact with both the externally applied drive (grey) and the intra-cavity field generated by their collective emission (blue and red). The superradiant laser primarily responds at two frequencies, the drive frequency ω_d and a self-lasing frequency ω_ℓ. (b) The characteristic frequencies are displayed in a level diagram, and all lie within one cavity mode of width κ. The Raman laser system is approximated as a 2-level laser incoherently repumped through intermediate optically excited states (not shown) at rate W. W is also the primary source of broadening of the lasing transition (shown as broadening of $|\downarrow\rangle$). In this work, the ratio of atomic and optical linewidths is $W/\kappa \approx 5 \times 10^{-2}$ to $5 \times 10^{-3} \ll 1$, placing the system deep into the bad-cavity or superradiant regime. The state $|\uparrow\rangle$ is a dressed state consisting of a ground hyperfine state of Rb coupled non-resonantly to an optically excited state as described in [23, 18, 171, 21]. The applied drive couples $|\downarrow\rangle$ and $|\uparrow\rangle$ with an on-resonance Rabi frequency Ω_d.

consequence of injection locking deep in the bad-cavity regime, a regime largely inaccessible by previous work [25].

The apparatus for the superradiant laser and principles behind its basic operation have been described in detail in previous work [23, 18, 171, 21]. The atomic gain medium consists of $N \approx 1.1 \times 10^6$ ^{87}Rb atoms cooled to 10 to 20 μK and trapped in a 1D optical lattice inside of an optical cavity with power decay linewidth $\kappa = 2\pi \times 11.8$ MHz. The atoms are tightly confined to $\ll \lambda$ (i.e. the Lamb-Dicke regime) along the cavity axis, but only weakly confined perpendicular to the cavity axis.

A dressing laser is applied transverse to the cavity to induce spontaneous Raman transitions between two hyperfine gound states $|\uparrow\rangle \equiv |5S_{1/2}, F = 2, m_F = 0\rangle$ to $|\downarrow\rangle \equiv |5S_{1/2}, F = 1, m_F = 0\rangle$, with typical single-atom free-space Raman transition rates $\gamma = 2\pi \times 100$ Hz to $2\pi \times 300$ Hz. The cavity frequency ω_c is tuned to be on or near resonance with the spontaneously emitted light's frequency ω_a. The effective two-photon coupling to the cavity is characterized by the rms value of the Jaynes-Cummings coupling constant g_2 [108] and single atom cooperativity parameter $C = \frac{4g_2^2}{\kappa\gamma} = 5 \times 10^{-3}$. The collective (or superradiant) emission rate for a single atom scales as $NC\gamma$.

To maintain population inversion and steady-state emission, additional lasers are applied to incoherently repump atoms through optically excited states from $|\downarrow\rangle$ back to $|\uparrow\rangle$. The characteristic repumping rate from $|\downarrow\rangle$ (including Rayleigh scattering) is $W \approx 2\pi \times 60$ kHz to $2\pi \times 500$ kHz. The repumping process is the primary contribution to the atomic transverse decoherence rate $\gamma_\perp \approx W/2 + \Gamma_D$. We measure a small additional contribution to the transverse broadening Γ_D which is primarily due to doppler broadening of the two-photon transition from $|\uparrow\rangle$ to $|\downarrow\rangle$ resulting from the weak transverse confinement of the atoms.

A conceptually simplified experimental diagram for this work is shown in Fig. 3.1. The key distinct feature in this work is the application of an additional coherent drive to the superradiant laser's cavity mode (Fig. 3.1). The drive couples the upper $|\uparrow\rangle$ and lower $|\downarrow\rangle$ lasing states with a single-atom Rabi frequency Ω_d. The drive frequency ω_d is detuned from the effective atomic

transition frequency ω_a by $\delta_d \equiv \omega_d - \omega_a$ (Fig. 3.1(b)). The behavior of the system depends on the relative magnitudes of drive strength Ω_d, detuning δ_d, and characteristic rates of the superradiant laser: the repumping rate W and characteristic collective emission rate into the cavity $NC\gamma$ given by the collective cooperativity NC and the single-atom decay rate γ from $|\uparrow\rangle$ to $|\downarrow\rangle$.

When no drive is applied the laser emits at frequency ω_{ℓ_0} near, but not necessarily identical to ω_a. When the drive is applied, the lasing frequency ω_ℓ is shifted by the atoms' interaction with the drive by $\delta_\ell \equiv \omega_\ell - \omega_{\ell_0}$. Additionally, the laser can emit at the drive frequency ω_d. We detect the light emitted from the cavity using heterodyne detection. This gives complete information about the emission spectrum and allows us to measure ω_ℓ, ω_d and the phases and amplitudes of the electric fields emitted from the cavity at these frequencies. Other frequency components in the laser emission are expected and observed at sums and differences of ω_ℓ and ω_d. These additional components can become rather large near synchronization (see Ref. [125]).

3.3   Phase diagram

The predicted behavior of the emitted field of the laser is summarized by the theoretical phase diagram in Fig. 3.2. The phase diagram is calculated by numerically integrating optical Bloch equations based on a simplified 2-level model for the superradiant laser (see [22] and Section 3.5). For simplification, the repumping rate W is set to a value that optimizes the output power of the laser $W_{\mathrm{opt}} = \frac{1}{2}NC\gamma$ [109], so that the characteristic rates governing the phase diagram are the two ratios Ω_d/W and δ_d/W.

The primary feature of the phase diagram is the synchronization or non-synchronization of the superradiant emission to the drive. In the unsynchronized phase of region (2), the atomic dipoles are not perfectly synchronized to the drive and the spectrum of light contains two distinct frequency components at the drive frequency ω_d and the self-lasing frequency ω_ℓ. In contrast in region (1), the atomic dipoles become synchronized to the drive and all light emission occurs at ω_d. For the optimum repumping $W = W_{\mathrm{opt}}$ here, the synchronization transition occurs roughly when $\Omega_d = \delta_d$.
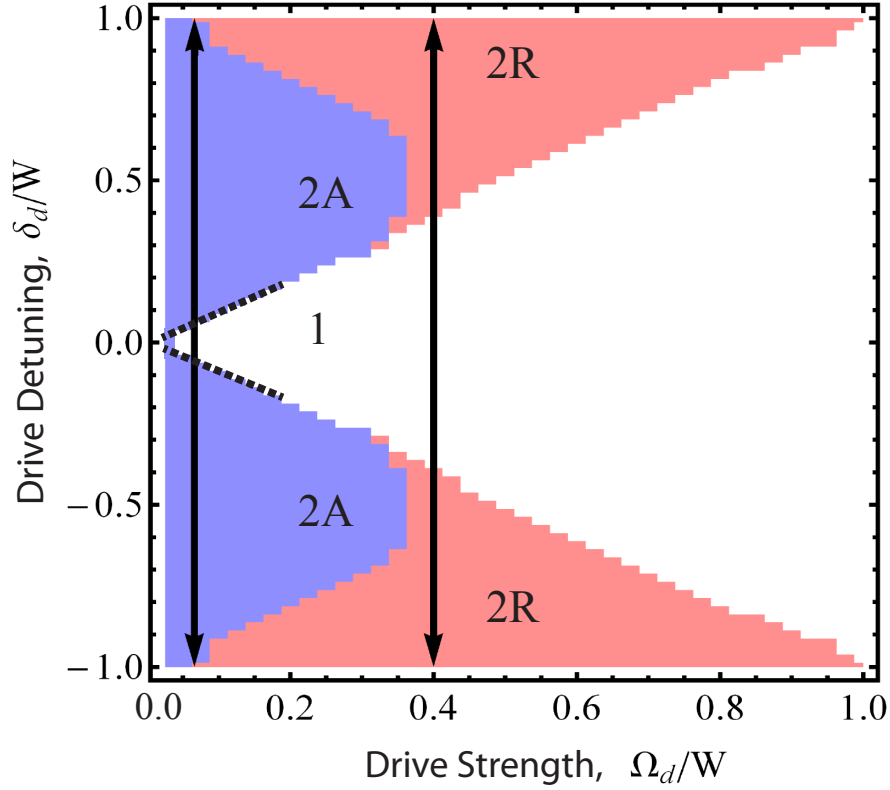
Figure 3.2: The predicted phase diagram for the driven superradiant laser is shown in a plane defined by the applied drive strength Ω_d and the drive detuning δ_d, normalized to the repumping rate W, which is fixed to $NC\gamma/2$ here. The regions are first divided by the number of distinct emission frequencies (1 or 2). Region (2) is further divided by the frequency shift of the self-lasing component at ω_ℓ, which can be attracted (2A) or repelled (2R) from the applied drive frequency ω_d. When $\Omega_d < 0.2 \times W$, the laser synchronizes by smoothly coalescing in frequency with the drive (dashed line). For larger drives, the self-lasing component remains distinct and is quenched. The two trajectories (black arrows) refer to the two parameter trajectories explored by the data in Fig. 3.3.
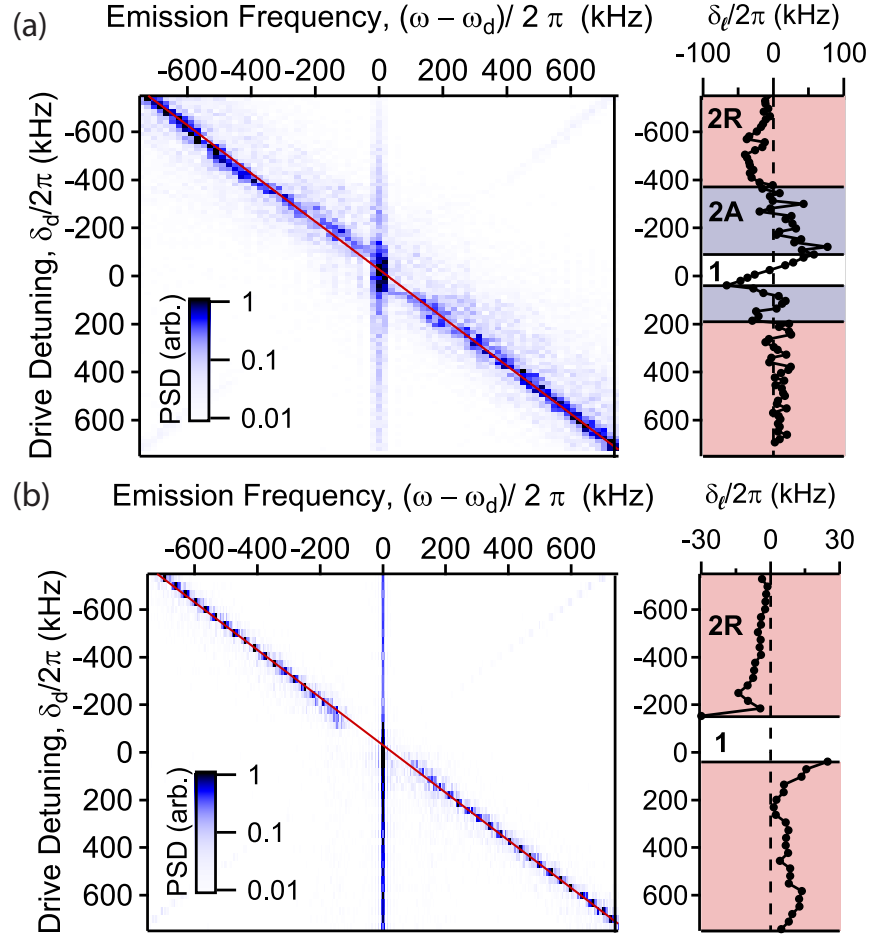
Figure 3.3: Experimental observation of coalescing attractive (a) and repulsive (b) synchronizations. (Left) 2D spectrograms are taken with fixed drive strength Ω_d as the detuning of the drive δ_d is varied along the representative vertical trajectories in Fig. 3.2. Darker colors indicate higher power in a frequency bin (i.e. PSD). The red line indicates the expected self-lasing trajectory in the absence of an applied drive. (Right) Two panels show the frequency shift $\delta_\ell = \omega_\ell - \omega_{\ell_0}$ between the lasing frequency and the lasing frequency when no drive is present. In each region, we qualitatively identify attraction and repulsion by the sign of δ_ℓ and label and color each region similarly to the phase diagram in Fig. 3.2. The behaviors follow the prediction for their respective trajectories across the phase diagram, which are represented by vertical lines in Fig. 3.2.

The unsynchronized region (2) is broken into two subregions, delineated by the self-lasing's attraction toward or repulsion from the drive frequency. The region of attraction ($\frac{\delta_\ell}{\delta_d} > 0$) is labeled (2A) in the phase diagram. The region of repulsion ($\frac{\delta_\ell}{\delta_d} < 0$) is labeled (2R). As δ_d or Ω_d are tuned, the behavior of the approach to synchronization depends on whether one enters region (1) from region (2A) or (2R). For attractive synchronization (from (2A) to (1)), as the $\Omega_d = \delta_d$ boundary

is crossed, ω_ℓ is pulled toward the drive. For drive strengths $\Omega_d < 0.2 \times W$ (dashed line in Fig 3.2), the self-lasing component synchronizes by smoothly coalescing with the drive at ω_d. When $\Omega_d > 0.2 \times W$, the self-lasing is driven to zero before coalescence can occur. In the repulsive synchronization (from (2R) to (1) in the phase diagram), as one approaches synchronization ω_ℓ is repelled in frequency from ω_d and the self-lasing component is driven to zero so that the superradiant ensemble is emitting power only at the drive frequency ω_d.

In the limit $\Omega_d, |\delta_d| \ll W$, the laser inversion J_z is approximately fixed, and the three-dimensional Bloch vector (J_x, J_y, J_z) describing the atomic ensemble can be reduced to an effective two dimensional object described by the transverse coherence $J_- = J_x - iJ_y$. In this case, the equation describing the time evolution of J_- is closely equivalent to that of a driven Van der Pol oscillator, for which attractive synchronization ((2A) to (1)) with and without coalescence (characterized by saddle-node and Hopf bifurcations respectively) have been well studied [125, 124]. We outline this mapping explicitly in Section 3.7.

However, when either Ω_d or $|\delta_d| \gtrsim W$, the inversion J_z can no longer be approximated as fixed and the dynamic response of the full three-dimensional Bloch vector must be considered. The response of the extra degree of freedom J_z leads to the repulsive behavior in region (2R) which can be interpreted as an AC Stark shift (Section 3.7).

Experimental examples of the two synchronization transitions are shown in Fig. 3.3, with approximate trajectories in the phase diagram represented by black arrows in Fig. 3.2. Fig. 3.3(a) demonstrates attractive, coalescing synchronization and Fig. 3.3(b) represents repulsive synchronization. The left plots are two-dimensional power spectra of the laser emission. Each horizontal slice corresponds to a single power spectrum of laser emission where color represents the optical power in each frequency bin. The nominal detuning δ_d is changed between experimental trials and plotted on the left axis. On the horizontal axis, the drive freqency ω_d is set to zero so that in the absence of an applied drive ($\Omega_d = 0$), the emission frequency ω_ℓ would follow the diagonal red line. At sufficiently small detunings synchronization occurs and only power at ω_d is observed. A faint spectral component in Fig. 3.3 appears on the opposite side of zero from the self-lasing component.

We believe this small feature is an artifact of nonlinearities in the detection system.

The spectrograms illustrate the qualitative differences between the two types of synchronization. In Fig. 3.3(a), the self-lasing frequency ω_ℓ is attracted toward and joins ω_d as $|\delta_d|$ becomes small. In Fig. 3.3(b), the two emission components remain distinct until the ω_ℓ component is extinguished. To more clearly illustrate the attraction and repulsion, the measured quantity $\delta_\ell = \omega_\ell - \omega_{\ell_0}$ is plotted on the right. The plots are overlaid with color and labeled to help identify the repulsion (red) and attraction regions (blue) matching the phase diagram of Fig. 3.2. For the trajectory at small Ω_d the laser goes from synchronized (1), to attraction (2A), to repulsion (2R) as predicted. For the trajectory at larger ω_d there is a single transition from (1)- to (2R)-like responses. Both behaviors qualitatively agree with the prediction from the phase diagram for a 2-level laser, shown by the trajectories in Fig. 3.2.

The qualitative behavior of the data exhibits asymmetry with respect to $\delta_d = 0$, whereas the theoretical phase diagram of Fig. 3.2 is symmetric. This is because the data did not strictly follow the vertical trajectories shown in Fig. 3.2. As the detuning δ_d was changed, the fractional amount of the fixed incident drive power coupled into the cavity changed, following the Lorentzian cavity resonance profile. The symmetry of this effect about $\delta_d = 0$ is broken by the fact that $\delta_c \equiv \omega_c - \omega_a \neq 0$ (where ω_c is the cavity resonance frequency), leading to the observed asymmetry in the data of Fig. 3.3.

3.4   Van Der Pol description

We now turn to the development of a perturbative description of the system far from synchronization and the break down of this description as the system approaches and ultimately crosses the synchronization threshold.

Deep into region (2) of the phase diagram, the superradiant laser's response to the drive is small and can be understood as a small modulation of the initially undriven Bloch vector describing the atomic coherence. The modulated Bloch vector then radiates an additional field into the cavity at the drive frequency ω_d, producing gain. In Fig. 3.4(a) we measure this power gain G and phase
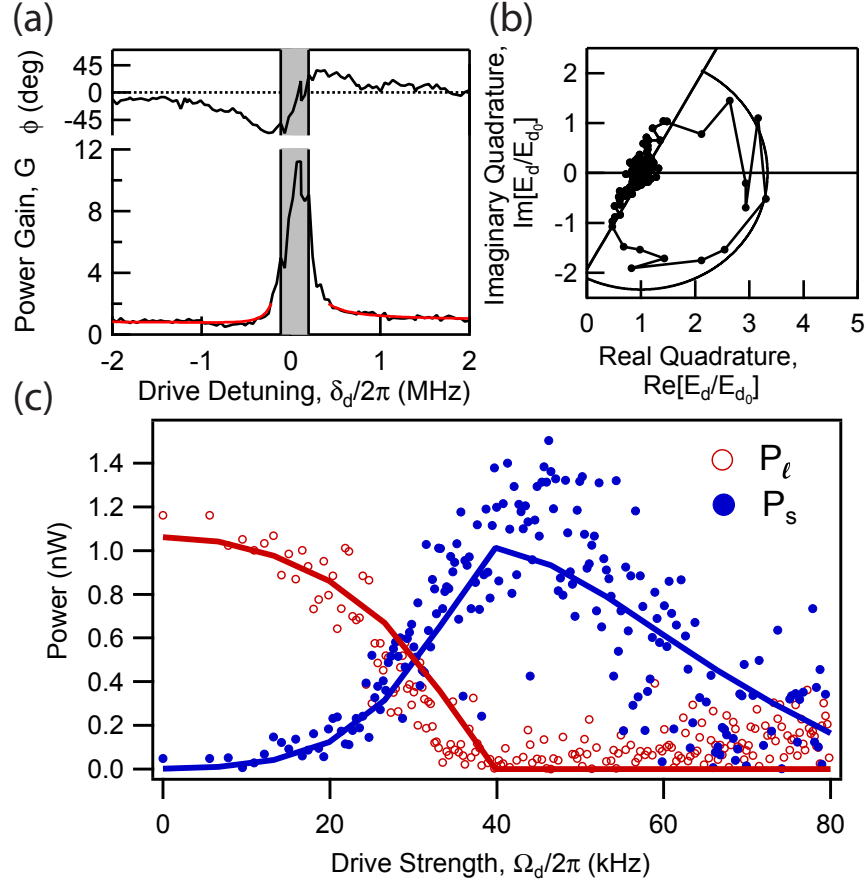
Figure 3.4: Synchronization and gain saturation. (a) Measured gain and phase response of the superradiant laser at the drive frequency ω_d. At large drive detunings, the response displays linear small-signal gain (red fit to perturbative model overlayed). The gain saturates (grey shaded region) at small detunings as the laser approaches the synchronization transition. (b) The same gain and phase response are represented in a phasor picture. Points of small signal gain lie along the straight line, and the region of saturation is approximately described by a curve of maximum stimulated electric field (inner curve). (c) The stimulated output powers P_s and P_ℓ, at the self-lasing frequency ω_ℓ (red) and at the drive frequency ω_d (blue) respectively, are displayed as the laser is driven across a repulsive synchronization transition at approximately $\Omega_d/2\pi \approx 40$ kHz. Theoretical predictions (solid lines) show good agreement with the data.

response ϕ of the laser at the drive frequency ω_d versus the drive detuning δ_d. This corresponds to a vertical trajectory on the phase diagram where, in this dataset, $\frac{\Omega_d}{W} \approx 0.04$. A fit to a perturbative model based on the optical Bloch equations in Section 3.6 is shown in red.

At small detunings (grey region), the gain and phase response begin to saturate, and deviate from the predicted small-signal values. This is roughly the point when the laser begins to synchro-

nize to the drive and the emission at frequencies other than ω_d begin to disappear. In Fig. 3.4(a) we have chosen a specific drive strength ($\frac{\Omega_d}{W} \approx 0.04$) to illustrate the transition from linear gain to saturation. If a smaller(larger) drive strength is chosen, we observe that, as expected, saturation occurs at a smaller(larger) detuning.

In Fig. 3.4(b), the equivalent complex electric field response E_d at the drive frequency is shown in a phasor diagram with each point corresponding to the measured field at a given detuning in Fig. 3.4(a). The drive response when no atoms are present E_{d_0} is normalized to be real and of length 1. In the perturbative limit, the additional stimulated field follows a straight line. The line of small-signal gain is tilted due to an additional phase shift of the stimulated field arising from nonzero detuning of the drive from the optical cavity $\omega_d - \omega_c \neq 0$. At saturation, the stimulated field deviates from the straight line and qualitatively follows a contour of constant stimulated electric field (solid semi-circle).

In Fig. 3.4(c) we show an example of how optical power is "stolen" from the self-lasing frequency ω_ℓ and transferred to the drive frequency. Here the drive strength Ω_d is increased at a fixed detuning $\delta_d/W = 2.2$, and the vertical axis shows the self-lasing power P_ℓ and the stimulated drive power $P_s \equiv P_d - P_{d_0}$. P_{d_0} is the detected power at the drive frequency in the absence of any atomic response, scaling as $P_{d_0} \propto \Omega_d^2$, such that P_s represents the extra stimulated power at ω_d. This dataset corresponds to tuning the system along a horizontal line in Fig. 3.2 that lies outside the plotted range and such that the system crosses from the repulsive region (2R) to the synchronized region (1).

Numerical solutions (solid lines in Figure 3.4(c)) of the optical Bloch equations (Section 3.5l) give reasonable agreement with the data. The theoretical model includes approximate corrections for an additional cavity tuning effect [21], and the absolute vertical scale of the theory has been scaled so that the P_ℓ agrees with the data at $\Omega_d = 0$.

The synchronization point in this data is represented by the sharp point when P_ℓ hits zero, with a discontinuous first derivative in P_ℓ and P_s. At the synchronization point, P_s is approximately the original output power of the laser when Ω_d is zero. At large drive strengths in Fig. 3.4(c), Ω_d

becomes much larger than W and the total output power of the laser decreases due to repumping-induced dephasing of the rapid Rabi oscillations caused by the drive. This reduction in stimulated output power is another unique aspect to injection locking in the bad-cavity laser.

3.5   Optical Bloch equations

The average behavior of the superradiant laser with an applied drive can be understood with slight modifications to the optical Bloch equations presented in [22]. The optical Bloch equations describe the time evolution of expectation values of the cavity annihilation operator $\hat{a}$ and the collective atomic operators, $\hat{J}_z$ and $\hat{J}_-$, defined as,

$$\hat{J}_z = \sum_{i=1}^{N} \frac{|\uparrow_i\rangle \langle\uparrow_i| - |\downarrow_i\rangle \langle\downarrow_i|}{2} \tag{3.1}$$

$$\hat{J}_- = \sum_{i=1}^{N} |\downarrow_i\rangle \langle\uparrow_i|. \tag{3.2}$$

$\hat{J}_z$ and $\hat{J}_-$ represent the atomic inversion and transverse coherence respectively. The optical Bloch equations govern the time evolution of the expectation values of these operators, $J_z = \langle\hat{J}_z\rangle$, $J_- = \langle\hat{J}_-\rangle$, and $E = \langle\hat{a}\rangle$. The atomic response can be visualized as a three-dimensional Bloch vector with x and y projections of the vector given by $J_- = (J_x - iJ_y)/2$. E is a complex representation of the optical cavity electric field such that $|E|^2$ is the average number of photons inside the cavity. The nonlinear equations are closed by approximating that the expectation values of products of operators can be factorized into products of expectation values. Assuming uniform coupling to the cavity mode, the coupled equations for a 2-level system with an applied drive can be written as

$$\dot{E} = -\left(\frac{\kappa}{2} + i\delta_c\right) E - ig_2 J_- + \frac{\kappa}{2} E_{d_i}\, e^{i\delta_d t} \tag{3.3}$$

$$\dot{J}_- = -\gamma_\perp J_- + i2g_2 J_z E \tag{3.4}$$

$$\dot{J}_z = -W J_z + \frac{N}{2} W + ig_2(J_- E^* - J_-^* E). \tag{3.5}$$

The equations are written in a frame rotating at the atom's natural transition frequency ω_a. E_{d_i} is proportional to the amplitude of the electric field of the applied drive incident on the optical

cavity. $\delta_c = \omega_c - \omega_a$ is the detuning of the cavity from the natural atomic transition frequency ω_a. The rest of the equation parameters are defined in previous text. The Rabi frequency of the drive is related to these parameters by $\Omega_d = \frac{2g_2 E_{d_i}}{1+\tilde{\delta}_c^2}$, where quantities $\tilde{A} \equiv \frac{A}{\kappa/2}$. The measured intracavity field when no atoms are present is $E_{d_0} = \frac{E_{d_i}}{1+i\tilde{\delta}_{d,c}}$, where $\delta_{d,c}$ is the detuning of the driving electric field from the cavity resonance, $\delta_{d,c} = \omega_d - \omega_c$.

We have numerically solved these equations to derive the phase diagram of Fig. 2 and to create theoretical curves for Fig. 4. The two-level model does a reasonable job of predicting the behavior of synchronization versus Ω_d and δ_d. However, due to the true multi-level structure of the atom, these equations cannot be used to predict the total output power of the system. When these equations are not adequate, multi-level optical Bloch equations from Ref. [22] can be used. Additionally, to approximately account for dispersive shifts of the optical cavity in our Raman laser, the cavity detuning δ_c is made a function of J_z to generate the theory for Fig. 4(c). Details can be found in Ref. [22].

3.6 Derivation of small-signal gain

The small-signal regions of gain and phase response, as described in the main text, follow a simple form that can be derived from the optical Bloch equations. We first assume κ is larger than all other characteristic frequencies in the system so that E adiabatically follows J_-. We then assume that J_- primarily responds at two frequencies, ω_a and ω_d, and make the ansatz $J_- = J_{-a} + J_{-d}\, e^{i\delta_d t}$. Lastly, we assume that in this perturbative limit J_z is unaffected by the weak drive, and retains its steady state value with no drive, $J_{z_{ss}} = \frac{W(1+\tilde{\delta}_c^2)}{2C\gamma}$. With these approximations, we find the small-signal complex field response at the drive frequency. The total detected field at the drive frequency, $E_d = E_{d_0} + E_s$, has two contributions. One contribution (E_{d_0}) comes from the drive alone, and the other (E_s) from atomic stimulation. The small-signal form of E_s is given by

$$E_s = \frac{-iE_{d_0}\gamma_\perp(1+\tilde{\delta}_c^2)}{\delta_d(1+i\tilde{\delta}_c)}. \tag{3.6}$$

In the limit $\tilde{\delta}_c = 0$, E_s can be written in the form $E_s = \frac{-i\sqrt{\alpha}E_{d_0}}{\delta_d}$, where $\sqrt{\alpha}$ characterizes the stimulated field gain. From Eq. 3.6 one expects $\alpha = \gamma_\perp^2$.

Eq. 3.6 explains several features of the measured small-signal gain shown in Fig. 4 of the main text. For $\delta_c = 0$, the stimulated field is in the orthogonal quadrature to the driving field. However, when $\delta_c \neq 0$ as is the case in the data of Fig. 4(b), the response of the cavity to the driving atomic dipole causes the stimulated field to be partially rotated into the same quadrature as the driving field. This rotation breaks the symmetry about $\delta_d = 0$ for both the measured phase and power gain shown in Fig. 4(a).
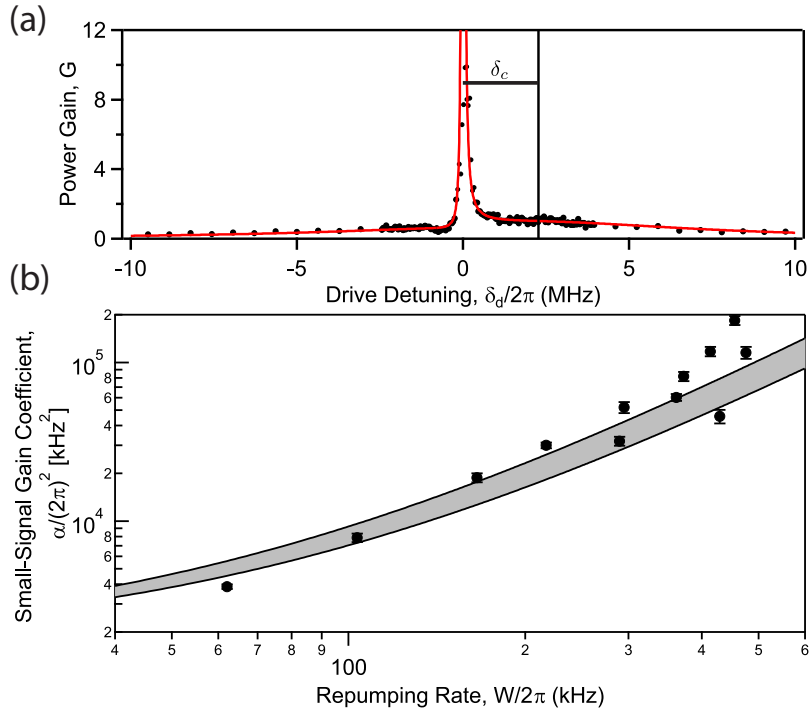
Figure 3.5: Quantitative small-signal gain measurements. (a) We measure the total transmitted power at the drive frequency ω_d and define power gain G as the measured transmitted power normalized to the drive power transmitted through the cavity on resonance with no atoms present. For these measurements δ_d is scanned over a frequency range greater than the cavity linewidth κ. The data is fit to the model in Eq. 3.7 (red line). Note that here, the cavity resonance marked by the vertical solid line is a few MHz higher than the atomic resonance. (b) From fits to data such as (a), we plot the variation of the fitted gain coefficient α (see text) versus W. The prediction $\alpha = \gamma_\perp^2$ is shown in grey. The width of the grey band corresponds to the uncertainty in an independant calibration of the repumping rate W.

To quantify the small-signal gain experimentally, we measure the total output power of the

laser at the drive frequency for a large range of drive detunings δ_d. We fit the total output power to the gain model shown in Eq. 3.7. Equation 3.7 is the magnitude squared of Eq. 3.6 with the E_{d_0} dependence on $\tilde{\delta}_{d,c}$ written explicitly.

$$G(\delta_d, \tilde{\delta}_{d,c}) = \frac{G_0}{1 + \tilde{\delta}_{d,c}^2} \left\{ 1 - 2\frac{\sqrt{\alpha}(\tilde{\delta}_c - \tilde{\delta}_0)}{(\delta_d - \delta_0)} + \frac{\alpha[1 + (\tilde{\delta}_c - \tilde{\delta}_0)^2]}{(\delta_d - \delta_0)^2} \right\} \tag{3.7}$$

For a single scan of δ_d, we allow fitting of the parameters G_0, α, δ_c, κ, and δ_0. The fit model constrains the transmitted power to be G_0 when the drive is on resonance with the cavity in the absence of an atomic response. The δ_0 coefficient allows for an arbitrary offset of the atomic transition frequency ω_a from zero. Figure 3.1(a) displays an example of this measured total output power as a function of δ_d with the fit overlaid in red. In Fig. 3.1(a), the data has been rescaled such that the fitted coefficient $G_0 = 1$. After this rescaling, the data represents the total power emitted at the drive frequency, normalized to the power transmitted through the cavity when the drive is on resonance with the cavity and no atoms are present. Also, the frequency axis of the data has been adjusted such that $\delta_0 = 0$.

We follow this procedure, measuring the output power and fitting to Eq. 3.7, for many repumping rates W. We plot the fitted gain coefficients α versus W in Fig. 3.1(b). The prediction that $\alpha = \gamma_\perp^2 = (W/2 + \Gamma_D)^2$ is overlaid in grey. Uncertainty in the prediction (width of the grey band) is due to uncertainty in the experimental calibration of W. The prediction shows reasonable agreement with the theory over a significant range of W.

3.7 Bloch vector interpretation of phase diagram

The predicted phase diagram is shown in Fig. S2. The behavior in each of the 3 regions can be visualized by the behavior of the Bloch vector in each regime. In a frame rotating at the atom's natural transition frequency ω_a, the applied drive can be represented by a rotation of the Bloch vector, $\vec{\Omega}_d = \Omega_d \left(\hat{\mathbf{x}} \cos(\delta_d t) + \hat{\mathbf{y}} \sin(\delta_d t) \right)$. $|\Omega_d|$ is the angular frequency of the rotation, and $\hat{\Omega}_d$ is the axis about which the Bloch vector rotates. The azimuthal phase of the applied rotation axis precesses at frequency δ_d. When $\Omega_d \ll |\delta_d|$, the drive primarily acts to slightly modulate the
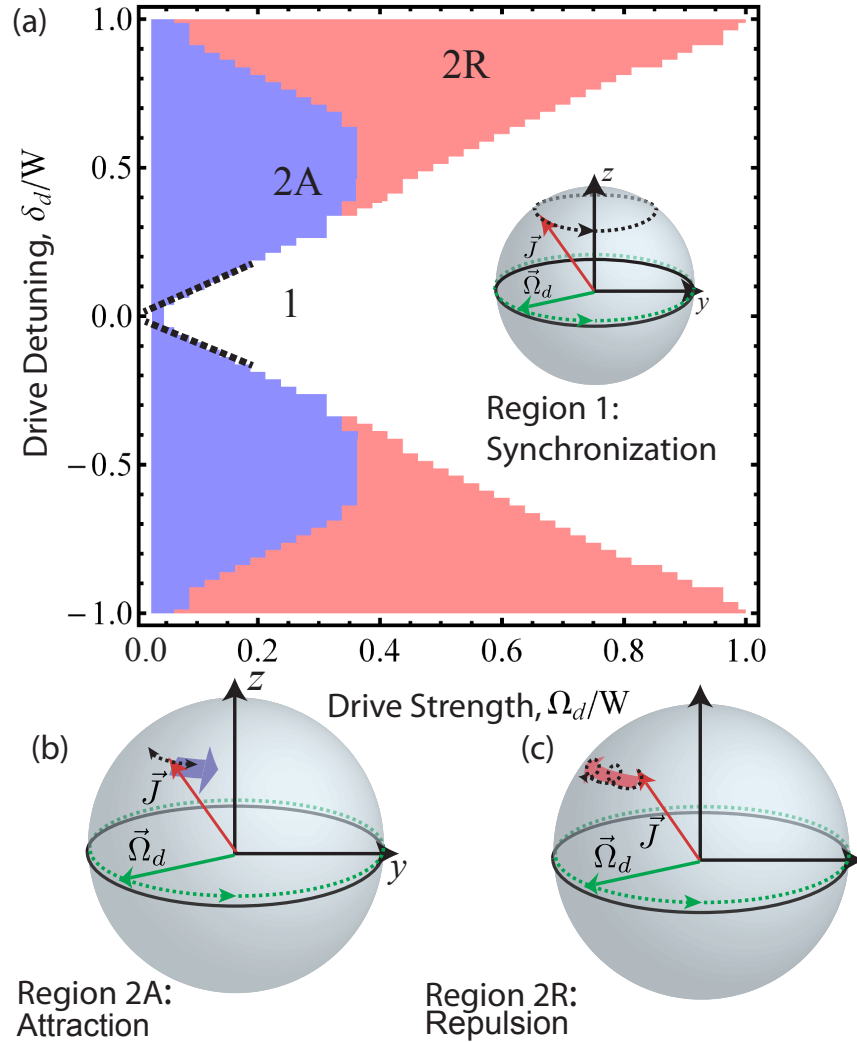
Figure 3.6: Bloch vector interpretation of phase diagram. (a) The types of behavior for the driven superradiant laser can be characterized by a phase diagram. The characteristic rates that determine the lasing behavior are drive Rabi frequency Ω_d, detuning δ_d, and repumping rate W. The regions correspond to the number of distinct emission frequencies (1 or 2) and the frequency shift (attraction or repulsion) of the carrier (A and R respectively). The behavior of the synchronization (a), attraction (b), and repulsion (c) configurations are shown in a Bloch sphere picture. In the frame of the atomic transition frequency ω_a, the drive is represented by a rotation $\vec{\Omega}_d$, with an orientation which rotates along the dashed green trajectory at frequency δ_d. In the unsynchronized case this modulates the Bloch vector (red vector), causing drift toward or away from the drive, with the average precession of the Bloch vector indicated in each case via the large blue and red arrows. In the synchronized case, the Bloch vector follows the drive all the way around the sphere.

orientation of the Bloch vector (both Fig. 3.6(b) and (c)). However, when $\Omega_d > |\delta_d|$, the applied modulation is so large that the Bloch vector can actually follow the drive all the way around the sphere. This is the synchronized region (1) in Fig. 3.6(a). Near the synchronization transition, the repulsive (2R) versus attractive (2A) behavior is determined by the size of the repumping rate W compared to δ_d and Ω_d.

3.7.1   Attractive regime: mapping to 2D Van der Pol oscillator

In the case $|\delta_d|, \Omega_d \lesssim W$ (i.e. 2A) the drive does not significantly perturb the laser from its steady-state inversion because any change in J_z caused by the applied field is quicky healed by the repumping process [18]. When J_z is not modified, the azimuthal phase ϕ is partially or fully dragged in the same direction as the rotating axis $\hat{\Omega}_d$ (Fig. 3.6(a)). The lasing can be viewed as being captured by the applied drive.

Furthermore, in this regime of weak drive, $|\delta_d|, \Omega_d \lesssim W$, the system can be mapped onto a Van der Pol self-oscillator model with a nonlinear driving term,

$$\jmath_- = -i\delta\jmath_- + \lambda\jmath_-(1 - |\jmath_-|^2) + \Omega(1 - \beta|\jmath_-|^2) \tag{3.8}$$

with complex amplitude $\jmath$ and characteristic rates λ, δ, Ω, and β. Equation 3.8 has an equilibrium amplitude $|\jmath_-|^2 = 1$. The nonlinearity of the applied drive is governed by the parameter β. For $\beta = 0$ this model has been well studied [125, 124].

To explicitly show the mapping of the optical Bloch equations (Eq. 3.3) onto this form, we first eliminate the cavity field E by assuming operation in the deep bad-cavity limit, and assume that J_z is not perturbed by the drive. Setting $\dot{J}_z$ equal to zero gives the nominal steady state value,

$$J_{z_{ss}} = \frac{N}{2} - \frac{C\gamma}{W}|J_-|^2. \tag{3.9}$$

One can then insert $J_{z_{ss}}$ into the J_- equation in Eq. 3.3, which leads to

$$\dot{J}_- = -i\delta_d J_- + J_- \left[\left(\frac{NC\gamma}{2} - \frac{W}{2} \right) - \frac{(C\gamma)^2}{W}|J_-|^2 \right] \tag{3.10}$$
$$+ \frac{\Omega_d}{2} \left(\frac{N}{2} - \frac{C\gamma}{W}|J_-|^2 \right).$$

Eq. 10 is identical in form to Eq. 3.8. For the case of optimal repumping, we set $W = W_{\text{opt}} = \frac{NC\gamma}{2}$, and normalize J_- to its steady state value defining $\jmath_- = J_-/J_{-ss}$, where $J_{-ss} = \frac{N}{\sqrt{8}}$, giving

$$\dot{\jmath}_- = -i\delta_d\jmath_- + \frac{NC\gamma}{4}(1 - |\jmath_-|^2) + \frac{\Omega_d}{\sqrt{2}}\left(1 - \frac{|\jmath_-|^2}{2}\right). \tag{3.11}$$

This equation is of the same form as Eq. 3.8 with $\delta = \delta_d$, $\Omega = \frac{\Omega_d}{\sqrt{2}}$, $\beta = \frac{1}{2}$, and $\lambda = \frac{NC\gamma}{4}$. We can define an effective drive strength $\Omega_d' = \frac{\Omega_d}{\sqrt{2}}\left(1 - \frac{|\jmath_-|^2}{2}\right)$. For a weak drive, the laser remains close to its steady state. One finds $\Omega_d' = \frac{1}{\sqrt{8}}\Omega_d$, and the system can be thought of as behaving similarly to the standard driven Van der Pol oscillator of Ref. [125, 124] with a constant driving term.

3.7.2 Repulsive regime: 3D dynamics

When the drive is applied with a large detuning $|\delta_d| \gtrsim W$ (i.e. (2R)), the repumping at rate W cannot heal the changes in the inversion J_z caused by the applied drive [18]. J_z can no longer be considered static and thus introduces a third degree of freedom (in addition to J_x and J_y) in the system. In this regime, the Van der Pol model breaks down, and small oscillations in J_z must be taken into account. The unhealed modulations of J_z at frequency δ_d coherently interact with the applied rotation due to the drive to cause the Bloch vector to on average aquire a small precession in the opposite sense to the precession of the drive rotation axis $\hat{\Omega}_d$ (shown in Fig. 3.6(c)). The precession rate is second order in Ω_d and can be identified as an AC Stark shift that leads to the observed frequency repulsion in region (2R). To emphasize, this shift does not appear in region (2A) because there the repumping process acts to smooth out the modulations in J_z that are essential for creating the AC Stark shift.

The AC Stark shift can be derived to leading order by perturbatively allowing for small oscillations in J_z. In this way we can mathematically show the additional repulsive behavior not evident in the 2-dimensional model of Eq. 3.8. The optical Bloch equation for J_z allowing for modulation, and written in the frame of the drive frequency ω_d is,

$$\dot{J}_z = -WJ_z + \frac{N}{2}W - C\gamma|J_-|^2 - \Omega_d\text{Re}(J_-) \tag{3.12}$$

We treat this equation perturbatively by assuming that J_- primarily oscillates at the self-lasing frequency. From this we can derive a leading order repulsion term giving a new self-lasing frequency,

$$\delta' = \delta_d + \frac{\Omega_d^2 \delta_d}{2(\delta_d^2 + W^2)},\tag{3.13}$$

which arises from oscillations in J_z coupling into an average frequency repulsion of the Bloch vector. This repulsive physics is not present in the driven Van der Pol oscillator and arises from the Bloch vector occupying a higher, 3-dimensional parameter space.

3.8   Outlook

We have observed for the first time two different types of synchronization transitions of a superradiant laser to an external drive, one attractive and one repulsive in nature. The synchronization transition is analogous to a ferromagnet in the presence of an applied magnetic field, the drive breaking a continuous symmetry of the laser with respect to phase [44]. However, the laser steady state is far from thermodynamic equilibrium, making our well-controlled cold atom-cavity system an interesting avenue for continued study of nonequilibrium phase transitions with modern approaches [158].

It is often useful to apply an external drive to a superradiant laser. Such drives have been used, for instance, to probe the frequency of the optical cavity in Raman-laser systems such as ours (as was done in ref. [18]) or perhaps in future narrow linewidth superradiant lasers to reduce errors, inaccuracies, and technical noise due to cavity frequency pulling. This work establishes understanding for how such a technical probe will affect the system. Furthermore, the phase response within the saturation region of Fig. 3.4(a) could be used as an error signal for a form of active spectroscopy of the gain medium, in some sense, the inverse approach to that of Ref. [106], although the fundamental signal-to-noise of such an approach is an open question.

In the future, this work will guide the interpretation of other proposed experiments in cold atom-cavity systems. For instance, multiple superradiant sub-ensembles each with an independent

transition frequency ω_a can be engineered to interact with each other through one or multiple cavity modes [52, 152, 53, 178, 104, 167]. Furthermore, while injection locking is well-described by a mean field description, and therefore can be considered classical behavior, recent theoretical works propose systems of multiple superradiant ensembles where quantum noise becomes observably large and may serve to drive the phase transitions and affect the average behavior [178, 167, 104].

Chapter 4

Review: Spin Squeezing and Joint Measurements with Atoms in Cavities

4.1   Quantum sensors and the Bloch sphere

Many quantum sensors use 2-level atoms or qubits as the sensing device. Such sensors are used for state-of-the-art measurements of time and frequency [115, 66], electric and magnetic fields [85, 2], fundamental constants [135, 175, 36], tests for new physics [61, 7], biological systems [81], and more. An arbitrary quantum state of a 2-level atom used for these sensors can be written as,

$$|\psi\rangle = \cos\left(\frac{\theta}{2}\right)|\uparrow\rangle + e^{i\phi}\sin\left(\frac{\theta}{2}\right)|\downarrow\rangle, \tag{4.1}$$

where $|\uparrow\rangle \equiv |e\rangle$ is the excited state and $|\downarrow\rangle \equiv |g\rangle$ is the ground state. The superposition is parametrized by the two angles θ and ϕ which tell the population and phase of the superposition respectively. The 2-level system is equivalent to a quantum spin-1/2 particle that, when measured, must collapse into either spin "up" or spin "down". It is convenient to visualize the 2-level system's quantum state as a pseudo-spin vector, or Bloch vector [48], labeled $\vec{j}$ that lives on the surface of a Bloch sphere. The Bloch vector is defined as $\vec{j} = j_x\hat{x} + j_y\hat{y} + j_z\hat{z}$ with the $\alpha \in \{x, y, z\}$ component equal to a first order expectation value $j_\alpha \equiv \langle\hat{j}_\alpha\rangle$ of the spin operator $\hat{j}_\alpha$, that are simply proportional to the Pauli spin operators, $\hat{j}_\alpha = \hat{\sigma}_\alpha/2$. By these definitions, the Bloch sphere is normalized so that the z projection of the Bloch vector, $j_z = (P_\uparrow - P_\downarrow)/2$, is equal to the difference in probabilities of the atom existing in the two states $|\uparrow\rangle$ and $|\downarrow\rangle$. Similarly, the transverse components of the Bloch vector give the magnitude and phase of the coherence between the two states. An example Bloch vector is plotted below in Fig. 4.1.
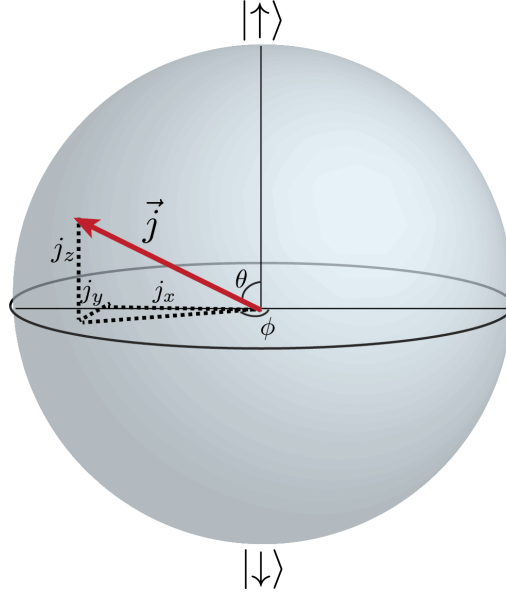
Figure 4.1: A 2-level atom's quantum state is represented by a Bloch vector $\vec{j}$ that lives on the surface of a Bloch sphere. The state can be parameterized by vector components j_x, j_y, and j_z or angles θ and ϕ.

In all of our experiments, we deal with a large ensemble of 10^4 to 10^6 atoms. So we most commonly think in terms of a collective Bloch vector composed of many individual Bloch vectors arranged tip to tail. Going forward, unless otherwise states, all Bloch vectors will be assumed to be collective.

The collective Bloch vector is denoted with a capitol $\vec{J}$ in terms of collective operators $\hat{J}_i = \sum_{i=1}^{N} \hat{j}_i$. An example collective Bloch vector, composed of many individual ones, is shown in Fig. 4.2. The Bloch vector shown represents a coherent spin state (CSS) where every atom is identically prepared in an arbitrary superposition state described by the angles ϕ and θ. However, due to the random projection of each atom when measured, uncertainty arises in the two angles, that is often plotted as a probability distribution of the Bloch vector on the sphere (red distribution). For a CSS on the equator the uncertainties in θ and ϕ are equal, and analogous to the coin flip uncertainty discussed in Chapter 1, $\Delta\phi = \Delta\theta = 1/\sqrt{N}$. This uncertainty is called the standard quantum limit (SQL) for unentangled atoms [173, 74].
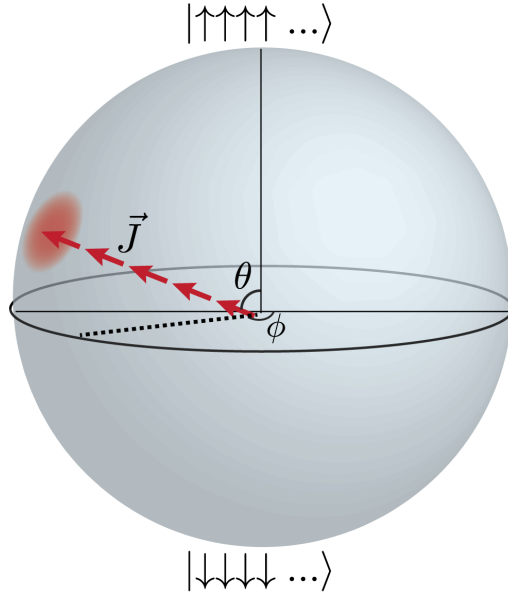
Figure 4.2:   A collective Bloch sphere. The individual projection of each single-atom Bloch vector leads to an uncertainty in the angular resolution of the Bloch vector of $\Delta\theta = \Delta\phi = 1/\sqrt{N}$ for unentangled atoms, called the standard quantum limit.

The angular uncertainty in the Bloch vector can also be interpreted in terms of variances in each component J_α calculated using second order expectation values of the spin operators. For example, $(\Delta J_z)^2 = \langle \hat{J}_z^2 \rangle - \langle \hat{J}_z \rangle^2$. For a coherent spin state on the equator of the Bloch sphere, a common example, $(\Delta J_z)^2 = \sqrt{N}/2$. This spin noise is referred to as quantum projection noise (QPN).

In addition to representing a collective spin state and its uncertainty, Bloch vectors have immense intuitive power for other reasons as well. First, the Bloch sphere can be used to visualize coherent rotations of the atom's quantum state. For any 2-level system or spin-1/2, coherent state rotations can be accomplished by applying an AC field at or near the frequency difference ω_a between $|\uparrow\rangle$ and $|\downarrow\rangle$. Applying a resonant coupling, for example, will cause Rabi flopping of the spin. However, general applied pulses can be used to achieve arbitrary rotations of the Bloch vector. For an applied field with Rabi frequency Ω and detuning δ, the Bloch vector is rotated through an angle $\gamma = \sqrt{\Omega^2 + \delta^2} \times t$ about an axis with polar angle $\theta = \pi/2 + \arctan(\delta/\Omega)$. The azimuthal

angle of the rotation axis is set by the phase of the applied field.

Second, and perhaps most importantly, the equatorial face of the Bloch sphere gives a visualization of the "face" of any atomic clock or quantum sensor. A CSS oriented on the equator will undergo phase oscillation at the difference frequency ω between the $|\uparrow\rangle$ and $|\downarrow\rangle$ states. An atomic sensor operates by measuring the difference in ϕ and the phase of the local oscillator ϕ_{LO}. This phase difference is converted into a population difference using a $\pi/2$ rotation of the Bloch sphere, and the populations of the two state are measured. This sequence is called Ramsey spectroscopy and is ubiquitous among all types of quantum sensors.

4.2   Squeezing

The goal of this work is to create entanglement-enhanced quantum clock hands that have an enhanced resolution in ϕ or θ below the SQL, as shown in Fig. 4.3. In particular, the entanglement enhancement is measured using the Wineland parameter for spin-squeezing $S = (\Delta\theta/\Delta\theta_{SQL})^2$ (or similar for ϕ). One can show that any state with $S < 1$ must be in a nonfactorable, entangled quantum state [149]. Whichever quadrature is squeezed, θ or ϕ, the anti-squeezing quadrature will always have an increased uncertainty given by the Heisenberg uncertainty relation $\Delta\phi\Delta\theta \geq 1/N$.

Over the past 10 years or so, researchers have demonstrated many ways to create spin squeezed states of neutral atoms. Many schemes use unitary interactions between qubits [136, 93, 113, 118, 102, 132, 62, 114, 28, 95]. However, we and others create entanglement using a joint, or collective measurement (sometimes called quantum-nondemolition) [88, 4, 140, 169, 96, 31, 19, 12, 142, 119, 133, 134].

4.3   Joint measurements

To understand how entanglement can be generated with joint measurements, consider a CSS of 4 atoms,

$$|\psi_{CSS}\rangle = \prod_{i=1}^{N=4} \frac{1}{\sqrt{2}}(|\uparrow_i\rangle + |\downarrow_i\rangle). \tag{4.2}$$
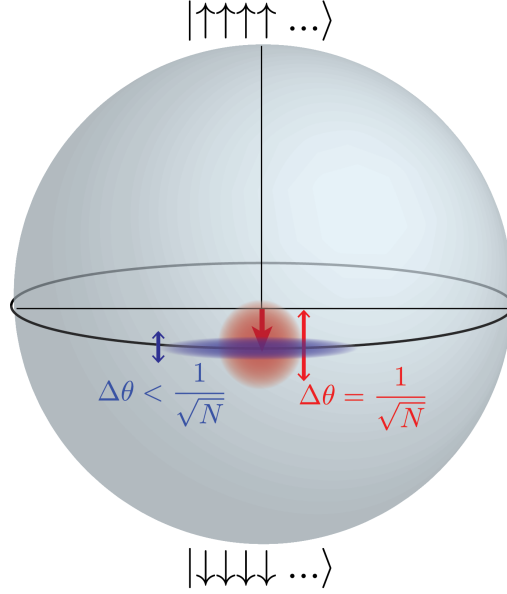
Figure 4.3: A squeezed collective Bloch vector. Entanglement can reduce the quantum fluctuation in an ensemble of atoms or spins, leading to a sharper atomic clock hand. The blue probability is squeezed since it has an angular resolution narrower than the standard quantum limit of $\Delta\theta_{SQL} = 1/\sqrt{N}$. The red distribution represents a coherent spin state made up of identically prepared unentangled atoms.

The number of atoms in $|\uparrow\rangle$ is uncertain in this state. In principle the state could have anywhere from zero to four atoms in $|\uparrow\rangle$. However, one could simply perform a measurement of $N_\uparrow$, the number of atoms in $|\uparrow\rangle$, in a collective way without gaining any information about which atom is in $|\uparrow\rangle$, and if the outcome is $N_\uparrow = 2$, for example, then the resulting state would be,

$$|\psi\rangle = \frac{1}{\sqrt{6}}(|\uparrow\uparrow\downarrow\downarrow\rangle + |\uparrow\downarrow\uparrow\downarrow\rangle + |\uparrow\downarrow\downarrow\uparrow\rangle + |\downarrow\uparrow\uparrow\downarrow\rangle + |\downarrow\uparrow\downarrow\uparrow\rangle + |\downarrow\downarrow\uparrow\uparrow\rangle) \qquad (4.3)$$

that is, in some sense, a maximally squeezed state of the 4 atoms. In fact, unless the outcome of the collective or joint measurement had been $|\uparrow\uparrow\uparrow\uparrow\rangle$ or $|\downarrow\downarrow\downarrow\downarrow\rangle$ the resulting state would be entangled no matter the outcome of the measurement. For a very large number of atoms, such as the 10^5 to 10^6 in our experiment, the outcome of a measurement can be very well approximated by a normal, Gaussian probability distribution $P(\theta) = \frac{1}{\sqrt{2\pi(\Delta\theta_{SQL})^2}}e^{\frac{-\theta^2}{2(\Delta\theta_{SQL})^2}}$ where $\Delta\theta_{SQL} = 1/\sqrt{N}$ is very small. This means that a collective measurement will, essentially, always give an entangled state

near the equator.

The state shown in equation 4.3 is a Dicke state of 4 atoms, which would be drawn as a ring around the equator of the Bloch sphere. In our experiments, our entanglement generating measurements are not precise enough to create such states, but rather we collapse into states that are somewhere in between Eq. 4.2 and 4.3. Such states are a bit difficult to write down, but very easy to plot on the Bloch sphere. These states are the classic "squeezed" states that have reduced uncertainty in the θ direction on the Bloch sphere and an increased uncertainty in the ϕ direction. Of course, since quantum sensors measure the quantum phase ϕ, our squeezed states will need to be rotated $90°$ before use in atomic clocks and most other precision measurements.

One mathematical formalism that can be used to write down and analyze squeezed states is a quantum Baysian formalism [50]. The Baysian formalism simply implements the rule that a quantum state must be consistent with any measurement outcome. In this formalism, one defines a projection operator for a measurement that we write as $\hat{P}_B$. For this work, we can assume that the measurement is a collective measurement that has an outcome of J_{zM} and a measurement uncertainty of ΔJ_{zM}. The collapse operator is then,

$$\hat{P}_B = \frac{1}{A} e^{\frac{(\hat{J}_z - J_{zM})^2}{2\Delta J_{zM}}^2} \tag{4.4}$$

where A is a normalization constant that renormalizes the wave function after the collapse. In the case that the measurement resolution ΔJ_{zM} is much smaller than the original projection noise, this measurement simply collapses the Bloch sphere into a state that is centered around the measurement outcome $J_z = J_{zM}$ with an uncertainty equal to the measurement uncertainty $\Delta J_z = \Delta J_{zM}$. In order to analytically derive the wave function of a squeezed state, one can simply apply the operator of Equation 4.4 to a coherent spin state written in the Dicke basis,

$$\psi_{CSS}(\theta = \pi/2, \phi = 0) = 2^{-N/2} \sum_{i=0}^{N} \binom{N}{i} |N_\uparrow = N - i\rangle_N . \tag{4.5}$$

Since the state collapses around the measurement outcome J_{zM}, this outcome must be recorded and subtracted from any final measurement for the entanglement-enhancement to be

realized. For this reason, this type of squeezing is often called "conditional", since the final measurement is certain conditioned on the premeasurement. However, conditional squeezing is still deterministic in the sense that squeezing is created on every trial. In addition, in chapter ?? we discuss an experiment to use real-time feedback after the measurement in order to create squeezing with a specific targeted population value J_z.

4.4   Quantifying entanglement through spin squeezing

As I have already discussed, spin squeezing is an entanglement metric that quantifies the reduction in a group of atoms' quantum noise. This reduction in spin noise means there must be quantum correlation between the atoms. In fact, the amount of squeezing and the quantum spin correlation can be directly related to each other by writing squeezing in terms of second order moments of the spin operators. Assume a state at the equator of the Bloch sphere is squeezed in the θ direction so that the variance in J_z is reduced $\Delta J_z < \Delta J_{z,SQL}$. I can re-write the spin noise using expectation values of the second order moment, assuming $J_z = 0$,

$$(\Delta J_z)^2 = \langle \hat{J}_z^2 \rangle \tag{4.6}$$

$$= \sum_{\text{all atoms } i,j} \langle \hat{j}_{zi} \hat{j}_{zj} \rangle \tag{4.7}$$

$$= \sum_{\text{all } i} \langle \hat{j}_{zi}^2 \rangle + \sum_{\text{all } i \neq j} \langle \hat{j}_{zi} \hat{j}_{zj} \rangle \tag{4.8}$$

$$= \frac{N}{4} + \sum_{\text{all } i \neq j} \langle \hat{j}_{zi} \hat{j}_{zj} \rangle . \tag{4.9}$$

The expectation value can be written in terms of second order operators of a single atom (line 4.8 first term) and joint operators between each atom (line 4.8 term two). The single atom operators are what lead to the original projection noise $(\Delta J_z)^2 = N/4$ as shown in line 4.9. Any reduction in this quantum noise must come from quantum correlation between the atoms given by, for example, a nonzero expectation value $\langle \hat{j}_{zi} \hat{j}_{zj} \rangle$ for atoms i and j.

In an ideal system, it is reasonable to assume that the correlations would be symmetric among

the atoms so that line 4.9 could then be written without the sum, for arbitrary i and j,

$$(\Delta J_z)^2 = \frac{N}{4} + N^2 \langle \hat{J}_{zi} \hat{J}_{zj} \rangle. \tag{4.10}$$

Additionally, since we assume the state is fully coherent and lies on the equator of the Bloch sphere, we can write the squeezing fully in terms of the spin noise reduction or squeezing, and cancel all the factor of two by writing the quantity in terms of the simple Pauli spin operators,

$$S = \frac{(\Delta J_z)^2}{(\Delta J_{z,SQL})^2} \tag{4.11}$$

$$= 1 + N \langle \hat{\sigma}_{zi} \hat{\sigma}_{zj} \rangle. \tag{4.12}$$

Therefore, in this case, the squeezing is directly expressed in terms of the total atom number and the atom-atom quantum correlation. However, for large atom number, the maximum correlation of a single pair will be whatever is required to fully cancel the original spin noise so that S goes to approximately zero, that is

$$\langle \hat{\sigma}_{zi} \hat{\sigma}_{zj} \rangle_{\text{max}} = -1/N \tag{4.13}$$

However, even though the quantum correlation between two atoms pulled out of the squeezed ensemble may be weak, the total quantum correlation in the system is very high. This is because there are N^2 links between atoms that can be correlated at order $1/N$. The total correlation is then the product of N^2 and $1/N$, namely, N. Therefore, a maximally squeezed state has the same total quantum correlation as N perfectly entangled pairs. In fact, for our best squeezed states wich have $S \approx 1/60$, the total quantum correlation is approximately, $\sum_{\text{all } i \neq j} \langle \hat{\sigma}_{zi} \hat{\sigma}_{zj} \rangle = 390,000$, equivalent to the quantum correlation of 390,000 maximally entangled pairs! This quantity of entanglement is enormous, and created by a single measurement operation. Could there be some way to use joint measurements as an entanglement resource to create, distill, and then harvest the entanglement for quantum information processing or other quantum tasks?

As another note, one other popular entanglement metric for non-classical states has been the so-called "entanglement depth" [150]. This entanglement metric proves that entanglement exists

and gives a minimum provable number of particles that must be participating in an entangled group. However, entanglement depth does not quantify the strength of the quantum correlation/entanglement in the system, and can even be maximal in the limit of infinitesimal quantum correlation. Entanglement depth might be more accurately labeled entanglement *breadth*. For this reason, spin squeezing may provide a more useful metric for thinking of entanglement as a resource for quantum correlations.

4.5   Joint measurements of atoms in a cavity mode

So far the joint measurements have been described in an abstract way that is implementation independent. I will now turn to an overview of how we implement joint measurements by placing the atoms inside an optical cavity mode.

The $|\uparrow\rangle$ and $|\downarrow\rangle$ states are formed in rubidium by the $F = 2$ and $F = 1$ hyperfine ground states, where F is the quantum number labeling total angular moment of the atom including electron spin, orbital angular momentum, and nuclear spin. For all of the work in this thesis we use the stretched $m_F = 1$ and $m_F = 2$ states. The optical cavity is then tuned near resonance to the $|\uparrow\rangle \to |e\rangle$ transition, where $|e\rangle$ is an optically excited state on either the D2 (780 nm) or D1 (795 nm) transition. In this situation, photons in the cavity can be exchanged with atomic excitations, if the atoms begin in $|\uparrow\rangle$. We work in a regime where the number of photons in the cavity is much smaller than the number of atoms, so the excitation fraction is low. In this regime, the atom-cavity system can be approximated (known the Holstein-Primakoff approximation) as two coupled harmonic oscillators. This approximation and formalism is described in detail in Ref. [32], but I will briefly overview the physics here.

Under the Holstein-Primakoff approximation, the atom-cavity system can be approximated by the following Hamiltonian, written for a single excitation, neglecting cavity losses and other decoherence mechanisms, and in matrix form in the $\begin{pmatrix} |\uparrow\rangle|1\rangle \\ |e\rangle|0\rangle \end{pmatrix}$ basis, where $|1\rangle$ represents a photon

in the cavity and $|0\rangle$ represents zero photons in the cavity.

$$H \doteq \hbar \begin{pmatrix} \delta & \Omega/2 \\ \Omega/2 & 0 \end{pmatrix}. \tag{4.14}$$

The cavity mode is detuned by $\delta \equiv \omega_c - \omega_a$ away from the atomic transition ω_a (which is set to zero energy in this Hamiltonian). The collective coupling between the atoms and the cavity mode is defined by Ω, called the vacuum Rabi splitting, where $\Omega = \sqrt{N_\uparrow} 2g$ and $2g$, called the Jaynes-Cummings coupling parameter is the single photon Rabi frequency of atoms in the cavity.

The Eigenstates of this Hamiltonian are characterized by new symmetric and antisymmetric normal modes of the coupled oscillators. The new normal modes of the system are, relative to the nominal atomic transition ω_a

$$\omega_\pm = \frac{\delta \pm \sqrt{\delta^2 + \Omega^2}}{2}. \tag{4.15}$$

Most importantly, the size of the vacuum Rabi splitting (the splitting between the two modes when $\delta = 0$), is dependent on the number of atoms in $|\uparrow\rangle$. This collectively-enhanced mode splitting is the phenomenon that allows us to make a joint measurement of $N_\uparrow$. In general, even if the cavity is detuned off of resonance (taken to be blue detuning here), the atoms cause a shift $\Delta\omega$ to the cavity resonance equal to

$$\Delta\omega = \frac{-\delta + \sqrt{\delta^2 + \Omega^2}}{2} \tag{4.16}$$

that depends linearly on atom number in the dispersive regime, where $\delta^2 \gg \Omega^2$.

In all, by measuring $\Delta\omega$, and knowing our detuning δ, we perform a nondestructive, joint measurement of the number of atoms in $|\uparrow\rangle$. This allows us to project the atoms into a squeezed state. A more complete description of the atom cavity system, the Jaynes Cummings Hamiltonian, etc. can be found in [32]. In the next two sections, I will describe the signal to noise of this probing as well as the fundamental limitation to this scheme from free space scattering.

4.6   Signal to noise when probing

In order to probe the cavity shift $\Delta\omega$, we send probe photons with frequency ω_p at the cavity near the atom-shifted cavity resonance frequency ω_c' . Small changes in the cavity frequency around ω_p will then be imposed as a phase shift on either the transmitted or reflected electric fields. This phase shift can either be measured in a homodyne or a heterodyne detection scheme by interfering the transmitted and reflected light against a reference beam. In the most recent third generation experiments, we have used homodyne phase measurements in reflection, that are advantageous over any heterodyne measurements which are limited to a 50% fundamental quantum efficiency due to gaining both phase and amplitude information from the reflected light (see Section A). However, importantly for this chapter, vacuum fluctuations of the transmitted or reflected field lead to noise variance in the estimated phase ϕ_H of of the homodyne fringe. The homodyne phase can be written as the amplitude of the q-quadrature of the reflected electric field to the nominally maximal i-quadrature, $\phi_H = q(\delta)/i(\delta \approx 0)$ where $\delta = \omega_p - \omega_c'$ is the detuning of the probe from the atom-shifted cavity. The noise in the homodyne phase signal, when sitting at a zero of the q-quadrature, is then

$$(\Delta\phi_H)^2 = \frac{\Delta q}{i_{\max}} = \frac{1}{q_p 4 M_d} \tag{4.17}$$

where M_d is the total number of detected photons as inferred from the voltage on the photodiode and the photodiode sensitivity S. q_p is a quantum efficiency after the detection plane (that is, in this case, taken to be directly in front of the photodetector) that includes detector quantum efficiencies and effective quantum efficiency loss from added technical noise sources in and after the photodetector. The homodyne phase noise leads to noise in the measured cavity frequency $\tilde{\omega}_c$ of,

$$(\Delta\tilde{\omega}_c)^2 = \alpha^2/(q_p 4 M_d) \tag{4.18}$$

where $\alpha^{-1} = \frac{1}{i}\frac{dq}{d\delta}|^{\delta\approx 0}$ is the phase shift of the relfected probe when probing the cavity near resonance. α depends on the input and output cavity linewidths κ_1 and κ_2 and whether one probes in reflection or transmission. The general phase response of the cavity can be found in Ref. [32]. For

probing in reflection in the dispersive regime, the result is,

$$\alpha^{-1} = \frac{4\kappa_1}{\kappa(\kappa - 2\kappa_1)} \tag{4.19}$$

where κ is the full cavity linewidth. For a perfect single-ended cavity with $\kappa_1 = \kappa$, the result simplifies to $\alpha = -4/\kappa$.

Now that we have calculated the photon shot noise in the measurement of the cavity resonance, this noise must be compared to the fluctuations in the cavity resonance induced by fluctuations in the number of atoms in $|\uparrow\rangle$ due to quantum projection noise. As already mentioned, $\Delta J_{z,QPN} = \sqrt{N}/2$. This leads to equivalent fluctuations of $N_\uparrow$, $\Delta N_{\uparrow,QPN} = \sqrt{N}/2$ and fluctuations in the outcome of a single measurement of the cavity resonance frequency of,

$$\Delta\omega_{c,QPN} = \frac{g}{2\sqrt{2}} \frac{\Omega}{\sqrt{\Omega^2 + \delta^2}}. \tag{4.20}$$

Given the quantum projection noise and the noise in probing, we can note that the amount of spin noise reduction R when limited by the fundamental photon shot noise is, $R_{PSN} \equiv (\Delta\tilde{\omega}_c/\Delta\omega_{c,QPN})^2$. In the dispersive regime, one finds, for two equal measurements,

$$R_{PSN} = \frac{\kappa^2\delta^2}{q_p\,\Omega^2\,g^2\,M_d} = \frac{\kappa^2\delta^2}{4q_p\,g^4\,M_d\,N}. \tag{4.21}$$

. Probing with more photons improves this photon shot noise-limited resolution of the cavity, although in practical systems there will be technical noise floors that limit the decrease in R.

4.7 Contrast loss from free-space scattering and optimal squeezing

However, competing with the photon shot noise concern, which demands more probe photons, is contrast loss from free space scattering that worsens as more photons are used to probe the cavity frequency. To lowest order, due to low transverse optical depth, every photon that is emitted into a free space mode reveals whether a single atom is in $|\uparrow\rangle$ or *down* and therefore causes that atom's wave-function to collapse. This causes a reduction in the transverse projection of the Bloch vector, measured by contrast $C \equiv (J_x^2 + J_y^2)/(N/2)^2$. Specifically, $C = e^{-M_s/N}$ where M_s is the total number

of free-space scattered photons. The Wineland squeezing parameter can then be equivalently re-written in terms of R and C as $S \equiv \Delta\theta/\Delta\theta_{SQL} = R/C^2$. This leads to an optimal squeezing, in the far detuned limit of, $S_{opt} = e/2qNC$, again for two equal probing windows, [32] where q is the total quantum efficiency for detecting the probe photons.

For our recent spin-squeezing experiments, this fundamental free-space scattering has been relevant limit to spin squeezing, along with technical noise floors from laser frequency noise and optomechanics (See chapter 6). In addition, spin flips induced by state-changing Raman transitions can also add significant limitations to spin noise reduction and squeezing [32], but these have been significantly reduced by working on optical cycling transitions.

Chapter 5

Improved Bloch Vector Rotations with Reversible Dephasing

In the summer of 2013 we performed an experiment to directly observe over a factor of ten in entanglement enhancement of an atomic clock hand, the largest amount of spin squeezing ever observed at the time [19]. The details of this experiment have been discussed in detail in previous theses [20, 170]. One outcome of this experiment was the realization of the difficulty of performing precise rotations of the atomic Bloch vector necessary for Ransey clock sequences, differential measurements of the Bloch vector, or any quantum information protocol. This difficulty is exacerbated when working on a magnetic field sensitive transition. For this reason, we conducted an experiment to demonstrate a new method to achieve cancellation of certain classes of Bloch vector rotation errors in a collective system using reversible dephasing [41]. In this chapter, I will describe this work.

5.1   Experiment: dephased rotations

Decoherence destroys entanglement, degrades precision measurement signals, and limits a wide range of coherent processes from lasing to operating quantum gates [138, 89]. Therefore, most technologies relying on real or synthetic atoms try to minimize decoherence resulting from loss, relaxation, and inhomogeneous broadening. Recently, however, specifically engineered forms of decoherence have been used to enhance certain processes. Dissipative decoherence, for example, can remove information from a system leading to stabilization of polar molecules from lossy collisions [179] or generation of entanglement [49, 87, 130]. Also, non-dissipative, reversible, decoherence in

the form of inhomogeneous broadening can be used to stabilize coherent operations allowing, for example, storage of non-classical light signals [67], or as we show in this Letter, insensitivity to errors in collective quantum state rotations.

Precision measurements using one or many atoms require precise rotations of the atoms' quantum state. These rotations, achieved by applying a coherent field at or near the atomic transition frequency, are used to excite an atomic transition [127, 17], map the evolution of a quantum phase into a measurable quantity [129, 66], or simply transfer state populations for precision readout [31]. Imperfections in these rotations lead to classical uncertainty in the atoms' quantum state, which can dominate fundamental quantum uncertainty and limit precision measurements.

In this Chapter, I will present an approach to suppress rotation errors using reversible inhomogenous broadening, an alternative to the composite coupling pulses that are often used to correct state rotation errors [160, 172, 78, 98, 161, 151, 128, 157]. I first theoretically show how collective rotations of many qubits can be performed with greatly reduced errors if controlled inhomogeneous broadening of the transition is applied prior to the desired rotation. I also show that collective coherence is restored by reversal of the inhomogeneous broadening after the rotation.

Next I apply dephased rotations in a specific experiment, demonstrating a maximum suppression of technical noise of greater than 21 dB when rotating the internal states of laser-cooled and trapped ^{87}Rb atoms. Dephased rotations aid the generation and observation of entangled, spin-squeezed states with a directly observed enhancement in quantum phase estimation 9.5(5) dB below the standard quantum limit for an unentangled ensemble, one of the largest such enhancements in atomic systems reported to date [19, 103, 62, 113, 95]. In the absence of any reversible inhomogeneous broadening, either incidental or deliberate, we estimate that little to no squeezing would have been observed in this experiment due to imperfections in the required quantum state rotations [1] .

---

[1] A different measurement sequence [19] that avoids any rotations achieved a comparable amount of directly observed spin squeezing in the same system without relying on dephased rotations, but only by sacrificing a factor of two in fundamental measurement resolution. This additional factor of two was not realized in this work due to the probe laser's frequency noise coupling more strongly into the measurment sequence of Fig. 5.3
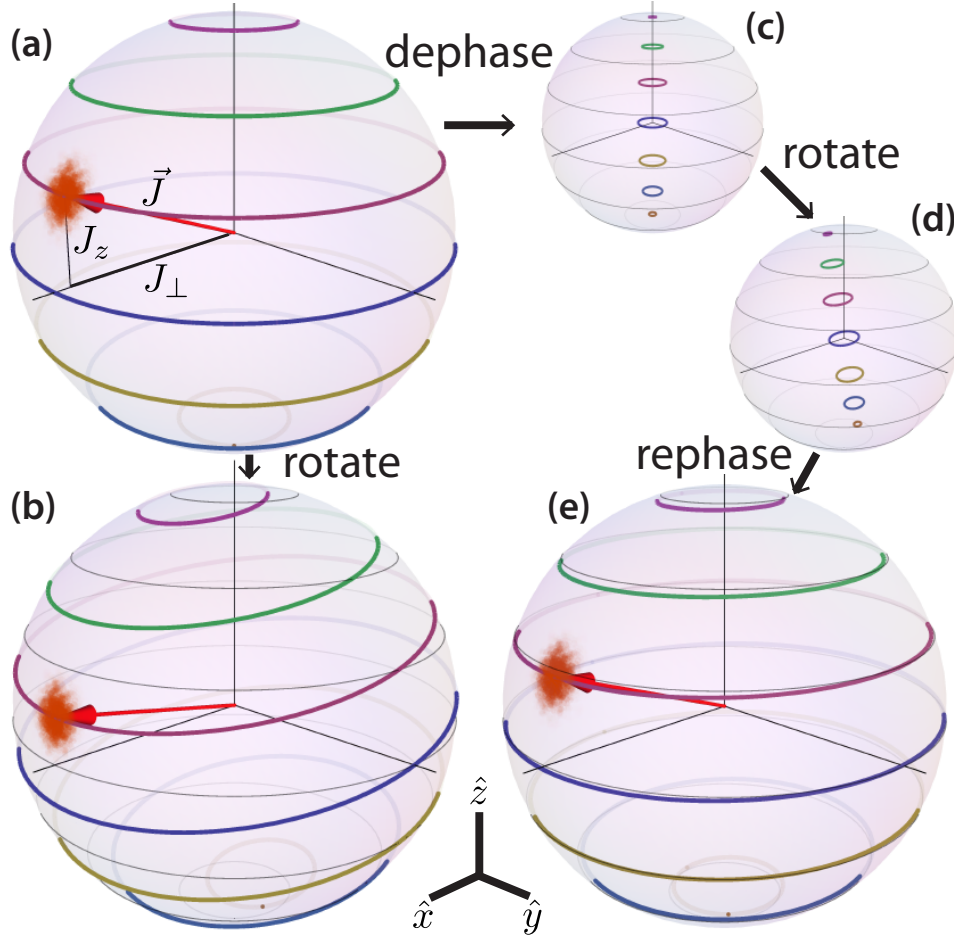
Figure 5.1: The reduced sensitivity of a dephased rotation to a small rotation error is graphically represented on collective Bloch spheres. A single representative Bloch vector prepared in the $\hat{x} - \hat{z}$ plane, along with the quantum uncertainty in its position, is shown (red arrow and noise distribution). Each sphere also has a series of colored lines denoting the tips of Bloch vectors that are at a constant J_z in the initial configuration. The original rings of constant J_z are shown in parts (b-e) as thin black lines for reference. A small rotation $\mathcal{R}_{\hat{y}}(\pi/16)$ representing an error is applied without (b) and with (c,d,e) dephasing. By reversibly dephasing the Bloch vector to $C_d = 0.14$, the impact of the rotation is greatly reduced. Rotation errors that would otherwise dominate can be supressed well below the fundamental quantum noise.

Dephased rotations are a general concept and could be applied to a variety of applications, having several advantages over traditional composite rotation sequences. Composite sequences rely on cancellation between the errors of each individual rotation. However, cancellation fails if the errors fluctuate on time scales comparable to the time required for the composite pulse sequence. Furthermore, increasing the rate of rotations to enhance the correlation in errors may actually be detrimental depending on the form of the noise spectrum [33]. Lastly, composite pulses require precise control over the phase of the coupling field, and the most effective composite sequences require many pulses, increasing the time required for a measurement sequence. The approach presented here to a large degree avoids these requirements. We note that intense efforts to apply composite pulses to reduce rotation-added noise were largely unsuccessful in our experiment.

We describe our system of N 2-level atoms as spin-1/2 particles using a collective Bloch vector $\mathbf{J} = J_x \hat{x} + J_y \hat{y} + J_z \hat{z} = \Sigma_{i=1}^{N} \mathbf{J}_i$, where the ith Bloch vector $\mathbf{J}_i = \langle \hat{\mathbf{J}}_i \rangle$ is the expectation value of the quantum spin projection operator for the ith atom. The $\hat{z}$ projection of the collective Bloch vector $J_z \equiv \mathbf{J} \cdot \hat{z} = (N_\uparrow - N_\downarrow)/2$, is directly determined by measuring the number of atoms in spin up $N_\uparrow$ and down $N_\downarrow$. Precision measurements with 2-level systems are fundamentally limited by quantum uncertainty in the angles describing the orientation of the Bloch vector. This quantum uncertainty appears as quantum projection noise (QPN) in the measurement of the spin projection J_z. For unentangled atoms, the rms fluctuation for a coherent spin state (CSS) with $\mathbf{J} = N/2 \, \hat{x}$ is $\Delta J_{z,QPN} = \sqrt{N}/2$. The projection noise limits the estimate of the Bloch vector's polar angle to an rms uncertainty of $\Delta \theta_{SQL} = 1/\sqrt{N}$, the so-called standard quantum limit (SQL). Due to this scaling, states with large N are desirable for precise phase estimation, but in these states, classical rotation errors become more challenging to reduce below the smaller SQL.

The rotation of the ith Bloch vector through angle ψ_i about an axis $\hat{n}$ is defined by the rotation matrix $\mathcal{R}_{\hat{n}}(\psi_i)$. If the rotation is uniform ($\psi_i = \psi$ for all i) then the result is a rigid rotation in which the length of the Bloch vector is conserved. The errors we wish to suppress are those generated by uniform rotation errors associated with the coupling field, in particular, an arbitrary erroneous rotation through a small angle ϕ described by $\mathcal{R}_{\hat{n}}(\phi)$. The suppression of

the rotation errors will be achieved by introducing a brief, controlled inhomogeneous broadening of the energy difference between $|\uparrow\rangle$ and $|\downarrow\rangle$ before and after the imperfect rotation. The time-integrated effect of the broadening on the ith vector is characterized by the non-uniform rotation $\mathcal{R}_{\hat{z}}(\psi_i)$. The amount of dephasing is quantified by the fractional reduction in the collective Bloch vector's transverse projection $J_\perp \equiv \sqrt{J_x^2 + J_y^2}$. Specifically, we define the transverse coherence $C_d = J_{\perp d}/J_{\perp 0}$, where the subscript d refers to $J_\perp$ after dephasing and 0 refers to $J_\perp$ prior to dephasing. In the present work, the inhomogeneous broadening will be achieved through light shifts, but could also be realized through magnetic fields or electric fields. Whatever method is used, the key is that the dephasing must be reversible: at a later time the opposite rotation can be realized $\mathcal{R}_{\hat{z}}(-\psi_i)$ to fully or partially undo the dephasing. Here the dephasing will be undone by using a π-pulse (e.g. $\mathcal{R}_{\hat{y}}(\pi)$) followed by identical inhomogeneous broadening.

To theoretically show that dephased collective spin vectors are protected from small rotation errors, we analyze the rotation error of a nominal π-pulse, with fractional amplitude error ϵ and detuning error δ of the applied coupling field from the atomic transition, that is preceded and followed by dephasing steps. The final Bloch vector after such a sequence is

$$\mathbf{J}_F = \Sigma_{i=1}^N \mathcal{R}_{\hat{z}}(\psi_i)\mathcal{R}_{\hat{\gamma}}(\beta)\mathcal{R}_{\hat{z}}(\psi_i)\mathbf{J}_{i0} \,, \tag{5.1}$$

where the subscript F indicates a quantity after all rotations.

The effective rotation angle is a function of both ϵ and δ and can be written $\beta = \pi\sqrt{(1+\epsilon)^2 + \delta^{*2}}$ where $\delta^* = \delta/\Omega$ and Ω is the on resonance Rabi frequency of the applied rotation. In the rotating frame of the applied field, the rotation axis depends on the detuning error, $\hat{\gamma} \propto \Omega\hat{\alpha} + \delta\hat{z}$. For an arbitrary initial Bloch vector, the rotation axis $\hat{\alpha} = \hat{y}$ can be chosen without loss of generality.

As an example, we assume that the inhomogeneous phase rotation angles ψ_i are drawn from a Gaussian distribution with mean of zero and rms value σ. The reduction in transverse coherence due to the applied inhomogeneous broadening in this case is $C_d = e^{-\sigma^2/2}$. The complete sequence of applied broadening and imperfect rotations can then be averaged over all atoms to compute the final Bloch vector $\mathbf{J}_F$ with solution,

$$
\begin{pmatrix} J_{xF} \\ J_{yF} \\ J_{zF} \end{pmatrix} \approx - \begin{pmatrix} J_{x0}(1-\eta^2) + C_d \pi \epsilon J_{z0} \\ J_{y0}(1-\eta^2) - C_d 2\delta^* J_{z0} \\ J_{z0}(1-2\eta^2) - C_d(2\delta^* J_{y0} + \pi \epsilon J_{x0}). \end{pmatrix} \tag{5.2}
$$

where $\eta^2 \equiv \pi^2 \epsilon^2/4 + \delta^{*2}$. We have assumed here that $\pi \epsilon$, δ^*, and $C_d \ll 1$, and neglected all terms of third order in products of these quantities.

The key result is that all rotation errors that are first order in $\pi \epsilon$ and δ^* are reduced by a factor C_d. The cost of this error suppression is shortening of the Bloch vector, but only at second order in the rotation error η. The final transverse Bloch vector component $C_F = J_{\perp F}/J_{\perp 0}$ is reduced as $C_F \approx 1 - \eta^2$, and the $\hat{z}$ projection of the Bloch vector is reduced to $J_{zF}/J_{z0} \approx 1 - 2\eta^2$.

Fig. 1 graphically demonstrates the reduced sensitivity of an arbitrary CSS to a rotation about an axis on the equator. The rings of constant color indicate the location of the tips of the Bloch vectors with equal J_z at the beginning of a rotation sequence (top left). Subsequent steps indicate how these points are mapped to new positions due to rotations and dephasing, with the initial ring locations shown in black for reference. The figure depicts the effect of an error $\pi \epsilon = \pi/16$, $\delta^* = 0$ rotation about the y-axis with and without dephasing to $C_d = 0.14$, a reasonable experimental value. Without dephasing, the rotation error can cause angular deflections greater than the representative quantum noise distribution (shown for $N = 120$ for visual clarity). With dephasing, the rotation error is greatly reduced, causing negligible error compared to the quantum noise.

The dephased rotation scheme exhibits an additional useful attribute for suppressing rotation errors in the generation and manipulation of spin-squeezed ensembles. Dephased rotations can significantly reduce the amount of anti-squeezing projected into the low noise squeezed quadrature by a rotation error. We show this theoretically in the Supplementary Material.

We apply the proposed scheme to collective measurements of $N = 2.1 \times 10^5$ to $N = 5 \times 10^5$ ^{87}Rb atoms laser-cooled and trapped inside an optical cavity of finesse $F = 660$ (see ref. [19] for experimental details). The atoms are tightly confined by a 1D optical lattice formed by exciting
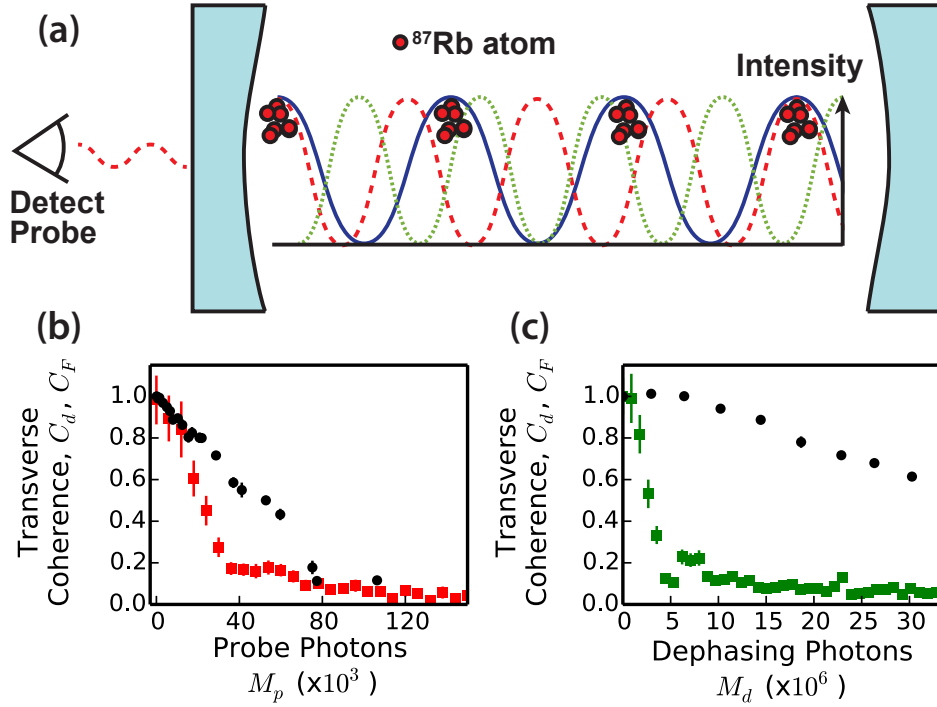
Figure 5.2: (a) The standing wave intensity of each beam is shown inside the cavity (blue mirrors). The atoms are trapped at antinodes of the 823 nm optical lattice (blue). The probe laser at 780 nm (red dashed) and dephasing beam at 795 nm (green dotted) cause dephasing due to their inhomogeneous light shifts. We detect the phase of the probe light to infer $N_\uparrow$. (b,c) The reduction in transverse coherence after dephasing C_d (red and green squares) and rephasing C_F (black circles) is measured versus the average number of transmitted photons from the probe beam (b) and dephasing beam (c).

a longitudinal TEM_{00} mode of the cavity with wavelength $\lambda_l = 823$ nm. The atoms fill lattice sites long the central 2 mm of the cavity. The spin system is defined by hyperfine ground states $|\uparrow\rangle = |F = 2, m_f = 2\rangle$ and $|\downarrow\rangle = |F = 1, m_f = 1\rangle$. Coherent rotations between these states are performed by applying microwaves at the transition frequency 6.83 GHz. $N_\uparrow$ can be inferred by measuring the dispersive frequency shift of another TEM_{00} cavity mode tuned ≈ 200 MHz from resonance with the optical transition between $|\uparrow\rangle$ and an excited state $|e\rangle = |F' = 3, m_f = 3\rangle$ on the 780 nm D2 line [19].

The probe light at $\lambda_p = 780$ nm that is used to measure the cavity frequency shift and infer $N_\uparrow$ also creates an inhomogeneous light shift that dephases the atoms. Since the standing waves of the lattice and probe are incommensurate ($\lambda_p \neq \lambda_l$), the atoms at different lattice sites experience different light shifts from the probe, leading to dephasing (shown in Fig. 5.2).

We can also apply an additional dephasing laser tuned to resonance with yet another TEM_{00} longitudinal mode of the cavity. This dephasing beam is detuned ≈ 50 GHz from the 795 nm D1 optical transition and allows us to modify the amount of dephasing without modifying the signal to noise of the atom number probe or causing additional unwanted free-space scattering. The 795 nm beam also serves to dephase the sub-class of atoms at lattice sites that are at anti-nodes of the probe mode (see Fig. 5.2(a)). Because the atoms are tightly confined with respect to the cavity axis, the same light shifts can be applied at a later time. after a π-pulse, to reverse the applied phase shifts.

We can measure C_d due to dephasing from the probe and dephasing lasers by first preparing a coherent spin state along $\hat{x}$. We then apply either the probe or dephasing laser for a varying amount of time, after which we apply the rotation $R_{\hat{\alpha}}(\pi/2)$ about a random axis $\hat{\alpha}$ lying in the $\hat{x}$-$\hat{y}$ plane. Lastly, we measure the number of atoms $N_\uparrow$. When averaged over all rotation axes, the standard deviation of $N_\uparrow$ is proportional to C_d. In Fig. 5.2(b) and (c), C_d and C_F are plotted versus the average number of probe M_p and dephasing M_d photons transmitted through the cavity. For small M_d the transverse coherence only shows second order reduction ($1 - C_F \propto M_d^2$), due to the large detuning of the dephasing beam from the optical transition. In contrast, for small M_p

the transverse coherence loss is linear $(1 - C_F \propto M_p)$ due to the higher probability of single-atom wave function collapse from free-space scattering of probe photons.

In Fig. 5.3(a) we demonstrate reduced sensitivity to rotation noise arising from environmental noise sources using our dephased rotation scheme. Data showing reduced sensitivity to intentionally applied rotation errors can be found in the Supplementary Material. In our experiment, undesirable environmental rotation noise arises primarily from microwave amplitude noise and frequency fluctuations in the magnetic field-sensitive hyperfine transition. To demonstrate a reduction in sensitivity to environmental noise sources, J_{zF} is measured after a large even number of π-pulses. With increased dephasing, the rotation-added noise can be reduced below QPN even after eight π-pulses.

We now show how dephased rotations can be used in experiments to generate entangled, spin squeezed states by making precise collective measurements of the spin projection J_z. These experiments are treated in detail in a related work [19]. Here we primarily emphasize the role dephased rotations can play, enabling large reductions in technical rotation noise and allowing resolution of the spin projection far below the quantum projection noise level. In our experiment, dephased rotations are highly advantageous to composite pulse sequences because they do not require any control of the applied rotation axis and do not increase the duration of the measurement sequence, which would increase sensitivity to low frequency noise.

To verify that the noise in J_z is below QPN, two consecutive measurements of J_z, labeled $J_{z,p}$ and $J_{z,f}$ must be correlated below $\Delta J_{z,QPN}$. The degree of spin noise compared to quantum projection noise is characterized by the spin noise reduction $R = [\Delta(J_{z,f} - J_{z,p})]^2 / \Delta J_{z,QPN}^2$, where $\Delta(J_{z,f} - J_{z,p})$ is the standard deviation in the differential quantity $J_{z,f} - J_{z,p}$. The measurement sequence for R is shown in Fig. 5.3(b). The spin noise reduction has two contributions $R = R_{\mathrm{bck}} + R_{\mathrm{rot}}$. One, R_{bck}, we attribute to measurement imprecision of the experiment along with measurement back-action. The other, R_{rot}, is rotation-added noise from the two π-pulses in the measurement sequence. We estimate R_{bck} (black line in Fig. 5.3(c)) by performing the measurement sequence of 5.3(b) without the π-pulses. The experiment is then repeated with the π-pulses
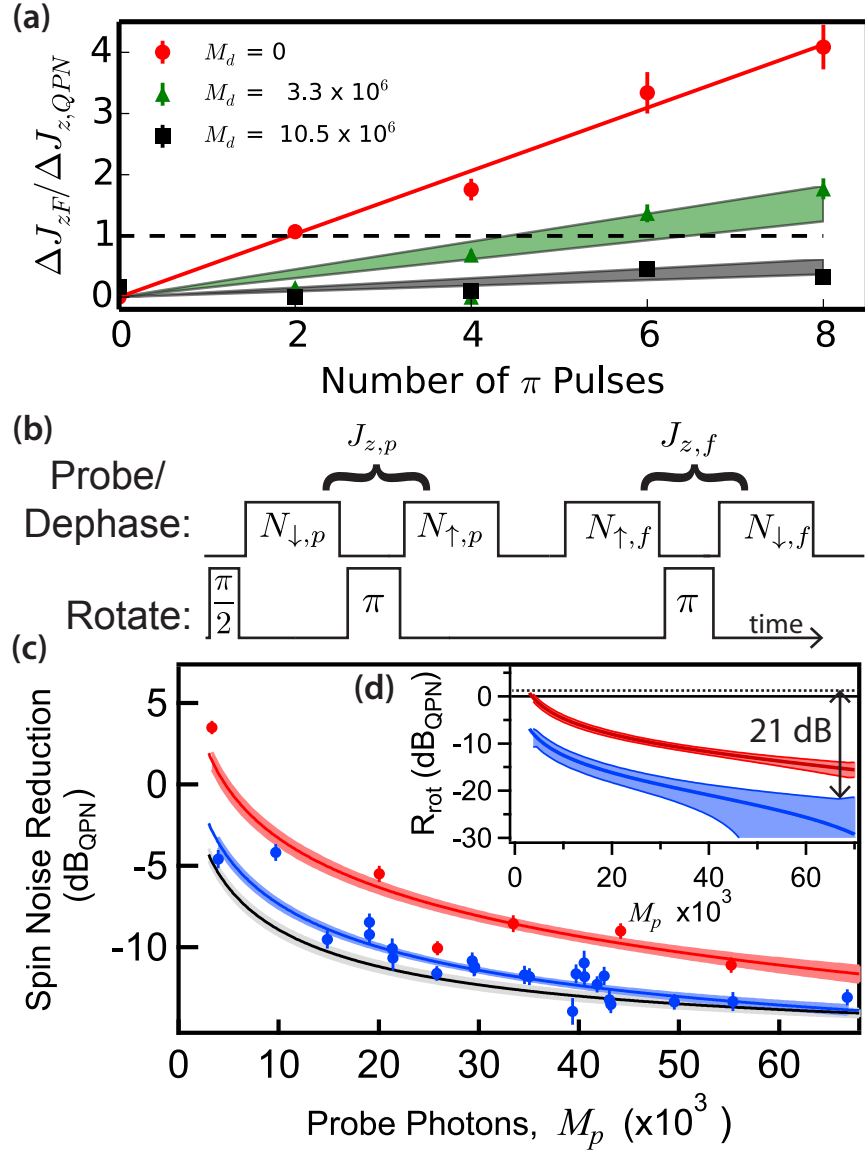
Figure 5.3: (a) The rms noise in the measured spin projection J_{zF}, ΔJ_{zF}, after applying an integer number of π-pulses is displayed for three different amounts of applied dephasing, quantified by M_d. The contribution to ΔJ_{zF} due to finite measurement resolution (i.e. ΔJ_{zF} at 0 π-pulses) is subtracted out. For $M_d = 0$, a linear fit extracts the rotation-added noise per pulse (red line). Predictions (green and black bands) using C_d from Fig. 5.2 reasonably explain the reduction in rotation-added noise with increased M_d. All shaded regions represent 68% confidence intervals. (b) Dephased rotations are applied in a sequence designed to resolve spin populations below QPN. $N_\uparrow$ is measured before and after a π-pulse with outcomes labeled $N_{\uparrow,p}$, $N_{\downarrow,p}$, $N_{\uparrow,f}$ and $N_{\downarrow,f}$ to determine the spin noise reduction R. Both the 780 nm probe and 795 nm dephasing beams are applied during each measurement of $N_\uparrow$ and $N_\downarrow$. (c) R is measured as a function of probe strength M_p for $M_d = 6.1(3) \times 10^6$ (blue data and fit) and $M_d = 0$ (red data and fit). All quantities are displayed in units of dB relative to QPN, dB$_{\text{QPN}}$. The fit to the measurement background R_{bck} is shown in black. (d) The rotation-added noise R_{rot}, shown in the inset, can be inferred from the data of part (c). R_{rot} with no dephasing is shown as a dashed line. Dephasing can reduce R_{rot} by more than 21 dB.

included, and any increase in R is assigned as rotation-added noise R_{rot}.

In Fig. 5.3(c), the measured spin noise reduction and measurement background are shown versus M_p (transmitted probe photons in a single measurement window). With the probe beam alone (i.e. $M_d = 0$), the spin noise reduction R (red data and fit) lies well above the measurement background R_{bck} (black line). However, when the additional dephasing is applied with strength $M_d = 6.1(3) \times 10^6$, the observed R (blue points and fit) is improved to values very close to the measurement background.

Fig. 5.3(d) (inset) displays the inferred rotation-added noise R_{rot} with and without the additional dephasing applied (blue and red lines respectively). The combined dephasing of the probe and dephasing beams allows a reduction of the rotation-added noise of greater than approximately 21 dB compared to the original rotation noise with no dephasing (i.e. $R_{\mathrm{rot}} \approx 0$ dB$_{\mathrm{QPN}}$ when $M_p = 0$ and $M_d = 0$) enabling up to $R = 13(1)$ dB of spin noise reduction below the QPN at 2.1×10^5 atoms.

The rephasing nearly completely restores coherence, as demonstrated in Fig. 5.2. As a result, the state generated after the premeasurement can be viewed as a determinstically generated spin-squeezed state (i.e. no post-selection), conditioned on knowledge of the measurement outcome $J_{z,p}$ on a given trial. After accounting for both the degree of spin-noise reduction R and the loss of coherence C_F, the optimum measurement sequence with dephasing provides a directly observed enhanced phase resolution 9.5(5) dB below the SQL. In contrast, without any reversible dephasing, rotation-added noise would have precluded the observation of any enhancement beyond the SQL.

5.2   Reduction of applied frequency and amplitude errors

The main text shows both experimentally and theoretically that dephasing reduces an ensemble's sensitivity to collective rotation errors arising from imperfections in the coupling field used for state manipulation. To gain intuition, consider the case when the initial Bloch vector lies on the equator of the Bloch sphere ($J_z = 0$). In this case, the length of the dephased Bloch vector J_d is reduced, by definition of C_d, to $J_d = C_d J_0$. Since the length of the Bloch vector is reduced by

C_d, the possible change in the Bloch vector's J_z projection due to a rotation must also be reduced by C_d.

Fig. 5.4 demonstrates this reduced sensitivity to intentionally applied rotations representing amplitude and frequency errors in the coupling field. Measurement sequences are shown at the bottom of Fig. 5.4. A $\pi/2$-pulse initializes the Bloch vector at the equator (black pulse). Dephasing is applied with a strength characterized by the average number of photons transmitted through the cavity M_d (yellow pulse). A rotation representing an error (either amplitude (a) or detuning (b)) is applied, after which $N_\uparrow$ is measured by measuring the shift of the optical cavity resonance frequency[19, 32]. From the measured $N_\uparrow$, we infer the z-projection of the final Bloch vector J_{zf}.

For part (a), the applied rotation is $\mathcal{R}_{\hat{\alpha}}(\psi)$, where ψ is the arbitrary rotation amplitude, and $\hat{\alpha}$ is a random rotation axis lying in the $\hat{x} - \hat{y}$ plane of the Bloch sphere. J_{zf} (blue points) is plotted as a function of the applied amplitude ψ for three different values of dephasing. The randomization of $\hat{\alpha}$ causes large scatter of J_{zf} over positive and negative values. To compare with an expectation, we plot the average magnitude of the measured J_{zf} in red, and a prediction based on the independently measured transverse coherence C_d from Fig. 2 of the main text is shown as a black line. The envelope of the data decays linearly with C_d in reasonable agreement Eq. 2 in the main text and our intuitive expectation.

To demonstrate the reduction in sensitivity to rotations for which the coupling field is detuned from the atomic resonance frequency, we apply a nominal π-rotation with variable detuning. The applied rotation is $\mathcal{R}_{\hat{\gamma}}(\pi\sqrt{1 + \delta^{*2}})$ where $\hat{\gamma} \propto \Omega\hat{\alpha} + \delta\hat{z}$, and the azimuthal axis $\hat{\alpha}$ is randomized between each trial. $\delta^* = \frac{\delta}{\kappa/2}$ is the detuning of the coupling field from atomic resonance in cavity half-widths. In Fig. 5.4(b), J_{zf} (blue points) is plotted versus δ^* for three different values of M_d, and the average magnitude of J_{zf} (red points) are compared to a prediction (black line). Just as with the amplitude errors, the magnitude of the deflections of J_{zf} scale linearly with C_d in good agreement with the prediction.
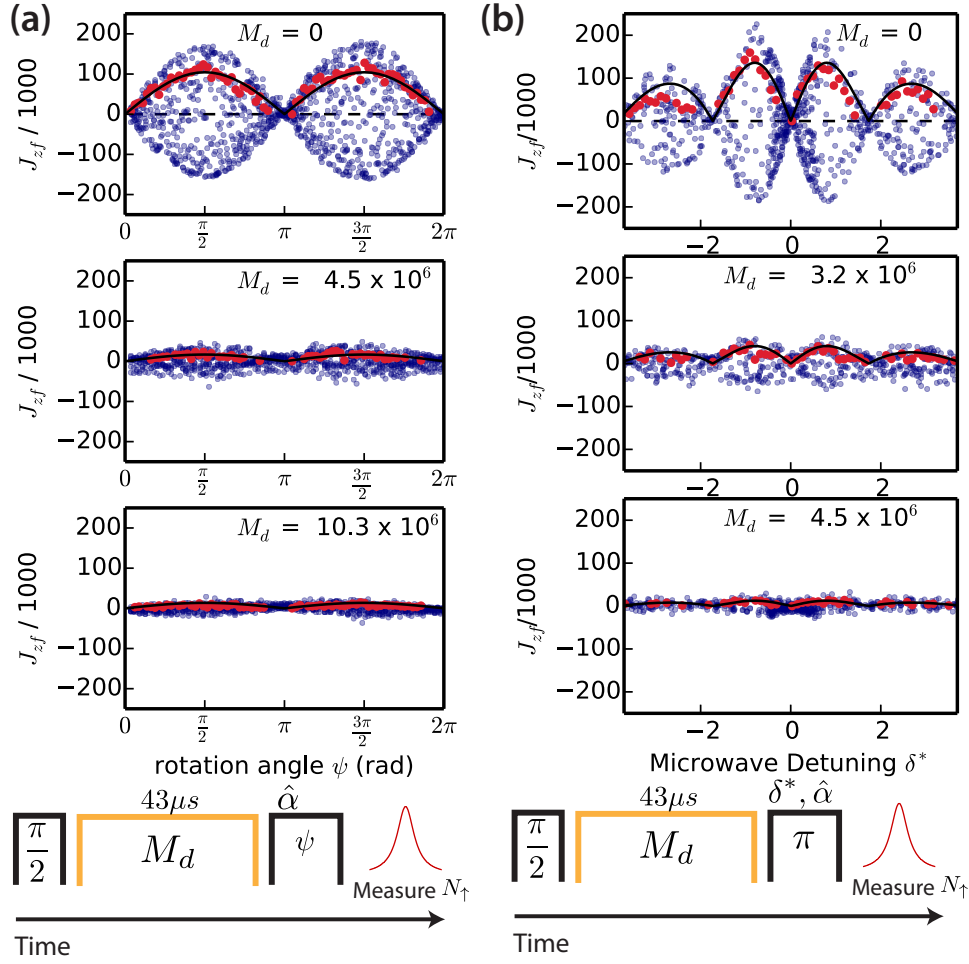
Figure 5.4: Reduction in sensitivity to amplitude and frequency rotation errors. (a) The ensemble is subjected to a rotation with arbitrary amplitude ψ and equitorial rotation axis $\hat{\alpha}$ and zero detuning (measurement sequence shown below graph). The resulting J_{zf} (blue points) are plotted versus amplitude of the rotation ψ for three different values of dephasing, characterized by M_d. At each amplitude the average magnitude of J_{zf} (red points) is compared to a prediction using the measured transverse coherence from Fig. 2 (black line). (b) The ensemble is subjected to a rotation with aribitrary detuning δ^* and azimuthal rotation axis $\hat{\alpha}$. The amplitude is constrained so that at zero detuning, the rotation is a π-pulse. J_{zf} (blue points) are plotted as a function of δ^*, again for three different values of dephasing, and the average magnitude of J_{zf} (red points) is in agreement to a prediction from the measured transverse coherence (black line).

5.3   Dephased rotation of quantum noise

When dealing with spin squeezed states, classical rotation errors can rotate the anti-squeezed quadrature of a system into the measurement basis. This leads to additional noise above the noise in classical rotation errors primarily considered in the main text. In this section, we treat this problem theoretically with a fully quantum mechanical description of the spin state, instead of treating each spin as a classical vector as in the main text. We show that dephasing protects squeezed noise distributions from rotation of the anti-squeezed spin projection into the originally squeezed quadrature.

We assume for simplicity that there is an arbitrary initial state oriented along $\hat{y}$ with a squeezed noise distribution in $\hat{J}_z$ (and anti-squeezed in $\hat{J}_x$). The state is subjected to a small rotation amplitude error of size $\pi\epsilon$ around the $\hat{y}$-axis which rotates the anti-squeezed spin projection into the z quadrature. The initial squeezed noise distribution is characterized by the second order expectation value

$$\langle \hat{J}_z^2 \rangle_0 \equiv \langle \psi_0 | \, \hat{J}_z^2 \, | \psi_0 \rangle \,, \tag{5.3}$$

where $| \psi_0 \rangle$ describes the initial state. We wish to evaluate the noise distribution of $\hat{J}_z$ for the final state,

$$\langle \hat{J}_z^2 \rangle_f \equiv \langle \psi_f | \, \hat{J}_z^2 \, | \psi_f \rangle \,, \tag{5.4}$$

where the final state $| \psi_f \rangle$ can be written in terms of $| \psi_0 \rangle$ using the dephasing operator

$$\hat{D} \equiv \prod_i^N \hat{R}_{\hat{z}}(\theta_i) \tag{5.5}$$

and rotation operator (around $\hat{y}$) $\hat{R}_{\hat{y}}(\pi\epsilon)$, $| \psi_f \rangle = \hat{D}^\dagger \hat{R}_{\hat{y}}(\pi\epsilon) \hat{D} \, | \psi_0 \rangle$. For now, we do not need to specify a specific form of dephasing (i.e. the inhomogeneous rotations θ_i). Using the dephasing and rotation operators, Eq. 5.4 becomes

$$\langle \hat{J}_z^2 \rangle_f = \langle \psi_0 | D^\dagger \hat{R}_{\hat{y}}(\pi\epsilon)^\dagger \hat{D} \hat{J}_z^2 \hat{D}^\dagger \hat{R}_{\hat{y}}(\pi\epsilon) \hat{D} | \psi_0 \rangle . \qquad (5.6)$$

The rotation operators can be written in terms of single atom spin projection operators as, to second order in the small parameter $\pi\epsilon$,

$$\hat{R}_{\hat{y}}(\pi\epsilon) \approx \prod_k^N (\mathbb{I}_k + i\pi\epsilon\hat{J}_{\hat{y},k} - \frac{(\pi\epsilon)^2}{2}\mathbb{I}_k), \qquad (5.7)$$

where $\mathbb{I}_k$ is the identity operator for the kth atom, and the collective spin projection operator $\hat{J}_{\hat{y}}$ can be written as a sum over all atoms' individual spin operators $\hat{J}_{\hat{y}} = \sum_i^N \hat{\mathbf{J}}_i \cdot \hat{y}$. Using these definitions and single atom commutation relations, we simplify Eq. 5.6 keeping to second order in ϵ,

$$\langle \hat{J}_z^2 \rangle_f = \langle \hat{J}_z^2 \rangle_0 + (\pi\epsilon)^2 \langle \hat{J}_x^2 \rangle_d - (\pi\epsilon)^2 \langle \hat{J}_z^2 \rangle_0 + 2\pi\epsilon \langle \hat{J}_z \hat{J}_x \rangle_d. \qquad (5.8)$$

The expectation values in the second and final terms (with subscript d) are calculated with respect to the dephased state, $|\psi_d\rangle = \hat{D} |\psi_0\rangle$. This equation is particularly useful because it gives the quantum noise rotation in terms of measureable quantities for an arbitrary form of the dephasing.

For squeezed states oriented along $\hat{y}$ with symmetry around $\hat{x}$ and $\hat{z}$ (generated, for example, by 2-axis twisting or quantum non-demolition measurement [32, 79]) the final term in Eq. 5.8 is zero, giving

$$\langle \hat{J}_z^2 \rangle_f = \langle \hat{J}_z^2 \rangle_0 + (\pi\epsilon)^2 \langle \hat{J}_x^2 \rangle_d - (\pi\epsilon)^2 \langle \hat{J}_z^2 \rangle_0. \qquad (5.9)$$

This result shows that the back-action quadrature is introduced at order ϵ^2 through $\langle \hat{J}_x^2 \rangle_d$ instead of $\langle \hat{J}_x^2 \rangle_0$. In the limit of random Gaussian dephasing (as considered in the main text), $\langle \hat{J}_x^2 \rangle_d$ can be written,

$$\langle \hat{J}_x^2 \rangle_d = C_d^2 \langle \hat{J}_x^2 \rangle_0 + (1 - C_d^2)\Delta J_{QPN}^2. \qquad (5.10)$$

In the limit of small and moderate dephasing, the standard deviation of the back-action quadrature that is rotated into $\hat{z}$ is reduced linearly with C_d (first term). However, for complete random dephasing, the back-action can only be reduced to the quantum projection noise level for a CSS, $\Delta J_{QPN} = \sqrt{N}/2$ as seen by the second term. Applying greater dephasing provides marginal returns when the two terms in Eq. 5.10 become equal. This occurs at a value of C_d which we label C_d',

$$C_d'^2 = \frac{1}{1 + \langle \hat{J}_x^2 \rangle_0 / \Delta J_{QPN}^2}. \qquad (5.11)$$

For a spin squeezed state with a large back-action quadrature, $\langle \hat{J}_x^2 \rangle_0 \gg \Delta J_{QPN}^2$, more dephasing is required to reduce $\langle \hat{J}_x^2 \rangle_d$, the dephased back-action projection, to near the QPN level.

Chapter 6

3rd Generation Spin Squeezing and Deterministic Squeezing with Feedback

6.1   Introduction

After achieving a factor of 10 in squeezing, the obvious question arose: how could we reach a factor of 100? Working on the cycling transition had effectively removed the limit to squeezing due to Raman spin flips, $S = \sqrt{8p/(qNC)}$ where p is the probability for a free space scattered photon to cause a Raman spin flip, q is the total quantum efficiency for detecting cavity photons, and NC is the collective cooperativity [32]. The new observed squeezing was instead limited by decoherence from free space scattering, laser frequency noise, and noise induced from atomic motion due to optomechanical forces [19]. These issues prompted a third spin squeezing attempt which achieved a factor of 59 in spin squeezing and was realized through significant engineering improvements and a rebuilt experiment in the basement of the JILA X-wing.

One of the primary improvements was a significant increase in the quantum efficiency q for detecting probe light. This lead to a reduction in optomechanics, since more spin resolution could be gained with lower probing power, and an improvement in the fundamental limit due to free space scattering $S = 1/(qNC)$. In the 2nd generation experiment, we only reached a quantum efficiency of $q \approx 5\%$, limited by a 50% lossy optical cavity, use of heterodyne detection, various small losses due to detecting both sides of the symmetric optical cavity, path efficiency, quantum efficiency of silicon photodetectors, and technical noise in the AD8015 transimpedance amplifiers used for heterodyne detection [19].

By building a new, lower loss, single-ended optical cavity and moving to homodyne detection

with a custom detector sensitive at both DC (for homodyne) and AC (for path length stabilization), we achieved a quantum efficiency in a single measurement of nearly 40%, roughly 8 times better than in the second generation. This new system and quantum efficiencies are described in detail in Sect. 6.4.

In generation 2, the frequency stabilization of the probing laser was achieved by narrowing Photodigm DBR lasers with a long external optical cavity [100]. Details of this technique can be found in Ref. [170]. Using this technique, the optimum frequency resolution of the optical cavity which was achieved was approximately 20 kHz rms, or 17 dB below the typical projection noise driven fluctuation of the cavity freqeuency of 140 kHz [19]. In order to improve this floor to achieve close to 20 dB of directly observed squeezing, we implemented a relative stabilization of the atomic probe laser to the cavity using an additional "cavity probe" laser resonant with another TEM_{00} optical cavity mode 122 GHz away from the D2 atomic transition. This system achieved frequency resolution of the cavity of approximately 5 kHz and is explained in detail in Sect 6.4.

In all, these and other engineering improvements lead to a directly observed squeezing of 17.7(6) dB below the standard quantum limit using 4×10^5 atoms. This result, along with the similar result reported by [68] is the largest entanglement enhancement of any kind in atomic or optical systems.

Further, with this new spin squeezing apparatus, we demonstrated real-time feedback to a squeezed state to create so-called "deterministic" squeezing, where the result of the pre-measurement is no longer necessary to obtain enhanced resolution. Using this real-time feedback we created one of the largest amounts of deterministic squeezing ever observed, comparable to the amounts generated by the best naturally deterministic schemes such as 1-axis twisting using cavity feedback or collisions in an ultra-cold gas [95, 62].

In this Chapter, in Sections 6.2 and 6.3, I will first present the primary results from the third generation of spin squeezing experiment. Then, I will elaborate on the apparatus used for these measurements in Sect 6.4 and report additional relevant information regarding background decoherence, back-action measurements, and the feedback scheme in Sections 6.5 6.6 and 6.7 re-

spectively.

6.2   Spin squeezing with real-time feedback

This section features two main results. First, following Fig. 6.1(a), we use the outcome of a collective, or joint, measurement to actively steer the collective spin-projection of an ensemble of 5×10^4 laser-cooled and trapped ^{87}Rb atoms to a target entangled quantum state. Real-time feedback allows generation of the target state with enhanced angular resolution $S^{-1} \equiv (\Delta\theta_{SQL}/\Delta\theta)^2 = 5.5(8)$, or 7.4(6) dB below the SQL, with no background subtractions. Second, we perform a direct subtraction of quantum noise without feedback and directly observe a conditionally enhanced phase resolution $S^{-1} = 59(8)$ or equivalently 17.7(6) dB below the SQL, along with [68], the largest phase estimation enhancement from entanglement to date in any system.

Entanglement is often created and manipulated via unitary interactions between qubits [136, 93, 113, 118, 102, 132, 62, 114, 28, 95]. However, the joint measurements on two or more qubits used here (sometimes referred to as quantum non-demolition measurements) have shown promise for creating entanglement, particularly among large numbers of qubits [88, 4, 140, 169, 96, 31, 19, 12, 142, 119, 133, 134]. By adding real-time feedback guided by the outcome of joint measurements, one can access a more diverse range of quantum technologies including Heisenberg-limited atomic sensors [26], reduction of mean field shifts in atom interferometers [47, 75], quantum teleportation [144, 86], and error correction [116, 165]. Quantum noise suppression with real-time feedback has been considered theoretically [155, 154] and demonstrated in a previous experiment [72] but without the critical enhancement in phase resolution that signifies entanglement.

We visualize a collection of N spin-1/2 atoms as a single collective Bloch vector $\mathbf{J} = J_x \hat{x} + J_y \hat{y} + J_z \hat{z}$ given by first order expectation values $J_\alpha \equiv \langle \hat{J}_\alpha \rangle$ of collective spin projection operators with $\alpha = \{x, y, z\}$. The quantum projection noise (QPN) and resulting SQL can be intuitively visualized by a quasi-probability distribution perpendicular to the classical Bloch vector (Fig. 6.1(a)). The distribution's rms fluctuations along a given spin-projection direction are given by $\Delta J_\alpha \equiv \sqrt{\langle \hat{J}_\alpha^2 \rangle - \langle \hat{J}_\alpha \rangle^2}$. In this chapter Δ will refer to the standard deviation of a given
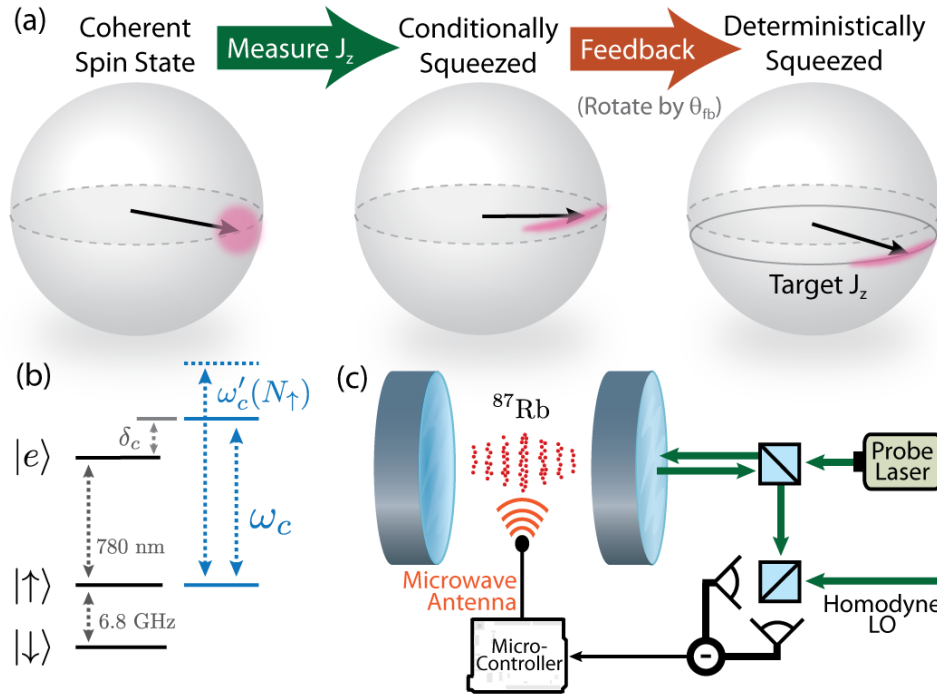
Figure 6.1: (a) A coherent spin state's spin-projection noise (pink distribution) is projected onto a squeezed state by a measurement of J_z. The quantum state randomly collapses within the original distribution, creating a conditionally squeezed state. The pre-measurement's outcome is then used to rotate the spin state's polar angle to a desired target spin projection (black solid line) $J_z = J_{ztar}$, creating a deterministically squeezed state. (b) The relevant ^{87}Rb energy levels (black) and cavity resonance frequency ω_c (blue). (c) Simplified experimental diagram. The cavity is probed in reflection. Homodyne detection of the probe is sampled by a microcontroller that then applies microwaves at 6.8 GHz to achieve the desired feedback rotation θ_{fb} to create the deterministically squeezed state in (a). See Section 6.4 for experimental details.

quantity. For a coherent spin state oriented at the equator of the Bloch sphere, the spin projection J_z and spin population $N_\downarrow$ both fluctuate from one trial to the next with a standard deviation $\Delta J_{z,QPN} = \Delta N_{\downarrow QPN} \equiv \sqrt{N}/2$.

We calculate the enhancement in phase resolution $S \equiv (\Delta\theta/\Delta\theta_{SQL})^2 = R/C^2$ [174], where $R \equiv (\Delta J_z/\Delta J_{z,QPN})^2$ is the observed spin projection noise relative to the projection noise level, and $C \equiv 2\langle|\hat{J}|\rangle/N$ is the fractional atomic coherence remaining (or "contrast") after a joint measurement. An additional 0.2 dB correction is applied to S for a 4% background loss of contrast (see Supplementary Material). Observing $S^{-1} > 1$ serves as a witness for entanglement between atoms [149] and the magnitude usefully quantifies the degree of entanglement [174, 79].

A joint measurement of the population of atoms $N_\uparrow$ is engineered by measuring the frequency shift of a TEM_{00} cavity mode. The cavity is tuned $\delta_c = 2\pi \times 400$ MHz to the blue of the ${}^{87}\text{Rb}$ $|\uparrow\rangle \equiv |5^2 S_{1/2}, F = 2, M_F = 2\rangle$ to $|e\rangle \equiv |5^2 P_{3/2}, F = 3, M_F = 3\rangle$ optical atomic transition as shown in Fig. 6.1(b). The second state forming the pseudo-spin system is $|\downarrow\rangle \equiv |5^2 S_{1/2}, F = 1, M_F = 1\rangle$. The cavity has finesse 2532(80) and power decay linewidth $\kappa = 2\pi \times 3.15(10)$ MHz. The atoms are laser-cooled to 10 μK and trapped tightly on axis in an intracavity 1D optical lattice (Fig. 6.1(c)). Spatially inhomogeneous coupling of atoms to the cavity mode is handled as in [31, 32, 19, 69]. Atoms in $|\uparrow\rangle$ strongly phase shift the intracavity probe light, causing the empty cavity resonance frequency ω_c to shift to ω_c'. A measurement of the shift $\omega_c' - \omega_c$ using homodyne detection of probe light reflected from the cavity can then be used to infer the population $N_\uparrow$. To measure the population $N_\downarrow$, a π-pulse microwave coupling can then be applied to swap the populations between $|\uparrow\rangle$ and $|\downarrow\rangle$, and a measurement of the new population in $|\uparrow\rangle$ can be made with the measurement outcome now labeled $N_\downarrow$.

The experimental sequence is shown in Fig. 6.2 (a) and (b). All atoms are prepared in $|\downarrow\rangle$, then a microwave $\pi/2$-pulse is applied to place each atom in an equal superposition of spin states, equivalent to preparing the Bloch vector along $\hat{y}$. We make a measurement of the spin projection J_z with measurement outcome labeled $J_{zp} = (N_{\uparrow p} - N_{\downarrow p})/2$. Each population measurement outcome $N_{\uparrow p}$ and $N_{\downarrow p}$ is obtained by averaging the cavity-probe signal over a 40 μs window. In each run

of the experiment, a microcontroller calculates J_{zp} and applies feedback to steer the state toward a targeted value of spin projection J_{ztar}. The feedback is accomplished by applying microwaves to rotate the Bloch vector through polar angle $\theta_{fb} \approx 2 \times (J_{ztar} - J_{zp})/(NC)$. After the feedback, a final measurement of the spin projection J_z is made with measurement outcome labeled $J_{zf} = (N_{\uparrow f} - N_{\downarrow f})/2$. Feedback toward $J_{zf} = 0$ is evident in the time trace (Fig. 6.2 (a)), since the final two cavity frequency measurement windows that provide $N_{\uparrow f}$ and $N_{\downarrow f}$ are more nearly equal than was the case for the two pre-measurement windows.

The microcontroller sets the sign of the rotation θ_{fb} by digitally toggling between two microwave sources that are $180°$ out of phase. The magnitude of the rotation $|\theta_{fb}|$ is controlled by varying the duration t_{fb} for which the microwaves are applied, with a discrete timing resolution of approximately 12 ns. The input technical noise floor, timing jitter, and timing resolution of the microcontroller are all sufficient to allow up to 20 dB of squeezing.

The outcomes J_{zp} and J_{zf} are plotted versus trial number and collated into histograms in Fig. 6.2(c). Projection noise for this data (independently confirmed by measuring the scaling of ΔJ_z with N) is $\Delta J_{z,QPN} = 218(10)$, consistent with the measured $\Delta J_{zp} = 235(24)$. The data on the right shows the final measurement outcomes J_{zf} after applying feedback for five different target states J_{ztar}. By implementing the feedback, each target state was reached with noise below the original projection noise.

To observe deterministic squeezing or phase resolution enhancement, the atomic coherence that remains after the pre-measurement and feedback must be evaluated. The contrast is determined in a separate set of experiments by using microwave rotations after the feedback step to rotate the Bloch vector to determine its total length. Accounting for the loss of coherence, we directly observe up to $S^{-1} = 5.5(8)$ (7.4(6) dB) of deterministic squeezing via pre-measurement and feedback.
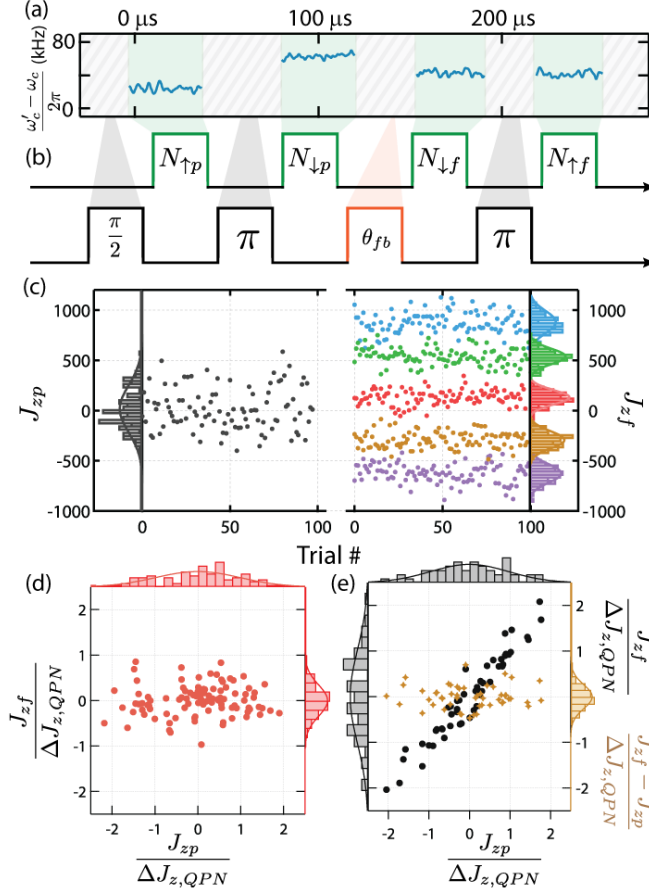
Figure 6.2: (a) Measured cavity resonance frequency for a single trial versus time, subtracting a constant 12 MHz frequency offset. (b) The time windows in which the probe is turned on (green) and the populations determined from each window. The fixed microwave rotations are shown in black with the feedback rotation shown in orange. (c) The pre-measurements J_{zp} (left) and final measurements J_{zf} (right) of J_z are plotted versus trial number and accumulated into histograms. Five different J_z states are targeted (five distinct colors on right) and reached with noise below QPN. The maximum deterministic squeezing is $S = -7.4(6)$ dB relative to the SQL. (d) Feedback reduces the noise distribution of the final measurement relative to the initial quantum noise in the pre-measurement. (e) If no feedback is applied the final and pre-measurement are strongly correlated (black), allowing for conditional squeezing (S = -10.3(6) dB) by using the differential quantity $J_{zf} - J_{zp}$ (gold). The increase in noise from feedback is discussed in the Supplementary Material.
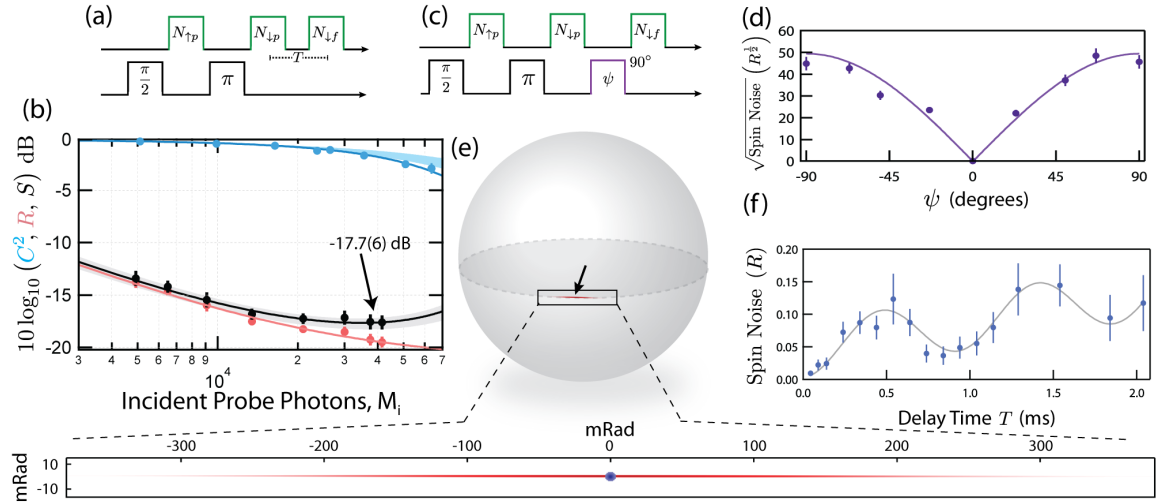
Figure 6.3: (a) Experimental sequence for conditional spin squeezing, with labeling mirroring that of Fig. 6.2a. (b) Squared contrast C^2 (blue), spin noise R (red), and spin squeezing S (black) are plotted versus the average number of incident photons M_i in a single measurement window. The solid lines are fits, the blue band is the predicted loss of contrast from free-space scattering, and the grey band indicates the total squeezing error bar. (c) The experimental sequence used to observe the back-action spin-projection. (d) The measured spin noise R is plotted versus ψ with fit (purple). (e) The reconstructed conditional probability distribution of the quantum state (red) on a Bloch sphere with Bloch (black) vector. The distribution is magnified with a 1:1 aspect ratio and plotted with the equivalent coherent spin state (blue) in the lower panel. (f) Thermal radial motion of the atoms causes the spin noise R to oscillate at twice the radial trap frequency as the time separation T between the pre- and final measurements is increased.

6.3   17.7 dB of conditional squeezing

For many applications, the feedback is not necessary. Instead of applying feedback, one can cancel the quantum noise by directly subtracting the pre-measurement J_{zp} from the final measurement J_{zf}, a technique known as conditional squeezing [88, 4, 140, 169, 96, 31, 19, 12, 142]. In Fig. 6.2(d) and (e), we compare conditional and deterministic spin noise reductions taken under identical settings. J_{zf} is plotted versus J_{zp} and the results are collated into histograms on each axis. With feedback (red), J_{zf} is driven to zero with resolution below $\Delta J_{z,QPN}$, regardless of J_{zp}. Without feedback (black), J_{zp} and J_{zf} are correlated, and the quantum noise can be conditionally subtracted from the final measurement by taking the difference $J_{zf} - J_{zp}$ (gold).

The deterministic squeezing with feedback is primarily limited by errors in the π-pulses due to microwave amplitude and frequency noise. However, by increasing the number of atoms to $N = 4 \times 10^5$, we improve the amount of conditional spin squeezing to $S^{-1} = 59(8)$ or 17.7(6) dB. The experimental measurement sequence is the same, but to avoid added noise from the π-pulses, we only consider the reduction in the noise of the difference of two population measurements of the same spin state $R = (\Delta(N_{\downarrow f} - N_{\downarrow p}))/\Delta N_{\downarrow QPN})^2$ (Fig. 6.3(a)). The information gained from the first measurement $N_{\uparrow p}$ is not used here, but its presence serves to spin-echo away probe-induced inhomogeneous light shifts at the end of the pre-measurement pair $N_{\uparrow p}$ and $N_{\downarrow p}$. Because the Bloch vector lies at the equator, small angular displacements of the polar angle could be sensed from changes in a single spin state's population alone.

In Fig. 6.3(b), we show the noise reduction R versus the average number of photons M_i incident upon the cavity during a single probe measurement window. Again, this is the directly observed noise reduction with no background subtractions or removal of noise of the final mea-surement applied. The maximum quantum noise reduction is $R^{-1} = 92(9)$, or 19.6(4) dB below QPN and is limited by both a technical noise floor 25 dB below QPN and optomechanical effects induced by the probe light being turned on and off, an effect that increases with M_i. Also apparent in Fig. 6.3(b), the atomic coherence or contrast (blue) after the pre-measurement decreases with

increasing M_i due primarily to undesired free space scattering causing collapse of individual atoms' wave functions into spin up (blue prediction band). The background contrast C_{BG} is obtained from a measurement with $M_i = 0$ in the two pre-measurement windows. The black data and fit in Fig. 6.3(b) display the squeezing obtained by combining the reduction in noise with the reduction in contrast.

We also examine the back-action or anti-squeezed spin-projection. The experimental sequence is shown in Fig. 6.3(c) and is distinguished by the replacement of the rotation θ_{fb} with a microwave rotation about an axis parallel to the Bloch vector through a fixed angle ψ. Figure 6.3(d) shows the increase in spin noise R moving from the 17 dB squeezed (at $\psi = 0$) to anti-squeezed (at $\psi = \pm 90°$) projections. Using an inverse Radon transform, we construct a visualization of the equivalent squeezed state, shown in Fig. 6.3(e). The original coherent state noise is shown in blue. The state has $\Delta J_z \Delta J_x / (\Delta J_{z,QPN})^2 = 6.1 > 1$ and is no longer a minimum uncertainty state owing to finite quantum efficiency for detecting the probe light. From the increase in area and its scaling with M_i we can infer the quantum efficiency of a joint measurement of a single population is $\tilde{Q}_1 = 38(14)\%$, in good agreement with an independent prediction of $37(5)\%$ from measuring path efficiencies, cavity loss, detector efficiencies, technical noise floors, and laser turn-on times (see Sect. 6.4). Here, the total quantum efficiency of the full measurement sequence $(N_{\uparrow p}, N_{\downarrow p}, N_{\downarrow f})$ is effectively 4 times lower than $\tilde{Q}_1$ due to the additional noise in the final measurement $N_{\downarrow f}$ and the presently unused pre-measurement $N_{\uparrow p}$.

In Fig. 6.3(f), we evaluate how well the conditional noise reduction can be maintained over a variable evolution time T. This is an important consideration for implementing conditional squeezing in atomic sensors. The contribution to R from technical noise sources is partially removed by performing the measurement sequence of Fig. 6.3(a) with no atoms present and subtracting the measured noise variance from the noise variances obtained with atoms present. The spin noise R is seen to oscillate at twice the radial frequency of the trapping potential due to thermal radial atomic motion that causes an oscillation in each atom's coupling to the cavity mode. The additional monotonic increase in R is not currently understood. A 3D optical lattice or a smaller atomic

temperature to lattice depth ratio can be used to reduce the noise oscillations in the future.

The improved squeezing relative to previous work [19, 41] was achieved by increasing the net quantum efficiency for probe detection from 5% to 37% (by constructing a single-ended cavity, reducing losses on cavity mirrors, and using homodyne detection), increasing the cavity finesse by 3.5, and implementing a two-probe laser technique that reduced the relative frequency noise between the probe laser and the empty cavity from 16 to 25 dB relative to projection noise [38]. See Sect. 6.4.

It is physically reasonable to expect that the majority of the atoms participate in a single multipartite entangled state. The entanglement depth, or we believe more appropriately "entanglement breadth" ζ quantifies the *minimum* number of atoms that *provably* particpate in a multipartite entangled state, no matter how weakly [150, 107]. We find the largest breadth $\zeta = 400(120)$ atoms at squeezing S^{-1}=15 dB, but at the largest squeezing we find ζ=170(30) atoms.

Applying real-time feedback based on the outcome of joint measurements may allow for new applications in both quantum information technology and precision measurement. For instance, the utility of highly spin-squeezed states suffers from the fact that the state lives on a sphere, causing the back-action spin projection to couple into the measured spin projection J_z if the state is rotated too far from the equator. In clock applications, this results in needing to reduce the Ramsey phase evolution time such that the net enhancement in clock precision is far from approaching the Heisenberg limit [3]. It was recently proposed that joint measurement and feedback similar to that used here would allow one to actively measure and steer the back-action noise out of the measured spin projection and would thus allow enhancements in precision approaching the Heisenberg limit [26]. With improved atom-cavity coupling (e.g higher finesse, smaller mode waist size), even greater amounts of squeezing than that reported here can be achieved in principle [32]. However, it will be critical to consider current limiting effects such as optomechanical ringing and time-varying couplings between measurements due to atomic motion in order to achieve significant improvements. Having now shown that large enhancements in phase resolution using entanglement are achievable in real systems that are compatible with state-of-the-art precison measurements,

next steps may include application to matterwave interferometers [47] and optical lattice clocks [119].

6.4   Experimental details

Several technological improvements from previous experiments were key to achieving the results of this chapter. Full experimental diagrams of the optics and electronics are shown in Fig. 6.5 and Fig. 6.6 respectively in an attempt to highlight differences from previous work, and a general procedure is described.

6.4.1   Atomic state preparation

The atoms are loaded from a magneto-optical trap (MOT) whose loading time sets the experimental repetition rate of 1 second. Polarization gradient cooling is then used to cool the atoms to 10 μK and to load them into 823 nm optical lattice sites spanning approximately 1 mm along the cavity axis. A bias magnetic field along the cavity axis of 1.1 Gauss sets the quantization axis. Optical pumping beams are used to polarize the atoms with $> 90\%$ probability into the $|\downarrow\rangle = |5^2S_{1/2}, F = 1, M_F = 1\rangle$ ground state. After optical pumping, the MOT beams are applied once more to clear any remaining atoms from the $F = 2$ manifold. Atoms not in $|\downarrow\rangle$ are not rotated by the microwaves into the measured $|\uparrow\rangle$ state due to the Zeeman splitting between states. As a result, they do not contribute to the experiment. Lastly, to account for inhomogeneous coupling of the atomic ensemble to the probe mode, the reported atom numbers $N_\uparrow$, coupling g, and cooperativity parameter $\mathcal{C}$, in both the main text and here, are effective values as described in Refs. [31, 32, 19, 69]. Neglecting small corrections for radial inhomogeneity, the total atom number $N_{\uparrow,tot}$ in the lattice in state $|\uparrow\rangle$, the single-atom Rabi frequency $2g_0$ at an antinode of the probe mode, and the cooperativity parameter C_0 at an antinode of the probe mode are related to the effective quantities by $N_\uparrow \approx \frac{2}{3}N_{\uparrow,tot}$, $g^2 \approx \frac{3}{4}g_0^2$, and $\mathcal{C} \approx \frac{3}{4}C_0$, respectively.

6.4.2 Science cavity and lattice

The optical cavity parameters are given in Table 6.1. Compared to previous work [19, 31], the cavity finesse has been increased by a factor of 3.5, or equivalently the cavity power decay linewidth κ is smaller by the same factor. The cavity is now primarily transmissive at a single end, *i.e.* the input mirror's transmission coupling rate κ_1 is much greater than the output mirror's transmission coupling rate κ_2. As a result, measurement of the probe light in reflection from the cavity captures nearly all of the information transmitted out of the cavity mode, with effective quantum efficiency now of $\kappa_1/\kappa = 0.83(3)$ compared to the previous effective quantum efficiency of 0.23 in reflection alone. This eliminates the need for a second detection system for the transmitted cavity light.

The cavity's frequency is actively stabilized to the frequency of the 823 nm optical lattice laser. This is achieved by a Pound-Drever-Hall (PDH) frequency servo that feeds back to piezos to control the cavity length. The bandwidth of the servo is about 1.5 kHz. The lattice laser is frequency stabilized to an independent transfer cavity using PDH detection with servo bandwidth of 1 MHz. The lattice laser's frequency is tuned relative to the transfer cavity by using a high frequency phase modulator to place 5 to 8 GHz sidebands on the lattice laser light probing the cavity. The optical frequency of a first order sideband is locked to the transfer cavity, such that tuning the modulation frequency then allows the lattice laser's frequency to be tuned continuously over several GHz. The microwave voltage-controlled oscillator (VCO) that provides the modulation is phase-locked to a DDS that is controlled by the data acquisition computer for ease of tuning. Finally, the frequency of the transfer cavity is stabilized with 1.5 kHz bandwidth by PDH probing of another longitudinal mode using a 795 nm laser that is stabilized using Doppler-free FM spectroscopy to the D1 transition in ^{87}Rb. 795 nm light is used simply for historical reasons.

6.4.3 Relative frequency noise between cavity and probe

Relative frequency noise between the atomic probe laser (200 kHz FWHM nominal linewidth ECDL laser) and the empty cavity hinders our ability to determine the atomic-induced shift $\omega_c' - \omega_c$
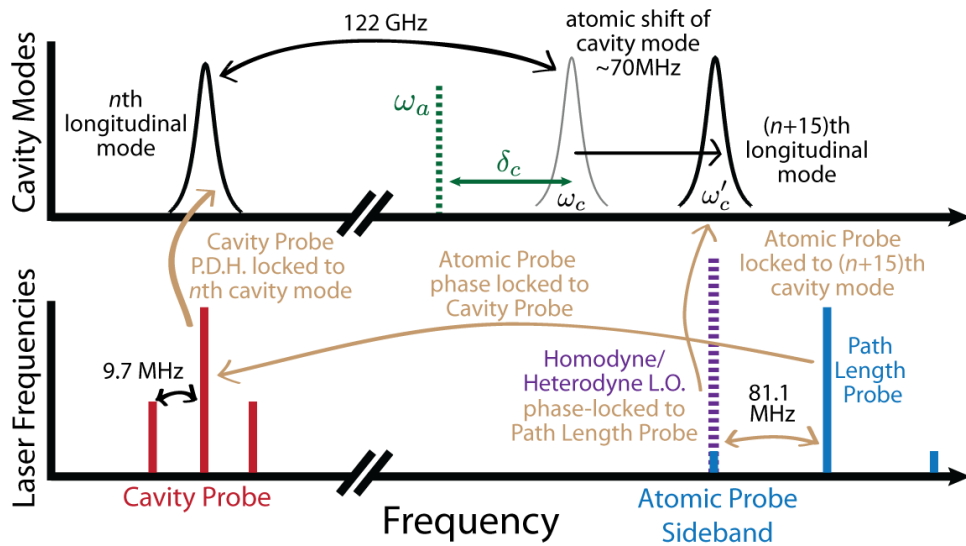
Figure 6.4: Experimental frequency diagram. Relevant frequencies described in the text are shown along with the locking scheme of the atomic (blue) and cavity (red) probe lasers. The two longitudinal resonances of the cavity that these two lasers probe are separated by 122 GHz and shown on the upper graph. The unshifted $n+15$th cavity mode at ω_c is detuned δ_c blue from the atomic resonance ω_a. The presence of atoms in $|\uparrow\rangle$ typically shift this cavity mode by approximately 70 MHz, to ω'_c. The homodyne local oscillator beam is shown in purple (dashed), and feedback stabilization steps are shown as gold arrows with descriptions.

Cavity Parameters (probe $\lambda = 780$ nm)

Single-atom cooperativity $\mathcal{C} = \frac{4g^2}{\kappa\Gamma}$	0.044(6)
Single-atom vacuum Rabi splitting g	$2\pi \times 0.44(3)$ MHz
Input coupling κ_1	$2\pi \times 2.60(5)$ MHz
Output coupling κ_2	$2\pi \times 0.17(1)$ MHz
Internal losses κ_L	$2\pi \times 0.38(8)$ MHz
Linewidth κ	$2\pi \times 3.15(10)$ MHz
Dressed-cavity linewidth* κ'	$2\pi \times 3.6(1)$ MHz
Dressed-cavity linewidth† κ'	$2\pi \times 3.2(1)$ MHz
Q.E. due to internal losses κ_1/κ	0.83(3)
Finesse	2532(80)
Free spectral range	8.105(5) GHz
Frequency difference TEM_{00}-TEM_{10}	2.290(5) GHz
TEM_{00} waist size w_0	70(1) μm
Cavity length	1.849(1) cm
Mirror radius of curvature	4.999(5) cm

Cavity Parameters (lattice $\lambda = 823$ nm)

Input coupling κ_1	$2\pi \times 4.40(10)$ MHz
Output coupling κ_2	$2\pi \times 0.23(1)$ MHz
Linewidth	$2\pi \times 5.8(6)$ MHz
Finesse	1400(150)
Trap depth	115 μK
Circulating power P_{circ}	0.30(3) W
Power Buildup (P_{circ}/P_{inc})	800(130)
Axial trap frequency	181(20) kHz
Radial trap frequency	900(50) Hz
TEM_{00} waist size w_0	71(1) μm

Table 6.1: Relevant cavity parameters at the atomic and cavity probe laser wavelength $\lambda = 780$ nm and at the lattice laser wavelength $\lambda = 823$ nm. The symmetric, standing wave cavity's mirror transmission coefficients, T_1 on the probed end (1) and T_2 on the closed end (2), are expressed in terms of coupling rates $\kappa_{1,2} = T_{1,2} \times$ (free spectral range). The atomic decay linewidth of $|e\rangle$ is $\Gamma = 2\pi \times 6.07$ MHz. The dressed cavity linewidths κ' include broadening of the cavity resonance at ω_c' due to spontaneous scattering from the atoms.
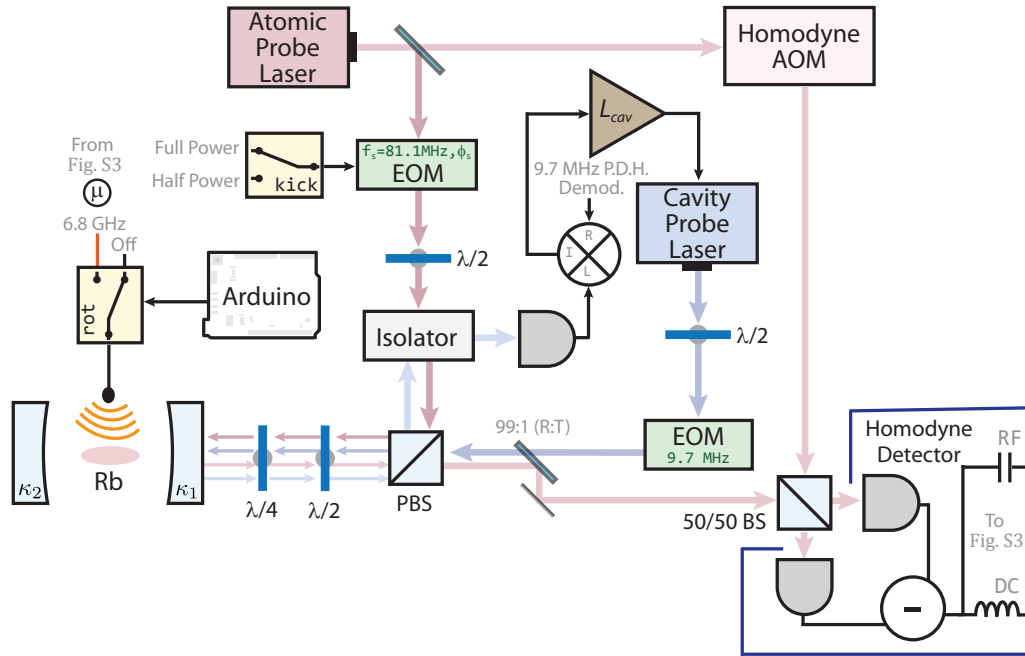
Figure 6.5: Optical block diagram. The resonance frequency of the optical cavity ω_c' is detected using homodyne detection of the atomic probe laser (red). Homodyne detection is performed on an $f_s = 81.1$ MHz sideband on the atomic probe laser. This sideband can be applied at half power by the "kick" switch to provide an extra impulsive kick to the atoms in order to cancel optomechanical ringing (described in Section 6.4.5.5). The carrier of the atomic probe laser is detected in heterodyne (RF port) to provide a path length reference (see Fig. 6.6) for stabilizing the homodyne detection phase. The cavity probe laser (blue) is P.D.H. locked, via the L_{cav} loop filter, to another longitudinal mode of the optical cavity, unshifted by atoms, and provides stabilization of the atomic probe laser's frequency to the cavity frequency. The atomic probe and cavity probe are separated optically via polarization. Real-time feedback is applied using an Arduino microcontroller that controls the sign and duration of 6.8 GHz μ-wave pulses. More details are given in Fig. 6.6.
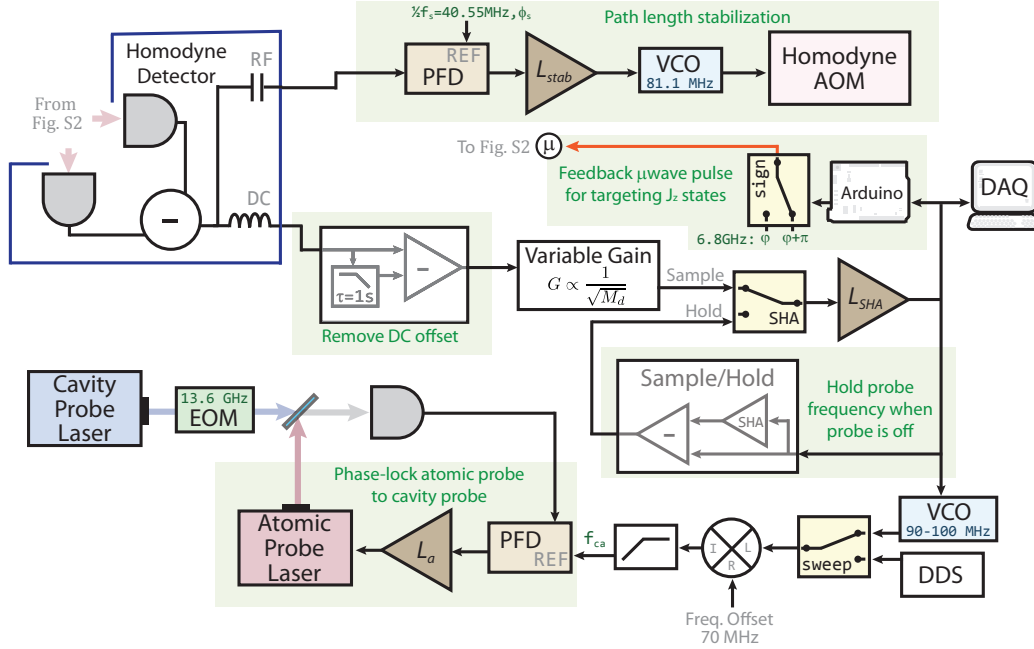
Figure 6.6: Electronic block diagram. The homodyne detection phase is stabilized by detecting the carrier of the atomic probe beam with the signal appearing at 81.1 MHz at the `RF` port. The phase of this signal is locked to a DDS frequency reference by applying feedback through the L_{stab} loop filter to a VCO controlling the homodyne AOM. The homodyne difference signal (`DIFF`) is used to stabilize the atomic probe laser to the atom-shifted cavity mode at ω_c'. The signal is high-pass filtered at 1 Hz to remove slowly drifting DC offsets and then passed through a variable gain amplifier (used to maintain constant loop gain as M_i is varied) before entering the loop filter L_{SHA}. The output of L_{SHA} is used to control a VCO which provides a phase reference to a phase lock between the atomic probe laser and the cavity probe laser using loop filter L_a. The cavity frequency ω_c' is detected by sampling the output of L_{SHA}. When the atomic probe is off, a sample and hold circuit is used to hold the output of the loop filter. A separate synthesizer (DDS) can be used to perform sweeps of the atomic probe. Real-time feedback is applied by the Arduino based on the sampled output of L_{SHA}. The Arduino can control the sign of the feedback by switching (`sign`) between two 6.8 GHz sources that are 180° out of phase.

and hence the atomic populations that constitute our joint measurement of spin projection J_z. To remove this, an improved stabilization scheme of the atomic probe laser has been implemented similar to that described in [38], described below and shown in Fig. 6.4.

A second 200 kHz FWHM laser at 780 nm, called the cavity probe laser, is PDH locked with servo bandwidth 800 kHz to a longitudinal mode of the science cavity that is 122 GHz (15 free spectral ranges) away from resonance with the atomic transition $|\uparrow\rangle$ to $|e\rangle$. The large detuning means that even at much higher circulating powers inside the cavity, the cavity probe produces sufficiently small atomic dephasing and spontaneous emission. Frequency noise on the science cavity is thereby imposed on the cavity probe laser for spectral noise at frequencies below the unity gain frequency of the servo. Conversely, the original frequency noise of the cavity probe laser is also reduced relative to that of the empty cavity.

The cavity probe light is circularly polarized σ^-, opposite to that of the primary or atomic probe which is σ^+ polarized. This allows the reflected cavity probe light to be polarization separated from the atomic probe after probing the cavity. An avalanche photodiode (Hamamatsu S2381, gain ≈ 150) is used to detect the PDH signal generated by typically 50 nW of total optical probe power. To maximize the signal-to-noise for a given amount of circulating cavity probe power in the cavity, the PDH signal is derived by phase modulating the cavity probe light at frequency 9.7 MHz $\gg (\kappa/2)/2\pi$ so that the phase modulation sidebands do not enter the cavity.

To link the cavity probe laser to the atomic probe laser, approximately 2 mW of the cavity probe laser's light is phase modulated at $f_m = 13.6$ GHz. The modulation frequency is derived from a low-phase noise microwave source [34]. The atomic probe laser is then phase-locked to a 9th order sideband at a total offset of $9 \times f_m = 122.4$ GHz from the cavity probe frequency using loop filter L_{cav}. The heterodyne signal between the sideband and the atomic probe appears in the rf spectrum at 500 to 700 MHz. This heterodyne beat note is phase-locked to an rf voltage-controlled oscillator (VCO) with center frequency f_{ca}, and with servo bandwidth of 2 MHz. By tuning the VCO frequency f_{ca}, we can thereby tune the atomic probe laser relative to the cavity, while frequency noise on the atomic probe is now common-mode with the cavity.

A representative power spectral density of instantaneous frequency noise between the atomic probe laser and the cavity, $S_\nu(f)$ is shown in Fig. 6.7a. This data was taken using a heterodyne detection setup which existed before implementing the final homodyne detection scheme described in this chapter [38]. However, for this data, the power in the atomic probe laser beam was turned up so that technical noise due to laser freqeuency fluctionations dominated the fundamental photon shot noise and any technican noise associated with the detection scheme. The data in Fig. 6.7 faithfully characterizes the quality of frequency stabilization between the atomic probe and the optical cavity for all of the generation three spin squeezing experiments.

In the central flat region of Fig. 6.7(a), $S_\nu \approx 1.5 \times 10^3$ Hz^2/Hz. This corresponds to the instantaneous frequency noise of a laser with Lorentzian FWHM $\Delta\nu = \pi \times S_\nu = 5$ kHz, significantly smaller than the initial laser linewidth of 200 kHz.

The roll off at high frequency results from 300 kHz anti-aliasing low pass filters after the IQ demodulation. The rise at low frequencies is largely due to uncontrolled relative path length changes between the atomic-probe LO and atomic-probe paths. We have found it unnecessary to stabilize this path length phase for the preliminary results presented here because it only required 200 μs to measure the differential quantity $f_{cf} - f_{cp}$.

We are interested in characterizing the noise in the difference between the final and premesaurement. Each measurement is the average of the measured frequency in a window of length $T_{\rm win}$ and the two measurement windows have a time gap $T_{\rm diff}$ between them. The variance is obtained by integrating $(\Delta f_d)^2 = \int_0^\infty S_\nu(f) \, T(f) \, df$. The transfer function is $T(f) = 4 \sin^2(\pi f (T_{\rm win} + T_{\rm diff})) \sin^2(\pi f T_{\rm win})/(\pi f T_{\rm win})^2$. Figure 6.7b shows the measured noise variance Δf_d as a function of the measurement window length $T_{\rm win}$ with $t = 0$ μs. For this data, the minimum is $\Delta f_d = 6$ kHz at $T_{\rm win} = 100$ μs.

6.4.4 Decoherence from the cavity probe

The measurements of Fig. 6.7 were made at very high probe powers with no atoms in the cavity. As a result, the photon shot noise and technical noise sources of the detectors were negligible
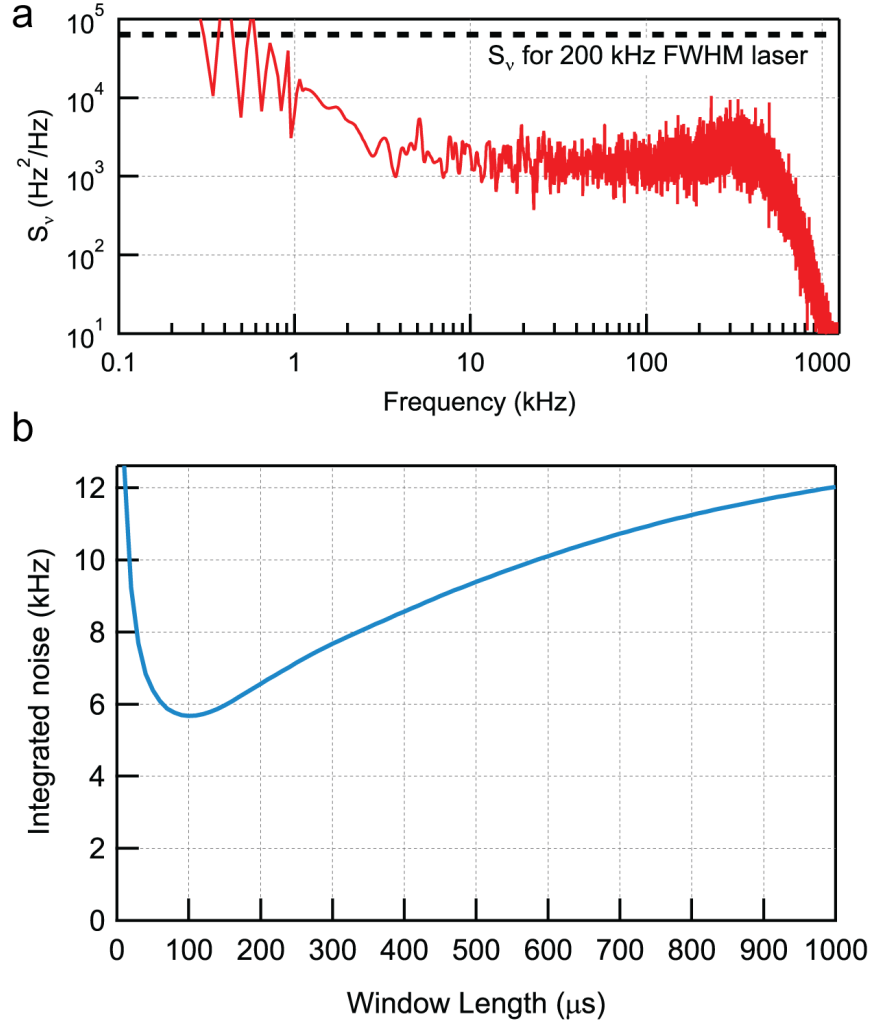
Figure 6.7: (a) The measured power spectral density of instantaneous frequency fluctuations $S_\nu(f)$ between the atomic-probe and an empty cavity mode. The frequency stabilization described in the text reduces the noise by close to a factor of 50 over a broad range relative to the S_ν one expects for the linewidth of our free-running 200 kHz FWHM external cavity diode lasers. For this data, the atomic and cavity-probes were set to a high enough power that increasing either did not decrease $S_\nu(f)$, so that we are sensitive only to technical noise floors. Also, heterodyne path-length stabilization had not yet been implemented, and this is largely responsible for the rise below 2 kHz. (b) The integrated noise in the difference of two frequency measurement windows, plotted as a function of window length T_m, with a fixed $t = 0$ μs window separation.

compared to contributions from other technical noise sources. However, as the power in the cavity-probe is increased, the amount of squeezing may become limited by additional scattering of light from the atoms, potentially leading to single-particle wavefunction collapse (loss of signal) and Raman transitions to other ground hyperfine states (a source of additional noise.) Inhomogeneous differential light shifts of the spin transition frequency can also lead to dephasing that can be spin-echoed away, but perhaps imperfectly.

Figure 6.8a shows the noise variance $(\Delta f_d)^2$ between two measurements of the cavity resonance frequency versus the cavity-probe power incident on the cavity P_c. Here the atomic-probe power is increased such that its photon shot noise contribution is negligible. The right hand axis translates the noise variance into an equivalent uncertainty relative to a quantum projection noise level $\Delta f_{PJN} = 97$ kHz. For powers above 1 μW, the technical noise floor saturates to 27 dB below the projection noise level. For lower powers, the noise variance scales as $(\Delta f_d)^2 \propto 1/P_c^2$, indicating that lower powers P_c might be utilized with improved photodetection.

The cavity-probe induces a differential light shift of the transition frequency ω_{hf} between down and up. We measure the differential shift of the clock transition frequency $|F = 1, m_F = 0\rangle$ to $|F = 2, m_F = 0\rangle$ versus P_c in Fig. 6.8b. Appropriately rescaling for transition strengths and detunings gives an average shift of $\omega_{\uparrow\downarrow}$ by 8.5 kHz per μW. The shift is highly inhomogeneous and leads to dephasing. However, spin-echo measurements have shown that the atomic contrast (*i.e.*, length of the Bloch vector) is negligibly affected at $P_c = 0.5$ μW with 40 μs measurement windows. Thus, the atomic state is not significantly decohered by the cavity stabilization presented here.

6.4.5   Atomic probe

The atomic probe is used to determine the shifted cavity mode frequency $\omega_c' - \omega_c$. The cavity probe is σ^+ polarized to take full advantage of the cycling transition for strong light-atom coupling as well as to avoid Raman transitions to other ground states caused by spontaneous emission [32]. The circular polarization also facilitates easy separation of the cavity probe light reflected from the cavity for sending to a homodyne detector.
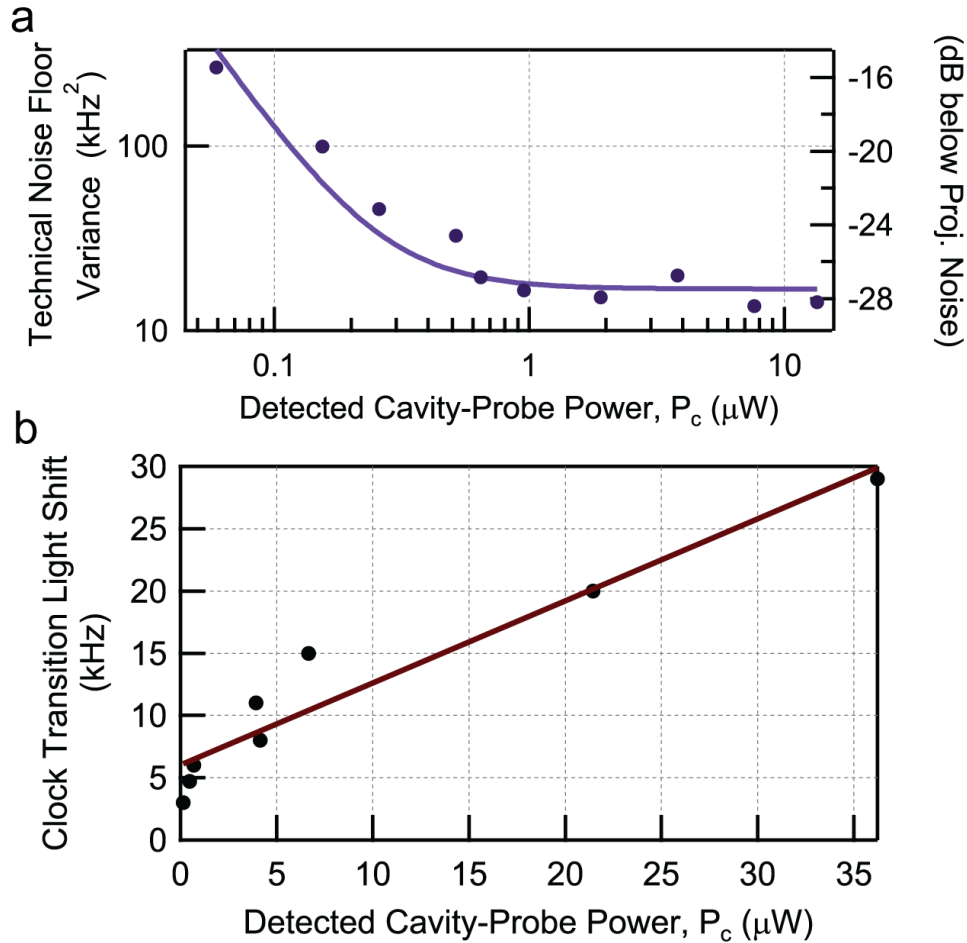
Figure 6.8: (a) The 2-window noise variance $(\Delta f_d)^2$ is plotted versus the detected power of the cavity-probe beam for $T_m = 40$ μs and $t = 0$. Above 1 μW, the noise variance saturates to 27 dB below the quantum projection noise level. (b) The measured light shift of the ^{87}Rb clock transition is plotted versus the detected power of the cavity-probe beam. The shift is approximately 660 Hz per μW. The non-zero light shift at $P_c = 0$ is due to an additional constant light shift from the 823 nm optical lattice. Due to differing Clebsch-Gordan coefficients, the shift of the $|\downarrow\rangle$ to $|\uparrow\rangle$ transition frequency $\omega_{\uparrow\downarrow}$ is approximately 13 times larger, but still causes very little coherence loss for the preliminary squeezing results presented here.

Near resonance, the reflected q_r quadrature response of the field is directly related to the incident field $i_i \propto \sqrt{M_i}$ and the detuning δ_p between the probe light and the cavity resonance by [32]:

$$\frac{q_r}{i_i} = \frac{4\delta_p}{\kappa} \left(\frac{\kappa_1}{\kappa}\right) \left(\frac{(\kappa/\kappa')^2}{1 + \left(\frac{\sqrt{N_\uparrow}2g}{2\delta_c'}\right)^2}\right) \tag{6.1}$$

where $\delta_c' = \omega_c' - \omega_a$; ω_a is the optical atomic transition frequency, and the dressed cavity linewidth is $\kappa' = (\kappa + \Gamma \left(\sqrt{N_\uparrow}g/\delta_c'\right)^2)/(1 + \left(\sqrt{N_\uparrow}g/\delta_c'\right)^2)$. Homodyne measurements of q_r allow us to determine the detuning of the probe from ω_c'.

6.4.5.1   Homodyne phase stabilization

Homodyne detection requires stabilization of the relative path length between the homodyne reference path and the probe path, as well as removing other sources of relative phase noise. To achieve this, the homodyne reference light derived from the same laser is shifted up in frequency by an acousto-optic modulator (AOM) driven by a VCO with nominal frequency $f_h = 81.1$ MHz. The atomic probe light is weakly phase modulated at fixed frequency $f_s = 81.1$ MHz. The lower sideband is tuned close to resonance with ω_c' while the much stronger carrier component is 81.1 MHz off resonance from the cavity. The strong carrier component primarily reflects off of the cavity without creating any additional light circulating inside of the cavity–important for avoiding dephasing and spontaneous emission from this frequency component.

The carrier component acts as a phase reference for stabilizing the homodyne detection phase, and it appears on the homodyne detector as a signal at f_s. The signal is separately amplified from the DC signal by AC coupling the homodyne detector's signal to a high frequency transimpedance amplifier AD8015 (`RF` port). The `RF` port of the homodyne detector is sensitive to frequencies above 5 MHz while the DC difference and sum ports (not shown) of the detector have a bandwidth 1.5 MHz. The two detector ports are balanced well enough that $\frac{P_{DIFF}}{P_{SUM}} < 7 \times 10^{-3}$, where P_{DIFF} and P_{SUM} are the difference and sum of the two powers detected on the two photodiodes comprising the

homodyne detector. An additional electronic relative gain adjustment between the two photodiodes allows cancellation of power noise on the homodyne reference by typically $< 3 \times 10^{-4}$.

The carrier/homodyne reference beat note is then phase-locked to a stable DDS reference frequency at f_s. The phase of this reference frequency ϕ_s sets the quadrature of detection in homodyne and is under the control of the data acquisition computer. The phase lock is implemented with 50 kHz bandwidth and is achieved by feedback to the VCO that drives the homodyne frequency shifting AOM at f_h. This feedback loop works to continuously readjust the homodyne reference's phase to compensate for relative path length noise and other relative phase noise so that the q quadrature of the light reflected from the cavity appears at the difference port of the homodyne detector. The rms noise in this phase lock is low enough to resolve the cavity frequency with precision at least 28 dB below quantum projection noise.

6.4.5.2 Locking of atomic probe to cavity

We actively feedback to lock the atomic probe's sideband to ω_c'. This improves the dynamic range of the detection system, removes sensitivity to scale-factor noise, creates more consistent optomechanical effects, and removes nonlinearities associated with the dispersive error signal. The error signal is the detected q quadrature of the atomic probe's lower sideband as measured in homodyne at the difference port. The signal is a dispersive feature with a zero crossing appearing as the atomic probe laser's frequency is swept through resonance with ω_c (or ω_c') [32] .

During each measurement window of ω_c' the atomic probe's lower sideband is turned on for approximately 40 μs, and the DC homodyne signal is used to actively lock the sideband's frequency to ω_c'. This is achieved by feedback to the VCO that provides the frequency reference f_{ca} to which the cavity/atomic probe beat note is phase-locked. The phase-locking is achieved by adjusting the atomic probe laser's frequency via the loop filter L_{SHA}. The characteristic settling time of the servo is 1 μs for a unity gain frequency of 160 kHz. In order to record ω_c', the output of the L_{SHA} loop filter that sets the VCO control voltage is directly sampled at 2.5 MHz by the data acquisition computer (DAQ).

Since the atomic probe lower sideband is turned off between measurements, the atomic probe laser's frequency must be held fixed using the sample-and-hold circuit as shown in Fig. 6.6. When the atomic probe sideband is turned on, the circuit samples the loop filter voltage provided to the VCO that provides f_{ca}. When the sideband is turned off, the circuit holds the output voltage of the loop filter so that f_{ca} is held at its previous value.

Trial-to-trial fluctuations in atom number are significantly larger than fluctuations due to projection noise. This increases the range over which the probe laser must slew its frequency to align the lower sideband with ω'_c during the first $N_{\uparrow p}$ premeasurement. To reduce this initial offset, a "pre-centering" measurement is performed 1.5 ms before each experimental squeezing trial: a $\pi/2$ microwave pulse rotates the atoms to a superposition of $|\uparrow\rangle$ and $|\downarrow\rangle$ and the lower sideband is centered by the feedback loop at ω'_c. The atomic probe frequency is then held, and the probe light is switched off. The atoms are then optically pumped back to $|\downarrow\rangle$ for the actual spin squeezing measurements described in the main text.

We often wish to scan the power in the atomic probe lower sideband (quantified by the number of incident probe photons in a single measurement window M_i) to look at variation in measurement noise. This is accomplished by changing the rf power supplied to the EOM at f_s to modify the phase modulation index. For reference, a typical sideband/carrier ratio for $M_i = 36500$ incident photons is 0.004. Thus, the carrier power and hence the open loop gain of the path length phase stabilization for homodyne detection is relatively unaffected as we vary M_i.

In contrast, the open loop amplitude gain of the lower sideband to cavity lock scales as $\sqrt{M_i}$. To compensate, a variable gain amplifier (VGA; Analog Devices AD8337) is inserted after the homodyne detector. When the data acquisition computer changes the rf power that sets M_i, it also simultaneously scales the VGA's gain to keep the net loop gain fixed. DC offsets in the homodyne difference port are problematic when the gain is scaled and are therefore removed using a low pass filter ($\tau = 1$ s) and differential amplifier that essentially make a low bandwidth measurement of the DC offset that is then subtracted from the fast 40 μs measurement windows.

With this approach, we achieve a very large dynamic range from $M_i = 150$ to $M_i = 3 \times 10^5$.

When $M_i \lesssim 100$ in a 40 μs window, the average number of detected photons within the servo's time scale of 1 μs approaches unity. The photon shot-noise then imposes rms fluctuations on the atomic probe's frequency that are comparable to the cavity half-linewidth, leading to a reduction in fundamental signal to noise for estimating ω_c'.

Lastly, for diagnostic reasons, it is often useful to do broad sweeps of the lower sideband's frequency across the cavity resonance frequency. To accomplish this, the atomic probe laser's beat note with the cavity probe laser can be phase-locked to a direct digital synthesizer (DDS) source that provides the reference frequency f_{ca} in place of the usual VCO. The DDS frequency can be phase-coherently swept at programmable rate and range, accomplishing the desired sweep of the atomic probe frequency.

6.4.5.3 Calibration of incident photon number M_i

The number of incident photons on the cavity M_i is determined from the homodyne signal and measured quantum efficiencies. The locking scheme used for homodyne detection allows precise control of the relative phase between the homodyne reference beam and the atomic probe sideband by tuning the phase ϕ_s. Experimentally, when the atomic probe sideband is off resonance from the cavity and one scans ϕ_s over 2π, a sinusoidal interference fringe is observed in the homodyne difference port. The size of this fringe and the independently measured total power in the homodyne reference beam (130 μW typical) are used to determine the rate R_i of incident photons in the atomic probe lower sideband, coupled to the cavity, that would have been required to produce the observed fringe. The number of incident photons is $M_i = R_i \times 40$ μs.

Physically, this means M_i can be understood as the average number of photons in the atomic probe lower sideband crossing an imaginary plane directly in front of the cavity input mirror, counting only those that are spatially mode matched to the cavity TEM$_{00}$ mode, and integrated into a 40 μs window. The uncertainty in the absolute calibration M_i is approximately 25% due to uncertainty in the spatial mode-matching of the incident atomic probe beam and the homodyne reference beam. This uncertainty leads to uncertainty in the prediction of contrast lost in Fig.

3(b) of the main text, but does not lead to any uncertainty in the amount of squeezing or the experimental quantum efficiency $Q_1^{(0)}$ to be discussed in Section 6.4.5.4.

6.4.5.4   Quantum efficiency

To determine the probe detuning δ_p, we estimate the ratio q_r/i_i from the detected fields q_d/i_d. Vacuum or photon shot noise that appears in the detection of the q_d quadrature limits the resolution on our ability to determine ω_c'. We express the noise in the ratio as

$$\frac{(\Delta q_d)^2}{i_d^2} = \frac{1}{4M_i Q_1^{(0)}} + (\Delta q)^2, \tag{6.2}$$

where the one-window quantum efficiency $Q_1^{(0)}$ includes fundamental losses of signal to noise resulting from both photon losses and technical noise floors shown in Table 6.2.

The additional term $(\Delta q)^2 = f + rM_i^n$ represents noise contributions from the technical noise floor f associated with residual frequency noise on the atomic probe laser relative to the cavity mode frequency, and noise from optomechanical ringing r, which we model with an arbitrary nth-order polynomial scaling with $n \neq -1$. These noise sources have different scalings with M_i than the fundamental quantum noise (first term).

We define a new effective quantum efficiency Q_1 which includes the effects of the technical noise floor and optomechanics and write the noise in homodyne detection as

$$\frac{(\Delta q_d)^2}{i_d^2} = \frac{1}{4M_i Q_1} \tag{6.3}$$

where Q_1 is given by

$$Q_1 = \frac{Q_1^{(0)}}{1 + 4M_i Q_1^{(0)}(f + rM_i^n)}. \tag{6.4}$$

This effective quantum efficiency provides a useful figure of merit for the experiment and can be compared to measurements of the increase in area of the Bloch vector's noise distribution (discussed in Section 6.6).

Source	Q
Path efficiency, Q_{path}	0.75(3)
Cavity-mode/homodyne overlap, Q_o	0.95(3)
QE of cavity (κ_1/κ), Q_{cav}	0.83(3)
Technical noise from detector, Q_{elec}	0.86(1)
Detector QE, Q_{PD}	0.86(2)
Probe turn-on time, Q_{turnon}	0.86(1)
Total, $Q_1^{(0)}$	0.37(5)

Table 6.2: Quantum efficiency summary table. Quantum efficiency losses come from sources of signal loss and added noise floors. Q_{turnon} comes from finite laser turn-on times and ringing-cancelling "kicks" (see Sec. 6.4.5.5) during which the probe is on but we do not collect information. The total quantum efficiency $Q_1^{(0)} = 0.37(5)$ is the product of all the measured contributions.

6.4.5.5   Limits to noise reduction, optomechanics

The primary limitation to noise reduction R is currently set by optomechanical effects from the probing light. Due to the incommensurate probing and trapping potentials, when the probe light is turned on, the atoms are given an impulse that drives axial oscillations in the trap. Additionally, the minimum of the trapping potential moves in space. This ringing effect is shown in Fig. 6.9 (red) over the 40 μs probing period.

To partially cancel the optomechanical ringing, we employed a 2.5 μs half-power turn-on sequence of the probe laser. The initial half power turn-on induces ringing, while the second, full-power turn-on (applied one quarter of an axial oscillation period later) coherently zeroes the initial axial ringing such that the atoms come to rest at the new trap minimum. As shown in Fig. 6.9, this technique significantly reduced the amount of ringing but only somewhat improved the optimal squeezing in Fig. 3 by an estimated 0.6 dB. Mitigation of optomechanical effects will present a challenge for future experiments aimed at generating even more spin squeezing. Tighter trapping or homogeneous coupling of atoms to the atomic probe could be avenues toward reducing optomechanical effects.
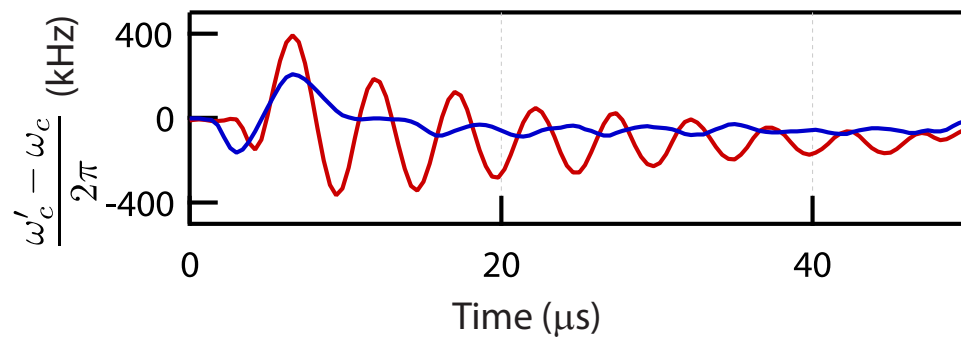
Figure 6.9: Probe induced oscillations partially cancelled by a staggered turn-on sequence. The oscillations are fully present with no kick (red, 43 traces averaged) during a 40 μs measurement, but greatly reduced by a half-power 2.5 μs kick (blue, 30 traces averaged). The 2.5 μs kick length corresponds to a quarter of the axial trap oscillation period. There is an 80 MHz offset subtracted from the vertical axis.

6.5   Background contrast correction

The spin squeezing values presented in the main text were calculated using the slightly modified relationship $S = RC_{BG}/C^2$ described in Ref. [173]. Here $C_{BG} = 0.96$ is the background contrast as determined from measurements of the contrast at $M_i = 0$ probe photons. For clarity of presentation we approximated $C_{BG} = 1$ for the expressions in the main text. Using the more exact formula represents a small 0.2 dB improvement in the reported squeezing compared to what would be calculated with $S = R/C^2$.

6.6   Antisqueezing and area of the noise distribution

The noise in the backaction (or antisqueezed) quadrature of the squeezed state was measured using the sequence in Fig. 3(c) of the main text, with the variable rotation ψ inserted, and measurement outcomes here labeled J_{zp} and $J_{zf}(\psi)$ for the first and second measurements respectively. This measurement sequence was used to make the visualization of the squeezed state shown in Fig. 3(e) of the main text. In order to construct a meaningful probability distribution describing our state, we constructed the normalized probability distribution $P\left(J_{zf}\left(\psi\right) - \cos\psi J_{zp}\right)$ for obtaining a differential measurement outcome $J_{zf}(\psi) - \cos\psi J_{zp}$. The weighting of the premeasurement by $\cos\psi$ ensures that we only condition the final measurement on the premeasurement to the degree that the two spin projections overlap. We performed an inverse Radon transform [94] on the measured $P\left(J_{zf}\left(\psi\right) - \cos\psi J_{zp}\right)$, yielding the conditional probability distribution shown in Fig. 3(e) of the main text.

We now consider the magnitude of the noise in the backaction quadrature versus the number of probe photons M_i. We generalize the spin noise reduction to now be a function of ψ as $R(\psi) = \Delta\left(J_{zf}\left(\psi\right) - \cos\psi J_{zp}\right)^2 / \Delta J_{z,QPN}^2$. The antisqueezing is defined as $A \equiv R(\pi/2)C_{BG}/C^2$, in direct analogy to the Wineland squeezing parameter, $S = R(0)C_{BG}/C^2$. The antisqueezing parameter can be interpreted as the noise variance in the azimuthal phase of the Bloch vector relative to the standard quantum limit $A \approx (\Delta\phi/\Delta\phi_{\mathrm{SQL}})^2$, up to the small correction for the background contrast

$C_{BG} = 0.96$.

The antisqueezing A is plotted in Fig. 6.10 versus M_i. The data is fit to a model that includes three contributions $A = A_0 + A_1 M_i + A_2 M_i^2$. The quantum backaction should rise linearly with M_i and is therefore parameterized by A_1. The contribution of this term to the total backaction is shown by the blue shaded region. Classical intensity noise on the probe laser power circulating inside the cavity (for example) would contribute backaction noise scaling as M_i^2. The classical backaction is therefore parameterized by A_2, with this classical contribution to the total backaction shown by the red shaded region. Lastly, the constant term A_0 is attributed primarily to the projection noise as well as noise in the rotations.

Squeezing data S was taken at the same experimental settings (gold points and line in Fig. 6.10). This allows us to infer the angular area of the quantum noise distribution, $\Delta\phi\Delta\theta/\Delta\theta_{\mathrm{SQL}}^2 = \sqrt{SA_1/C_{BG}^2}$, shown in purple in Fig. 6.10(b).

The increase of the area of the noise distribution can also be used as an alternate, global measurement of the quantum efficiency Q_1 in Section 6.4.5.4. Specifically, the total quantum efficiency of the entire measurement sequence is proportional to the square of the increase in the angular area of the noise distribution and can be written $\tilde{Q}_1 = 4/(A_1 S C^2/C_{BG}^2)$. The factor C^2 comes from the angular momentum uncertainty relation and accounts for the fact that the SQL increases as the Bloch vector shrinks. As mentioned in the main text, the factor of four arises due to finite measurement strength and an unused premeasurement. $\tilde{Q}_1$ as measured by the area of the noise distribution is plotted in Fig. 6.10(b) in gold. The gold shaded region represents the uncertainty in the extrapolation of $\tilde{Q}_1$ due to uncertainty in the fit of the antisqueezing data of Fig. 6.10(a). At low photon number, $\tilde{Q}_1$ agrees with the predicted value of $Q_1^{(0)}$ from Table 6.2. At higher photon number, $\tilde{Q}_1$ begins to rise due to the effective quantum efficiency losses from the technical noise floor and optomechanics discussed in Section 6.4.5.4.
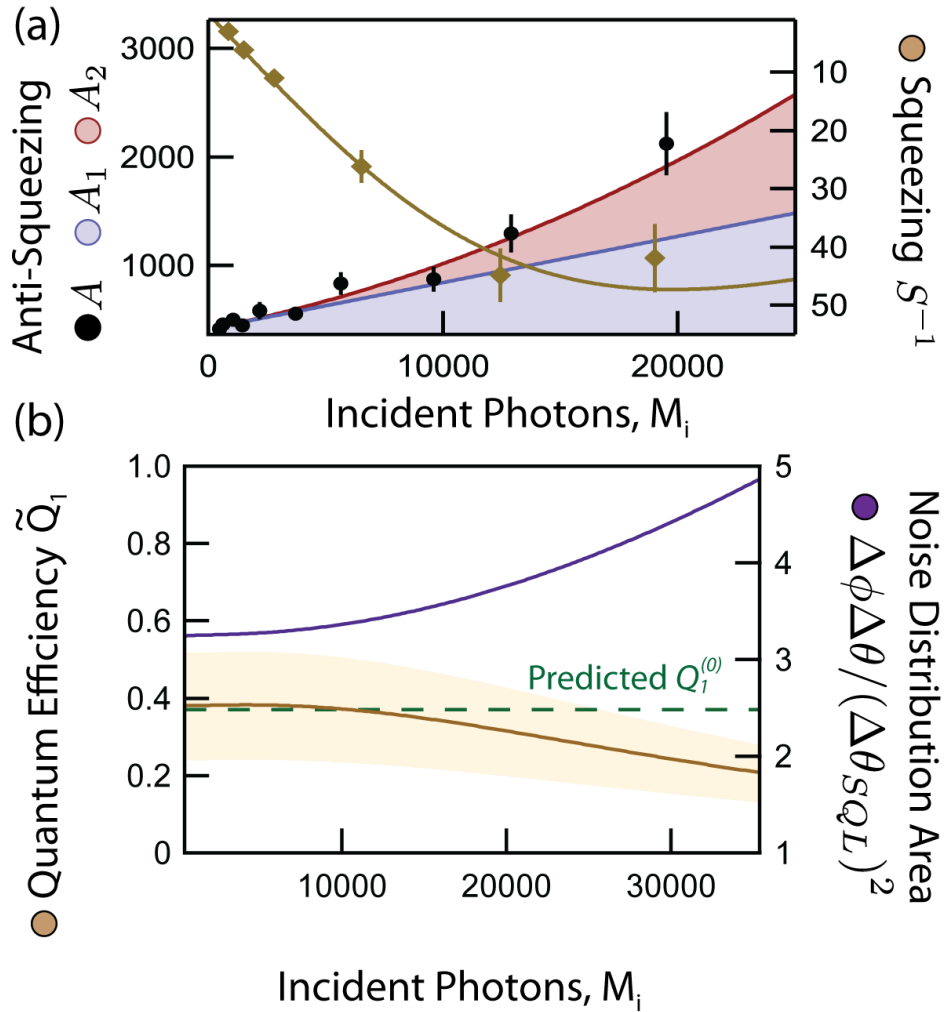
Figure 6.10: (a) The antisqueezing A is plotted versus M_i (black circles). The linear contribution to the rise in A, A_1, is shown in blue and the quadratic contribution A_2 in red. The squeezing (gold diamonds and fit) is plotted on the right axis. (b) The area of the noise distribution is calculated from the data in part (a) and plotted in purple. The measured effective quantum efficiency $\tilde{Q}_1$ is plotted in gold with an error bar shown as a gold band. At low M_i, $\tilde{Q}_1$ is consistent with the prediction (green dash) $Q_1^{(0)}$ from Table 6.2.

6.7 Feedback implementation

6.7.1 Experimental details

Real-time feedback to steer the atomic spin projection to a target spin projection J_z is implemented with an Arduino Due microcontroller with an internal clock of 84 MHz. The microcontroller is programmed to sample the loop filter L_{SHA} output voltage (directly related to $N_\uparrow$) during the $N_{\uparrow p}$ and $N_{\downarrow p}$ measurement windows, and the sampling rate allows for averaging 18 points in each 40 μs window. The microcontroller then calculates J_{zp} from the difference of the two measurement windows and applies the feedback microwave rotation to the atoms through the formula $\theta_{fb} \approx 2 \times (J_{ztar} - J_{zp})/N$ where J_{ztar} is the target value for J_z. Fluctuations in N are small enough that it can be taken as a constant. The microcontroller controls the microwave rotation angle by varying the duration for which the microwaves are applied using a high speed microwave switch (Minicircuits ZASW-2-50-DR+) (labelled `rot` in Fig. 6.6) with single clock cycle (12 ns) resolution. The sign of the rotation is controlled by another digital output of the Arduino that toggles a switch denoted `sign` between two microwave sources that are 180° apart in phase, as shown in Fig. 6.6. Microwave rotations to accomplish $\pi/2$ and π pulses can also be applied independently of the Arduino using digital outputs from the data acquisition computer (not shown), though with less timing resolution.

6.7.2 Limitations to squeezing with feedback

As mentioned in the main text, the primary limitation to deterministic squeezing is noise imposed from microwave rotations. We estimate these noise sources by performing two additional variations of the measurement sequence of Fig. 2 of the main text, removing either the feedback rotation θ_{FB} or all rotations.

At the optimal deterministic spin squeezing with feedback, we achieve $R^{-1} = 9.5(4)$ dB. To estimate the noise added from feedback, we measure conditional spin noise $J_{zf} - J_{zp}$ in a sequence with no feedback and find $R^{-1} = 12.4(7)$ dB. Feedback leads to approximately 2.9 dB of added

noise. Next, we perform the sequence with no microwave rotations of any kind, effectively measuring the same spin population $N_\uparrow$ four times. In this sequence we attain $R^{-1} = 14.0(5)$ dB, 1.6 dB less than the sequence with rotations but no feedback. This measurement suggests a rotation noise floor due to microwave amplitude and frequency noise that is approximately 17.5 dB below projection noise. Further, we suspect that rotation noise is also a primary contribution to the additional noise from adding feedback, since certain rotation errors which cancel after two π pulses will no longer cancel when feedback is applied. Improving the precision of microwave rotations remains a major obstacle in working with atomic spin states with extreme phase resolution.

Chapter 7

Spatially Homogeneous Spin Squeezing for Atom Interferometry

7.1   Introduction

Spin-squeezed states could be used to improve a wide range of quantum sensors, with today's best atomic clocks [115, 66, 76] being particularly promising candidates [121]. In this chapter I focus on preparing spin-squeezed states appropriate for matter-wave atom interferometry with applications including inertial sensing [9], measurements of gravity and freefall [135, 141], and even the search for certain proposed types of dark matter and dark energy [131, 61].

A major challenge arises for cavity-based atom interferometry and other applications involving release of spin-squeezed atoms into free space. The problem is that the probe mode used to perform the collective measurement is a standing wave, but the atoms are trapped in a 1-dimensional lattice defined by a standing wave cavity mode with a significantly different wavelength. Some atoms will sit in lattice sites positioned near nodes and some near anti-nodes of the entanglement-generating probe light. As a result, the atoms will contribute to the collective measurement with different strengths. In this common case, the large degree of squeezing exists only for this specific coupling configuration and would be largely lost after releasing the atoms into the arm of an interferometer, since their final coupling to the cavity mode or other readout detector will be different from the original configuration [70]. In contrast, we wish to create spatially homogeneous entanglement, quantified by the amount of observed phase resolution beyond the SQL that one can achieve when every atom couples equally to the final measurement apparatus.

7.2   Homogeneous squeezing in an effective optical dipole trap

In this section, I demonstrate a method to create homogeneous spin-squeezed states in a standing wave optical cavity by allowing the atoms to traverse many wavelengths of the standing wave probe during each collective measurement. Atoms experience a time-averaged coupling to the cavity so that every atom is measured with the same strength, ensuring homogeneous entanglement. We do this by creating an optical trap with a uniform axial potential, which we refer to as an effective "dipole trap" as opposed to the standing-wave "lattice". The dipole trap maintains transverse confinement of the atoms while allowing free movement subject to gravity along the vertical cavity axis. We demonstrate 11(1) dB of directly observed squeezing via collective measurements in the dipole trap, the most directly observed spin squeezing ever achieved apart from Refs. [39, 68], and use fluorescence images and noise scalings to show that the generated squeezing is homogeneously shared among the atoms to a large degree, in principle allowing significant amounts of squeezing for free space or guided matter-wave interferometry. We also discuss the limits placed on entanglement generation with time-averaged measurements.

Homogeneous squeezing can also be obtained using a travelling wave "ring" cavity [13], but birefringence must be controlled to maintain the efficacy of utilizing cycling transitions [32]. Another appealing approach is to introduce a commensurate lattice [68, 91]. This approach requires special mirror coatings and frequency doubling equipment and doesn't permit guided movement for atom interferometry within the cavity mode. Homogeneous entangled states can also be obtained without using a cavity [56, 4, 12, 114, 62], but free space experiments have not yet achieved the large amounts of squeezing observed using optical cavities.

In this work, we use the pseudo-spin states defined by the ground hyperfine states of ^{87}Rb, with $|\downarrow\rangle \equiv |5^2S_{1/2}, F = 1, m_F = 1\rangle$ and $|\uparrow\rangle \equiv |5^2S_{1/2}, F = 2, m_F = 2\rangle$ split by 6.8 GHz. As in Refs. [39, 32], we describe the total pseudo-spin state of N atoms by a collective Bloch vector $\vec{J}$, with spin projections J_x, J_y, and J_z. The spin projection on a single trial $J_z = N_\uparrow - \frac{N}{2}$ is determined by making a collective measurement of the total number of atoms in the upper spin state $N_\uparrow$. For an

unentangled, coherent spin state (CSS), quantum projection noise (QPN) leads to fluctuations in J_z of size $\Delta J_{z,QPN} = \sqrt{N}/2$. In this work, ΔX will refer to the standard deviation of a quantity X as measured over repeated trials of the experiment.

The collective measurement is performed using the experimental apparatus and techniques described in Ref. [39]. In brief, we trap ^{87}Rb atoms in the central 2 mm of a 2 cm optical cavity with finesse $F = 2532(80)$. A cavity mode is tuned $\delta_c = 2\pi \times 400$ MHz to the blue of the $|\uparrow\rangle$ to $|e\rangle \equiv |5^2P_{3/2}, F = 3, m_F = 3\rangle$ transition. The cavity resonance frequency ω is shifted by an amount depending on the number of atoms in $|\uparrow\rangle$ due to the dispersive interaction between the atoms and cavity. The cavity's resonance frequency is measured by probing the cavity in reflection for 40 μs. The probing is collective because it is not possible to tell from the single probe mode precisely which atoms are in $|\uparrow\rangle$.

In a single trial, we apply resonant microwaves to prepare each atom in an equal superposition $(|\uparrow\rangle + |\downarrow\rangle)/\sqrt{2}$. We then perform two consecutive measurements of the projection J_z, with the two measurement outcomes labeled J_{zp} and J_{zf}, with subscripts denoting pre and final measurement. The quantum projection noise is common to the two measurements and is removed when we take the difference between the pre and final measurements, yet the atoms nearly completely retain coherence of the quantum phase between $|\uparrow\rangle$ and $|\downarrow\rangle$. This allows one to sense a quantum phase that evolves between the final and premeasurements below the SQL.

The atoms are initially cooled to approximately 10 μK and trapped in a far off resonance red detuned optical lattice at $\lambda_l = 823$ nm (with corresponding wave vector $k_0 = 2\pi/\lambda_l$). We then convert this standing-wave lattice into an effective dipole trap. This is achieved by simultaneously driving multiple TEM$_{00}$ longitudinal modes of the cavity near 823 nm. Adjacent longitudinal modes have opposite symmetry with respect to the cavity center. To lowest order, near the center of the cavity, one mode creates a $\cos^2(k_0z)$ standing-wave intensity profile while the next mode creates a $\sin^2(k_0z)$ intensity profile such that the sum of the two standing waves $\cos^2(k_0z) + \sin^2(k_0z) = 1$ creates a net uniform intensity profile along the cavity axis as shown in Fig. 7.1(a).

To drive adjacent longitudinal modes, we phase modulate the lattice light at the cavity
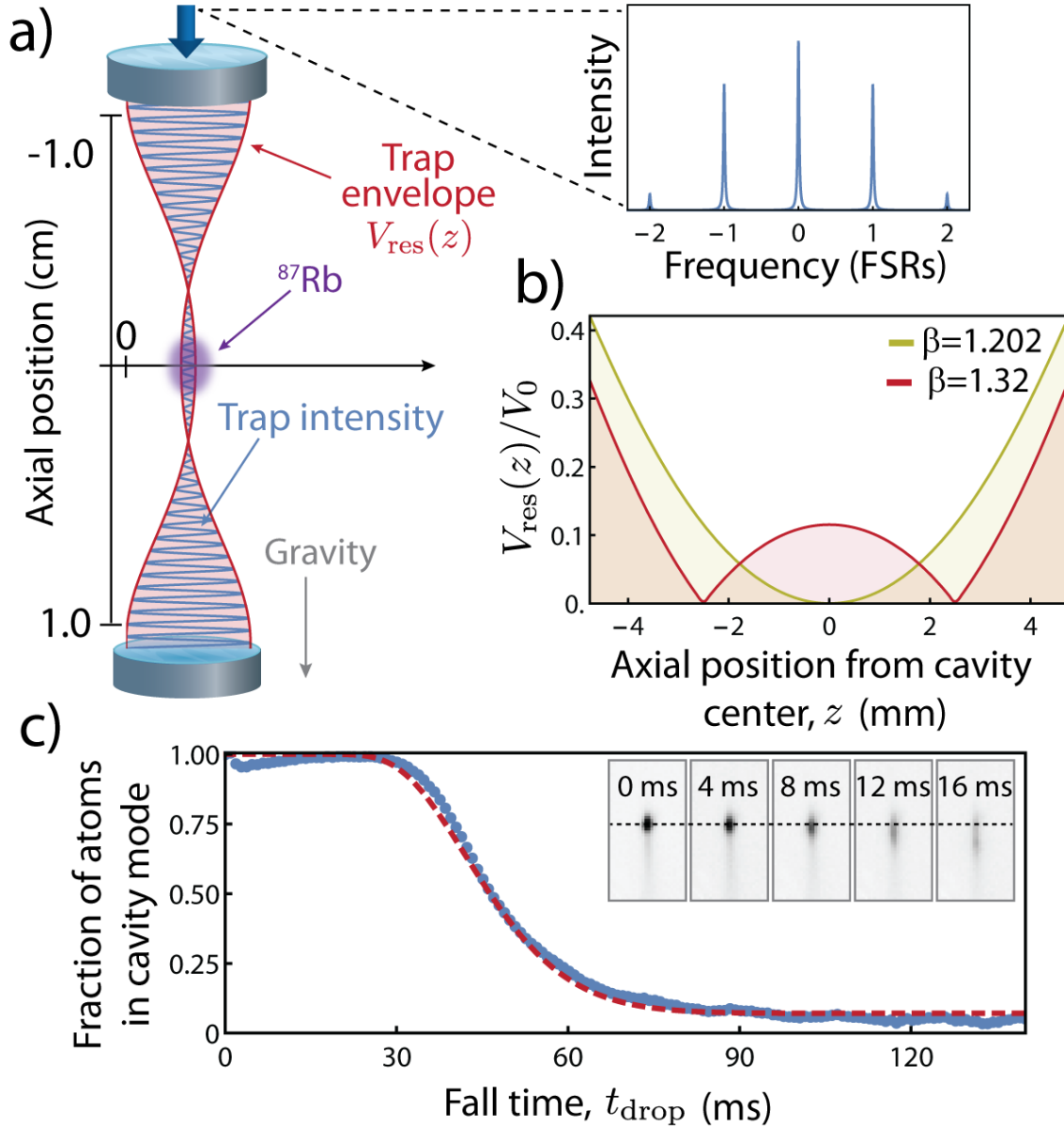
Figure 7.1: (a) Optical lattice sidebands separated by one free spectral range (FSR) are injected into the cavity to create an axially homogeneous "dipole" trap. Dipole trap intensity (blue) and its envelope (red) plotted inside of the optical cavity, with exaggerated wavelength $\lambda_l \times 10^3$. (b) The envelope of the residual lattice potential $V_{res}(z)$ normalized to the peak lattice potential depth V_0 is plotted near the cavity center, optimized for a minimum at $z = 0$ (gold, $\beta = 1.20$) and for the minimal fraction of trapped atoms determined experimentally (red, $\beta = 1.32$). (c) Fraction of atoms remaining in the cavity mode (blue points) vs. fall time, fit to a model (red dash) described in the text. Fluorescence images show the falling atom cloud at various times (inset).

free spectral range (FSR), FSR $= 2\pi \times 8.1050(5)$ GHz, using a fiber-coupled phase modulator.

The resulting axial component of the potential at distance z from the cavity center can be written

$V(z) = V_0[J_0^2(\beta)\cos^2{(k_0 z)} + J_{-1}^2(\beta)\sin^2{((k_0 + \delta k_{-1})z)} + J_1^2(\beta)\sin^2{((k_0 + \delta k_1)z)} + \ldots]$, where $J_n(\beta)$

is the nth Bessel function and β is the modulation index. $\delta k_n = n\text{FSR}/c$ is the additional wave

vector for the sidebands offset by n cavity free spectral ranges, with speed of light c. Interference

terms between sidebands are neglected since they oscillate at 8 GHz.

Figure 7.1(b) shows the depth of the residual standing-wave lattice potential in the dipole

trap $V_{\text{res}}(z)$ as a function of distance from the center of the cavity for two different values of β.

We find $\beta \approx 1.32$ (overdriving the dipole trap) to be the optimum value for freeing atoms to move.

This is due to a wider minimum of $V_{\text{res}}(z)$ which overlaps the atomic spatial distribution as well

as the fact that overdriving causes the lattice potential wells to be converted into small potential

peaks, giving atoms additional potential energy.

When an atom begins to fall in the dipole trap, the increase in the residual lattice depth is

not sufficient to stop the atom from continuing to fall; rather, we expect the atom to be guided by

the optical dipole trap until it collides with the lower mirror. In Fig. 7.1(c), we measure the number

of atoms in the cavity as a function of freefall time, t_{drop}, by continuously monitoring the dispersive

shift of the cavity resonance frequency. The data is renormalized to account for background atom

loss and is reasonably described by a fit (purple line) which assumes atoms are guided by the net

transverse intensity profile of the dipole trap until they are lost when they collide with the lower

mirror. For comparison, ballistic expansion out of the cavity mode would occur in only 2 ms were

we to simply turn off the optical lattice. The free fall and guiding are corroborated by fluorescence

measurements such as shown in Fig. 7.1(c) inset for various t_{drop}. Figure 7.1(c) and fluorescence

images indicate that at long times only 5(1)% of the atoms remain trapped in a residual lattice. The

majority of the atoms move along the cavity axis, the key for obtaining time-averaged homogeneity

in the coupling of the atoms to the standing-wave probe mode.

For a fixed total atom number, we expect the projection noise induced fluctuations in the

cavity resonance frequency $\Delta\omega_{\text{QPN}}$ to be smaller in the dipole trap than in the lattice. While

the total dispersive shift is the same in both cases, in the lattice the dominant contribution is
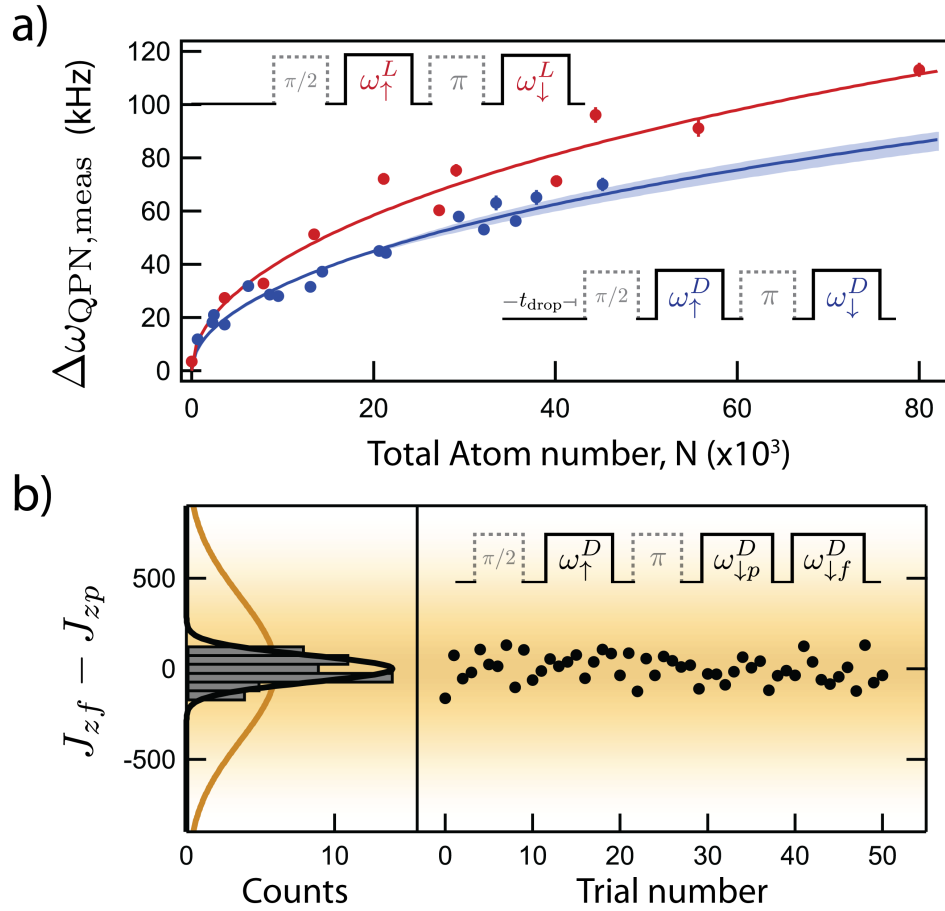
Figure 7.2: (a) Projection noise scaling versus total atom number N, measured in the lattice (red points) including a theoretical prediction (red line) and in the dipole trap (blue points) including a fit to infer a coupling fraction ζ (blue line, with 68% confidence interval bands). Sequences are inset. Dashed boxes represent Bloch vector rotations through a given angle using resonant microwaves. Solid boxes represent cavity frequency measurements. (b) Quantum noise reduction in the dipole trap with $6.3(3) \times 10^5$ atoms. A histogram of $J_{zf} - J_{zp}$ (black data points) shows a standard deviation 13.9(6) dB below projection noise $\Delta J_{z,QPN} = 397$ atoms (gold line and shaded distribution). The measurement sequence is inset.

from the subset of atoms situated near antinodes of the probe. These atoms have a Jaynes-Cummings coupling parameter g_i near the maximum value $g_0 = 2\pi \times 0.519(5)$ MHz and provide stronger than average fluctuations. In the ideal time-averaged situation, on the other hand, the full ensemble only couples with the rms coupling strength $g_{rms} = g_0/\sqrt{2}$, actually leading to weaker cavity frequency fluctuations. To quantify the level of homogeneous coupling, we define a model where fractionally, ζ of the atoms release into the dipole trap and are assumed to have perfectly homogeneous coupling. $1 - \zeta$ of the atoms remain fixed in position and maintain their original coupling. In this model, the projection noise induced fluctuations in the cavity resonance frequency can be written $\Delta\omega_{\mathrm{QPN}} = g_{\mathrm{rms}}^2 \sqrt{N(3 - \zeta)}/\sqrt{8(g_0^2 N + \delta_c^2)}$ (See Section 7.5).

We observe this change in the projection noise scaling between the lattice and dipole trap by performing the measurement sequences of Fig. 7.2(a) in the lattice (red, superscript L) and in the dipole trap (blue, superscript D) versus the total atom number in the cavity N. The $\omega_\uparrow$ and $\omega_\downarrow$ windows represent the outcome of a measurement of the cavity resonance frequency, sensitive to $N_\uparrow$ or $N_\downarrow$ respectively, and we plot the observed projection noise fluctuations $\Delta\omega_{\mathrm{QPN,meas}} = \Delta(\omega_\uparrow - \omega_\downarrow)$ in either the lattice or the dipole trap. A small amount of technical noise that does not have the proper scaling with atom number has been subtracted out of this data. The lattice data is used as a calibration of g_0 with the theoretical scaling plotted in red. The dipole trap data is fit to the model $2 \times \Delta\omega_{\mathrm{QPN}}$ (since the measurement sequence includes two anti-correlated windows, $\omega_\uparrow$ and $\omega_\downarrow$) with ζ as a free parameter. We fit $\zeta = 1.0(2)$, consistent with our expectation of 95% from the data in Fig. 7.1(c).

By consecutively performing a pre and final measurement $\omega_\downarrow^{\mathrm{D}}$, labeled $\omega_{\downarrow p}^{\mathrm{D}}$ and $\omega_{\downarrow f}^{\mathrm{D}}$ we can show a large degree of spin noise reduction below QPN and correspondingly demonstrate the creation of entangled, spin-squeezed states in the dipole trap. We measure spin squeezing using the Wineland criterion for phase enhancement relative to the SQL, $(\Delta\theta/\Delta\theta_{\mathrm{SQL}})^2 \equiv S = R/C^2$ [174, 39]. The observed spin noise reduction normalized to the quantum projection noise level is $R = (\Delta(J_{zf} - J_{zp})/\Delta J_{z,QPN})^2 < 1$. Squeezing or enhanced phase resolution also requires the additional demonstration of retained coherence, or Bloch vector length, often referred to as

"contrast", $C \equiv 2|\vec{J}|/N$.

The measurement sequence is shown in the inset of Fig. 7.2(b) and is the same as that of Ref. [39]. We use $t_{\text{drop}} = 13$ ms, which accelerates the atoms enough to average over approximately 13 cycles of the probe standing wave during the 40 μs measurement window. Figure 7.2(b) shows noise in measurements of $\omega_{\downarrow f}^{\text{D}} - \omega_{\downarrow p}^{\text{D}}$ in the dipole trap with total atom number $N = 630(30) \times 10^3$ atoms. Experimental parameters g_{rms}, δ_c, and N are used to scale between cavity frequency measurements and J_z, $\partial\omega/\partial J_z = g_{rms}^2/\sqrt{4g_{rms}^2 N_\uparrow + \delta_c^2}$. The data is collated into a histogram on the left, showing a standard deviation 13.9(6) dB less than the projection noise level shown in yellow. The remaining contrast after the premeasurement was independently measured, $C = 0.70(5)$. Together with the noise reduction, this yields a directly observed phase resolution, or spin squeezing, of $S = 1/13(3)$ or $-11(1)$ dB below the SQL

7.3 Coupling oscillations

When the cavity frequency is measured in a 40 μs window using the dipole trap, oscillations in the signal are observed, indicating the atomic motion over the probe standing wave. Specifically, we measure the number of atoms $N_\uparrow$ that are coupled to the cavity as a function of time by applying a scale factor to convert cavity frequency to atom number. We refer to this rescaled time signal as $\mathcal{N}(t) = \sum_i^{N_\uparrow} g_i^2(t)/g_{\text{rms}}^2$. We observe noise in the atom's coupling in the frequency domain, which can be used to infer the distribution of atoms' coupling oscillation frequencies. Most of the coupling oscillations average away, since the oscillation of each atom occurs with a random phase. However, the residual uncancelled coupling oscillations are observed in $\mathcal{N}(t)$ such that the squared Fourier transform of the time signal, $|\tilde{\mathcal{N}}(f)^2|$ has units of Atoms/Hz and is closely related to the atomic velocity distribution.

Figure 7.3(a) shows $|\tilde{\mathcal{N}}(f)^2|$, recorded using 2 ms of data and taking the average power spectrum of time traces from approximately 65 trials. The data was taken after 1 ms (blue), 7.5 ms (red), and 15 ms (green) of freefall time after release into the dipole trap. Each power spectrum is fit to an appropriately folded 1D Boltzmann distribution that accounts for the inability to distinguish
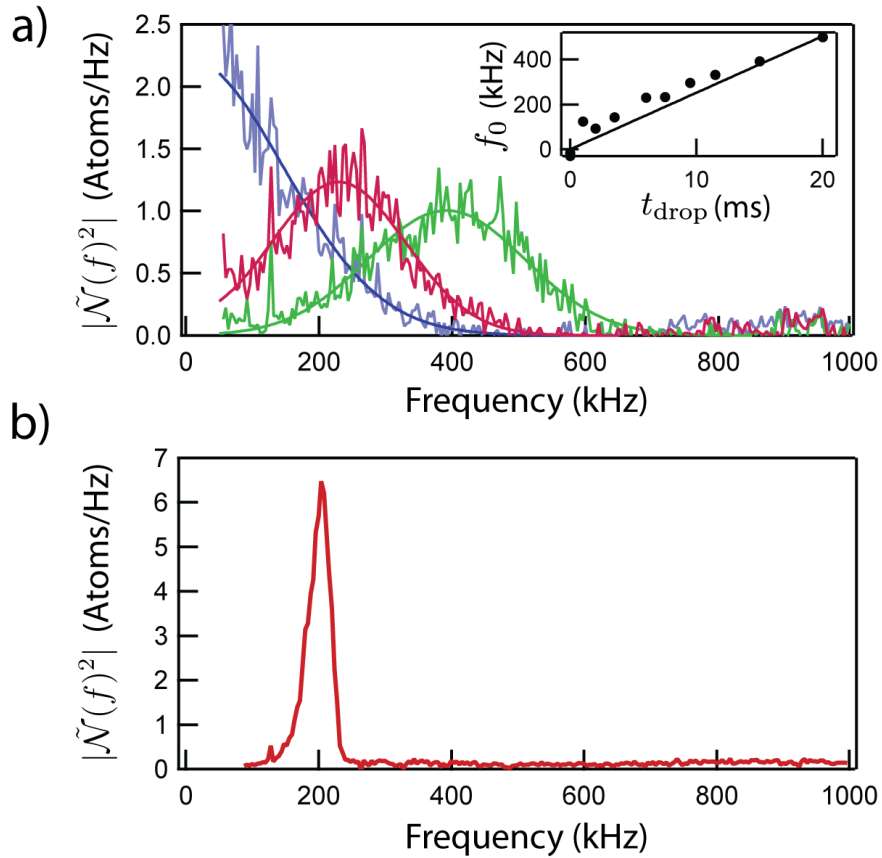
Figure 7.3: (a) Power spectra showing coupling oscillations for fall times of 1 ms (blue), 7.5 ms (red) and 15 ms (green) with their respective fits. (inset) Center frequency f_0 of the fitted Boltzmann distribution for various fall times (points) compared to a freefall prediction line of $f_0 = 2at/\lambda_p$ (line), see text for definitions. (b) Power spectrum showing coupling oscillations at the trap frequency when atoms are trapped in the optical lattice.

between upwards and downwards velocities. The fit center frequency f_0 is plotted as a function of the freefall time t in the inset of Fig. 7.3(a). The result is consistent, particularly at long times, with the simple prediction, $f_0 = a\,t/(\lambda_p/2)$, where $a = 9.81$ m/s^2 is the acceleration due to gravity. The widths of the distributions are consistent with Boltzmann distributions giving final axial temperatures of 25 μK. To contrast, Fig. 7.3(b) shows $|\tilde{\mathcal{N}}(f)^2|$ for atoms in the lattice. Instead of a large thermal distribution, a narrow distribution is observed at the lattice trap frequency, about 200 kHz.

7.4 Outlook for atom interferometry

In summary, we infer that we have created a spatially homogeneous squeezed state from the combined observations of Figs. 1-3. First, we observe release of 95(1)% of the atoms (Fig. 7.1) at a sufficient velocity (Fig. 7.3) to ensure, on average, 13 averaging cycles of the probe standing wave during a 40 μs collective measurement. In Fig. 7.2(a) we also confirm the transformation to homogenous coupling by the change in scaling of projection noise fluctuations of the cavity. The demonstration of 11(1) dB of observed squeezing in the homogeneous configuration proves our ability to create a large amount of entanglement in this highly time-averaged scheme.

We investigate the limits to squeezing using our time-averaged scheme in the Section 7.5. Since the ac signals in Fig. 7.3 yield additional information about the spin state of each velocity component of the atomic ensemble, time averaging will fundamentally limiting the squeezing to order $S \propto \frac{1}{qN}$, where q is the total quantum efficiency of the experiment. For $q \sim 1$, this is close to the Heisenberg limit. The more relevant limitation for our system is imperfect averaging of the probe standing wave. For 40 μs measurements after a 13 ms drop time and for a 25 μK ensemble, we estimate that the observed noise reduction should be limited to 15 dB below QPN, which we believe to be a primary limitation to our observed spin noise reduction of 13.9(6) dB. In the future, this limit could be improved using longer measurement windows to average over more cycles of the probe standing wave during each measurement.

To realize a free space matter-wave interferometer, atoms could be prepared in the cavity for

the entanglement generating premeasurement, then released into free space for an interferometry sequence. The final measurement could be performed with fluorescence detection. The 5% of atoms with non-uniform coupling during the premeasurement would lead to an additional noise floor, not observed in this work, of 13 dB below the SQL. Additionally, inhomogeneity from radial motion will lead to another additional noise floor of approximately 10 dB below the SQL [39]. Notably, this radial motion would also equally affect systems using ring cavities, commensurate lattices, or other axial averaging techniques.

Another possibility is to perform guided interferometry inside the cavity mode. Here the pre and final measurements would both be performed with collective cavity measurements. In this case, the noise from the 5% of atoms remaining trapped and radial motion largely cancels at short times. The 11(1) dB of squeezing observed in this work would in principle fully translate to this type of interferometer. In addition to the possibility of using entangled states, performing the final readout via a cavity measurement may allow for reduced technical noise, higher bandwidth, cleaner optical modes, and power buildup for Raman transitions [60].

Similarly, higher order transverse modes, atom-chip technologies [168, 176], or tailored potentials [58, 97] might be combined with the cavity measurement technique presented here to create new varieties of matter-wave Sagnac interferometers and other inertial sensors. The real-time observation of mechanical motion also opens the path to stochastic cooling schemes based on measurement and feedback [166] with applications to more complex systems such as molecules, which can be challenging to laser cool using conventional Doppler cooling methods.

7.5   Squeezing limits from time averaging

7.5.1   Introduction

As shown in the Main Text, time averaging the probe standing wave during collective cavity measurements can be used to create homogeneous squeezing within an atomic ensemble in a cavity. However, the technique introduces limitations to spin squeezing in addition to the fundamental

limits calculated in Ref. [32] set by finite collective cooperativity $N\mathcal{C}$, finite quantum efficiency for detecting the probe light q, and the probability of the probe light inducing a spin flip p. Specifically, the best achievable spin squeezing is $S = \mathrm{Max}\left[e/(qN\mathcal{C}), \sqrt{8p/(qN\mathcal{C})}\right]$ where the first limit $(e/(qNC))$ is due to wave-function collapse from free space scattering and the second limit $(\sqrt{8p/(qN\mathcal{C})})$ is due to additional noise from Raman spin flips. Here, we calculate the additional limits to S imposed by time averaging the spatially inhomogeneous coupling.

First, we establish the language for describing the limits on spin-noise reduction R when the coupling coefficient of each atom differs between the pre and final measurement windows, with results closely matching those of Hu *et al.* [70]. We apply this formalism to determine the best achievable spin-noise reduction, and therefore best spin squeezing for two concrete scenarios relevant to matter-wave interferometry with squeezed states. First, we consider the scenario in which we perform the premeasurement of the spin state with the atoms trapped in an incommensurate 1D intracavity lattice and then perform the final measurement with uniform coupling. Next, we consider the case of incomplete cycle averaging over the standing wave probe mode if the atoms are allowed to move along the cavity axis during the pre and final measurements.

Next, we calculate two sources of inhomogeneous broadening, or dephasing, that arise from time averaging. This dephasing leads to a loss of contrast or signal. The first source is fundamental quantum back-action that arises from the atoms sampling the photon shot noise of the intracavity probe light at different times, or equivalently, spectral frequencies. The second source arises from imperfect cycle averaging of the probe coupling. We show that these two limiting effects do not significantly impact current experiments, and can in principle allow spatially homogeneous squeezing near the Heisenberg limit.

7.5.2   Noise reduction limits with inhomogeneous coupling

7.5.2.1   Noise between the final and premeasurement

To find the optimum spin-noise reduction with inhomogeneous coupling, we begin with an expression for a measurement of atoms in a cavity where we assume each atom i couples to the optical cavity with a factor $\eta_{mi}(t)$ in the pre ($m = p$) or final ($m = f$) measurement. Concretely, we can write $\eta_{mi}(t) = g_{mi}^2(t)/\delta_c$ when we are in the dispersive regime of cavity measurements, where δ_c, the optical cavity detuning from the atomic transition, is much greater than $\Omega = 2g_{\mathrm{rms}}\sqrt{N}$, the collectively enhanced coupling rate between the atoms and the cavity, or vacuum Rabi splitting [32]. $g_{mi}^2(t)$ is the ith atom's time dependent Jaynes-Cummings coupling parameter. We consider the average outcome of the measurement by taking the time average of $\eta_{mi}(t)$, denoted by dropping the time dependence (t). As a reminder, g_{rms}^2 is the average of g_i^2 over the atomic ensemble. Note however, that by changing the units and scaling of η_{mi}, the expressions we derive can be generalized for any type of population measurement such as fluorescence detection. The operator $\hat{\omega}_{mi}$ that measures the time-averaged cavity frequency shift from the ith atom is then

$$\hat{\omega}_{mi} = \left(\hat{\sigma}'_{z,i} + \gamma\right)\eta_{mi}. \tag{7.1}$$

Here, $\hat{\sigma}'_{z,i} = (1-\gamma)(\,|\uparrow_i\rangle\langle\uparrow_i| - |\downarrow_i\rangle\langle\downarrow_i|\,)$ is the Pauli spin operator $\hat{\sigma}_{z,i}$ for the ith atom, rescaled by $(1-\gamma)$. The constant $0 \leq \gamma \leq 1/2$ is used to account for the fact that the measurement may be sensitive to some linear combination of state populations $N_\uparrow$ and $N_\downarrow$, given by $(N_\uparrow - (1-2\gamma)N_\downarrow)$. We include this factor since a number of spin squeezing experiments have used an optical cavity detuned halfway between the $|\uparrow\rangle \rightarrow |e\rangle$ and $|\downarrow\rangle \rightarrow |e\rangle$ transitions [68, 140, 4]. In such cases, the dispersive cavity shift is sensitive only to population differences between $|\uparrow\rangle$ and $|\downarrow\rangle$ and can be modeled with $\gamma = 0$. However, in this work we set the cavity resonance frequency near the $|\uparrow\rangle \rightarrow |e\rangle$ transition (modeled with $\gamma = 1/2$), so there is no sensitivity to $N_\downarrow$. This scheme is advantageous for probing on a cycling transition $p = 0$, as mentioned in the introduction [39, 32, 19]. Additionally, even when the cavity only couples to atoms in $|\uparrow\rangle$, a π-pulse can be used to swap the state populations and

measure $N_\uparrow$ and $N_\downarrow$ sequentially, again achieving a differential measurement with $\gamma = 0$. However, this method is only valid if the atoms' couplings to the measurement do not change between the $N_\uparrow$ and $N_\downarrow$ measurement.

We wish to cancel the quantum projection noise in the final measurement of all N atoms $\hat{\omega}_f = \sum_{i=1}^{N} \hat{\omega}_{fi}$ using a premeasurement $\omega_+ = \sum_{i=1}^{N} \hat{\omega}_{pi}$ of the noise value. However, if the ith atom's couplings η_{fi} and η_{pi} differ, its projection noise cannot be exactly cancelled. In order to optimize the cancellation of the noise, we construct a weighted difference $\hat{\omega}_{\text{diff}} \equiv \hat{\omega}_f - W\omega_+$, with weight factor W. It is important to note that, since our entanglement-generating collective measurements of $\hat{\omega}_f$ and ω_+ must not reveal single-particle information, we can only use a single weight factor for the entire ensemble. Thus, if the change between η_{fi} and η_{pi} is inhomogeneous, that is, different for each atom i, there is no value of W that can be chosen to achieve full cancellation of the noise in the final measurement.

To derive the best achievable squeezing limit with inhomogeneous coupling, we will calculate the noise in the weighted difference $\hat{\omega}_{\text{diff}}$ and find the optimum value for the weight factor W. First, using Eq. 7.1, we calculate the variance $(\Delta\omega_{\text{diff},i})^2$ in $\hat{\omega}_{i,\text{diff}}$ for a single atom. Next, we will independently sum the noise contributions from each atom to calculate the total variance $(\Delta\omega_{\text{diff}})^2$. We neglect all sources of noise in the system except the quantum projection noise and fluctuations in the couplings η_{mi}. Other realistic noise sources such as photon shot noise and laser frequency noise are neglected in order to calculate the squeezing limit just from inhomogeneous coupling. Importantly, the optimum weight factor W for cancelling quantum noise and coupling noise is likely to not be the optimum for cancelling the other technical noise sources such as laser frequency noise. In fact, in our experiments optimum squeezing was always observed with $W = 1$.

The noise variance in $\hat{\omega}_{i,\text{diff}}$ is calculated using

$$(\Delta\omega_{\text{diff},i})^2 \equiv \langle(\hat{\omega}_{fi} - W\hat{\omega}_{pi})^2\rangle - \langle(\hat{\omega}_{fi} - W\hat{\omega}_{pi})\rangle^2, \tag{7.2}$$

where we denote the average over many independent experimental trials with the $\langle...\rangle$ notation. This trial average will simultaneously evaluate the quantum fluctuations of the spin projection operator

$\hat{\sigma}'_{z,i}$ as well as possible fluctuations in the time-averaged couplings η_{mi}. In calculating averages, we will reasonably assume that fluctuations in the couplings are uncorrelated with fluctuations in the spin projection operator, leading to

$$(\Delta\omega_{\text{diff},i})^2 = \langle(\hat{\sigma}'_{z,i} + \gamma)^2\rangle\langle(\eta_{fi} - W\eta_{pi})^2\rangle \tag{7.3}$$

$$- \langle\hat{\sigma}'_{z,i} + \gamma\rangle^2\langle\eta_{fi} - W\eta_{pi}\rangle^2. \tag{7.4}$$

We now limit the discussion to the relevant case of atoms in an equal superposition of $|\uparrow\rangle$ and $|\downarrow\rangle$ such that $\langle\hat{\sigma}'_{z,i}\rangle = 0$. However, we leave the expectation value $\langle\hat{\sigma}'^2_{z,i}\rangle$ unevaluated. This helps to illuminate different contributions to $(\Delta\omega_{\text{diff},i})^2$ and also allows for the possibility of atoms being in different entangled or mixed states.

$$(\Delta\omega_{\text{diff},i})^2 = \langle\hat{\sigma}'^2_{z,i}\rangle\left[\langle\eta^2_{fi} + W^2\eta^2_{pi} - 2W\eta_{fi}\eta_{pi}\rangle\right] \tag{7.5}$$

$$+ \gamma^2\left[(\Delta\eta_{fi})^2 + W^2(\Delta\eta_{pi})^2 - 2W\text{Cov}(\eta_{fi}, \eta_{pi})\right] \tag{7.6}$$

where $\text{Cov}(X, Y) = \langle XY\rangle - \langle X\rangle\langle Y\rangle$ is the covariance between X and Y. As a reminder, the covariance quantifies the correlation of the fluctuations of X and Y. If X and Y are uncorrelated, then $\text{Cov}(X, Y) = 0$. If X and Y are perfectly correlated, then $\text{Cov}(X, Y) = \Delta X\Delta Y$ where ΔX is the standard deviation in the quantity X. There are two contributions to $(\Delta\omega_{\text{diff},i})^2$. The first (line 7.5) is the term arising from uncancelled quantum projection noise and will be nonzero if the couplings, $W\eta_{pi}$ and η_{fi}, are not equal to one another. This term captures the fundamental problem of inhomogeneous coupling to the collective measurement.

The second contribution proportional to γ (line 7.6) results from trial-to-trial noise in the couplings η_{fi} and η_{pi} and is fully classical, since it has no contribution from projection noise, that is, $\langle\hat{\sigma}'^2_{z,i}\rangle$. The physical origin of this term can be thought of as trial-to-trial noise in the scale factor relating an observed cavity frequency shift to an estimated population of atoms in spin up or down. When $\gamma = 0$, the cavity frequency shifts are proportional to $N_\uparrow - N_\downarrow$ which is on average zero for the case considered here. As a result, any noise in the scale factor contributes no additional noise.

However, if $\gamma = 1/2$, then the cavity frequency shifts are proportional to $N_\uparrow$ which for the case considered here is approximately $N/2$. In this case, classical scale factor noise can easily contribute at or above the quantum noise level.

As an example, the second term (line 7.6) is important when the atoms are trapped in the intracavity lattice for the premeasurement and then released to into an optical dipole trap for the final measurement. An atom in the optical lattice sees fluctuations with a range of 100% from trial to trial in the standing wave coupling η_{pi}. This leads to classical noise in the premeasurement that is of the same order as quantum projection noise. The quantum (line 7.5) and classical (line 7.6) contribution to $(\Delta\omega_{\mathrm{diff},i})^2$ are approximately equally. The classical noise could, in principle, be removed if we knew every atom's couplings η_{fi} and η_{pi} on each trial, but we do not. Instead, we can only measure the average couplings $\langle\eta_{fi}\rangle$ and $\langle\eta_{pi}\rangle$ by linking a cavity shift, averaged over many trials, to a change in the state population $N_\uparrow$.

The second relevant example that is sensitive to both quantum and classical noise in $\hat{\omega}_{\mathrm{diff}}$ is that of our time-averaged scheme. Atoms will have different initial positions and velocities from trial to trial, leading to classical noise between η_{fi} and η_{pi}. We theoretically predict the contribution to our observed squeezing from this effect in section 7.5.2.4.

The total noise variance $(\Delta\omega_{\mathrm{diff}})^2$ is found by summing the noise contribution from each atom, assuming that they are uncorrelated:

$$(\Delta\omega_{\mathrm{diff}})^2 = \sum_{i=1}^{N}(\Delta\omega_{\mathrm{diff},i})^2. \tag{7.7}$$

Every second order moment (e.g. $\langle\eta_{mi}^2\rangle$) contributing to this sum can in principle be different, but we make the often-valid assumption that the particle labels for every atom are interchangeable. In this case, the trial average $\langle...\rangle$ can equivalently be viewed as an average over all of the atoms in the ensemble on a single trial. In either picture, each term in Eq. 7.7 is equal so that

$$(\Delta\omega_{\mathrm{diff}})^2 = N(\Delta\omega_{\mathrm{diff},i})^2. \tag{7.8}$$

Since we have assumed that expectation values are the same for all atoms i, we will drop the indexes in following expressions such that $\langle \eta_{mi}\eta_{m'i}\rangle \equiv \langle \eta_m\eta_{m'}\rangle$, $\langle \eta_{mi}\rangle \equiv \langle \eta_m\rangle$, and $\langle \hat{\sigma}'^2_{z,i}\rangle \equiv \langle \hat{\sigma}'^2_z\rangle$.

7.5.2.2   Quantum projection noise

To calculate the quantum projection noise (QPN) limit to the noise difference $(\Delta\omega_{\mathrm{diff}})^2$, we can consider the case in Eq. 7.5-7.6 when $W = 0$ and only take the resulting noise from the quantum term of line 7.5,

$$(\Delta\omega_{\mathrm{QPN}})^2 = N\langle \hat{\sigma}'^2_z\rangle\langle \eta^2_f\rangle. \tag{7.9}$$

Equation 7.9 can be used to derive the prediction (given in the Main Text) for projection noise fluctuations in the effective dipole trap when fractionally $(1 - \zeta)$ of the atoms remained trapped in the residual lattice. We assume that the atoms are identically prepared in a pure state with an equal superposition of $|\uparrow\rangle$ and $|\downarrow\rangle$, so that $\langle \hat{\sigma}'^2_{z,i}\rangle = 1/4$. We have set $\gamma = 1/2$, to model our measurements that are sensitive to $N_\uparrow$. For the ζ atoms in the dipole trap, $\langle \eta^2_f\rangle = g^4_0/(4\delta^2_c)$ where g_0 is the Jaynes-Cummings coupling parameter at an anti-node of the cavity. For the $1 - \zeta$ atoms in the residual lattice, $\langle \eta^2_f\rangle = 3g^4_0/(8\delta^2_c)$. Simply adding the projection noise variance of all of the atoms leads to the observed decrease of the projection noise versus ζ,

$$(\Delta\omega_{\mathrm{QPN}})^2(\zeta) = \frac{Ng^4_0}{4\delta^2_c}\left[\frac{1}{4}\zeta + \frac{3}{8}(1 - \zeta)\right]. \tag{7.10}$$

The equation for the QPN level given in the Main Text is more general in that it does not assume the dispersive limit $\delta_c \gg 2\sqrt{N}g_{\mathrm{rms}}$ as we have done here.

7.5.2.3   Optimum spin-noise reduction

The observable spin-noise reduction relative to the quantum noise in the final measurement is given by $R = (\Delta\omega_{\mathrm{diff}})^2/(\Delta\omega_{\mathrm{QPN}})^2$. Here we consider atoms independently prepared in a pure

state with equal superposition of $|\uparrow\rangle$ and $|\downarrow\rangle$), such that $\langle\hat{\sigma}_z'^2\rangle = 1/(1-\gamma)^2$. We then find,

$$R = \frac{\langle\eta_f^2 + W^2\eta_p^2 - 2W\eta_f\eta_p\rangle}{\langle\eta_f^2\rangle} \tag{7.11}$$

$$+ \frac{\gamma'^2}{\langle\eta_f^2\rangle}\left[(\Delta\eta_f)^2 + W^2(\Delta\eta_p)^2 - 2W\,\text{Cov}(\eta_f, \eta_p)\right] \tag{7.12}$$

where we define $\gamma' = \gamma/(1-\gamma)$. As a reminder, $\gamma = \gamma' = 0$ represents a measurement of $N_\uparrow - N_\downarrow$ and $\gamma = 1/2$, $\gamma' = 1$ represents a measurement of only $N_\uparrow$. Similar to Eq. 7.5-7.6, this result possesses a quantum (line 7.11) and classical (line 7.12) contribution. The classical term is given by the variances, or fluctuations of measurement strengths while the quantum term is given by the squared magnitude of the pre and final measurement coupling strengths. Additionally, if $\gamma' = 0$ the classical term vanishes, since the measurement signal will be centered around zero. If $\gamma' = 1$, the two components can be of the same size. This shows that engineering measurements sensitive to $N_\uparrow - N_\downarrow$ can be advantageous to measuring $N_\uparrow$.

The optimum weight factor that minimizes R is

$$W_{\text{opt}} = \frac{\gamma'^2\text{Cov}(\eta_f, \eta_p) + \langle\eta_f\eta_p\rangle}{\langle\eta_p^2\rangle + \gamma'^2(\Delta\eta_p)^2}, \tag{7.13}$$

with optimized noise reduction R_{opt},

$$R_{\text{opt}} = 1 + \frac{\gamma'^2(\Delta\eta_f)^2}{\langle\eta_f^2\rangle} \tag{7.14}$$

$$- \frac{\left[\langle\eta_f\eta_p\rangle + \gamma'^2\text{Cov}(\eta_f, \eta_p)\right]^2}{\langle\eta_f^2\rangle\langle\eta_p^2\rangle + \gamma'^2\langle\eta_f^2\rangle(\Delta\eta_p)^2}. \tag{7.15}$$

This result is the best noise reduction possible when the final and premeasurement have different coupling strengths. Line 7.14 gives the projection noise and classical noise in the final measurement. Line 7.15 represents the optimum cancellation of the final measurement's noise provided by the optimally weighted premeasurement. In the case that only population differences ($N_\uparrow - N_\downarrow$) are mesured, such that $\gamma' = 0$, R_{opt} simplifies to

$$R_{\text{opt}} = 1 - \frac{\langle\eta_f\eta_p\rangle^2}{\langle\eta_f^2\rangle\langle\eta_p^2\rangle}, \tag{7.16}$$

the ratio of the second order moments of the coupling strengths.

7.5.2.4   Fundamental limits for specific cases

We now apply the previous results to two important cases. First, we show that spin-squeezed states created in an optical lattice with incommensurate coupling to the probe standing wave do not lead to significant noise reduction below the SQL after they are launched into a homogeneous environment such as free space or our time-averaged optical dipole trap. Second, we derive the limit to spin-noise reduction in our time-averaged scheme due to imperfect time averaging of the probe standing wave.

For applications such as atom interferometry, it is interesting to consider the case in which the atoms uniformly couple to the final measurement (homogeneous coupling), but during the premeasurement the atoms are held in an optical lattice that has an incommensurate wavelength with the probe standing wave (inhomogeneous coupling.)

We take the final coupling to be the same for all atoms $\eta_f = g_0^2/2\delta_c$. This represents the case when the final measurement is performed with the atoms moving along the cavity axis such that they perfectly time average away spatially inhomogeneous coupling to the probe standing wave. This will also capture the physics of similar such measurement scenarios including ring cavities, commensurate lattice/probe standing waves and spatially homogeneous fluorescence detection.

In our experiment, the lattice $\lambda_l = 823$ nm and probe $\lambda_p = 780$ nm wavelengths are higly incommensurate. The two standing wave antinodes go from fully aligned to misaligned to fully realigned in roughly 7.5 μm, a much shorter length than the characteristic 1 mm range of lattice sites into which atoms are loaded. To describe this scenario, we take the premeasurement coupling of the ith atom to depend on its fixed position x_i on a single trial as $\eta_{pi} = (g_0^2/\delta_c)\sin^2(\Phi_i)$, where the phase of the coupling is $\Phi_i = 2\pi x_i/\lambda_p$. We further assume that the atoms independently and randomly load into different lattice sites from one trial to the next such that the ith atom uniformly samples coupling phases $\Phi_i = 0$ to 2π from trial to trial. However, we re-emphasize that to model a premeasurement performed with the atoms trapped in the lattice, on a single trial the coupling phase of atom i does not vary in time. One then finds second order moments $\langle\eta_p^2\rangle = 3g_0^4/8\delta_c^2$ and

$\langle \eta_f^2 \rangle = \langle \eta_p \eta_f \rangle = g_0^4/4\delta_c^2 = g_{\text{rms}}^4/\delta_c^2$, and variances $(\Delta \eta_p)^2 = \langle \eta_p^2 \rangle - \langle \eta_p \rangle^2 = g_0^4/8\delta_c^2$, $(\Delta \eta_f)^2 = 0$ and $\text{Cov}(\eta_f, \eta_p) = 0$.

The best achievable spin-noise reduction for this case is $R_{\text{opt}} = 1/3$ (1/2) or -4.8 dB (-3 dB) when we consider the two different cases, $\gamma' = 0$ (1). This shows that squeezed states created by a premeasurement in an incommensurate standing wave lattice [39] cannot provide significant entanglement enhancement for free space sensors. Specifically, this degree of spin-noise reduction is far worse than the $R \approx -18$ dB of spin-noise reduction achieved in experiments in which the atoms are trapped for both the pre and final measurement [68, 39].

This optimal spin-noise reduction is achieved using the optimum weight factor $W_{\text{opt}} = 2/3$ (1/2). For comparison, if the relative weight factor is not optimized, but simply set to $W = 1$, one finds that $R_{\text{opt}} = 1/2$ (1) or -3 dB (0 dB).

For the case $\gamma' = 0$, it is interesting to note that in previous squeezing work with incommensurate standing waves [140, 95, 31, 19, 39], an effective atom number N_{eff} was defined in relationship to the total atom number N as $N_{\text{eff}} = 2N/3 = W_{\text{opt}}N$. The above results provide a nice physical interpretation of this effective atom number. The premeasurement can in principle perfectly measure the spin noise of N_{eff} of the total atoms N, here 2/3 of all the atoms. The spin noise of the N_{eff} atoms can then be perfectly cancelled from the final measurement of N atoms. The remaining spin noise of the "unmeasured" atoms $N - N_{\text{eff}}$, here 1/3 of the total atoms, cannot be canceled at all such that the best achievable spin-noise reduction is $R_{\text{opt}} = (N - N_{\text{eff}})/N = 1/3$.

As another example, consider the case in the Section 7.2, where both the pre and final measurements are performed by time averaging the probe coupling as the ith atom moves along the cavity axis at velocity v_i. The atom moves from anti-node to anti-node of the probe at frequency $f_i = 2v_i/\lambda_p$, a frequency we call the coupling oscillation frequency. The time dependent coupling can then be written as $\eta_{mi}(t) = (g_0^2/\delta_c)\sin^2(\pi f_i t + \phi_{mi})$, where ϕ_{mi} sets the coupling at $t = 0$. We assume both the pre and final measurements last for a time T_{win}, and that the pre and final measurements start at $t = 0$ and T_{diff} ($T_{\text{diff}} \geq T_{\text{win}}$) respectively. We take the projection noise level to be that for a perfectly time-averaged scenario in which each atom moves exactly an integer

number of cycles of the standing wave: $(\Delta\omega_{\mathrm{QPN}})^2 = Ng_0^4/16\delta_c^2$. Under the same assumption, we set the weight factor $W = 1$. The spin-noise reduction, averaging over the normalized thermal velocity distribution of atoms $P(f_i)$, is

$$R = \int_{-\infty}^{\infty} P(f_i) \frac{4\sin^2(\pi f_i T_{\mathrm{diff}})\sin^2(\pi f_i T_{\mathrm{win}})}{f_i^2 \pi^2 T_{\mathrm{win}}^2}\, df_i. \tag{7.17}$$

To gain some insight, consider an example when the atomic distribution $P(f_i)$ is Gaussian with mean f_0 and standard deviation Δf. In the limit that T_{diff}, $T_{\mathrm{win}} \gg 1/\Delta f$ and $f_0 \gg \Delta f$, the terms $\sin^2(\pi f_i T_{\mathrm{diff}})$ and $\sin^2(\pi f_i T_{\mathrm{win}})$ in Eq. 7.17 will oscillate rapidly with f_i and so can be replaced in the integrand by their average $1/2$. The resulting spin-noise reduction is then $R = 1/(\pi N_{\mathrm{osc}})^2$ where $N_{\mathrm{osc}} = f_0 T_{\mathrm{win}}$ is the number of cycles averaged by an atom at coupling oscillation frequency f_0.

We estimate the maximum possible spin-noise reduction expected for the conditions used for spin squeezing in the Section 7.2, for which the above simplifying approximations are not valid. To do this, we keep the full expression in Eq. 7.17, set $T_{\mathrm{diff}} = T_{\mathrm{win}} = 40$ μs, and use the directly measured distribution of coupling oscillation frequencies shown in Fig 3(a) of the main text to obtain an experimentally measured probability distribution $P(f_i)$. We find a limit from imperfect averaging $R \approx -15$ dB. We believe this is one of the primary limits to the observed spin-noise reduction $R = -13.9(6)$ dB. However, we expect that this limit can be improved to beyond 20 dB by allowing the atoms to fall for longer or by using longer measurement windows T_{win}, changes that are difficult to implement with current technical constraints of the experiment but that could be straightforward to implement in the future.

7.5.3   Dephasing from inhomogeneous back-action

In Section 7.2, the atoms are allowed to move along the cavity axis in order to achieve time averaging of the inhomogeneous coupling to the standing wave probe mode. As atoms traverse the probe standing wave, they produce fast oscillations in the measured cavity frequency shift in addition to the desired average pre and final measurement signals that are used to resolve phases

below the standard quantum limit. This power spectrum of the oscillations in the cavity shift is shown in Fig. 7.3 with the spread in frequency components reflecting the thermal spread in atomic velocities. These oscillating signals yield information about the spin state of atoms moving at a particular velocity and therefore must cause some degree of additional quantum collapse or back-action, which may limit the amount of squeezing. A full treatment of this effect is very difficult since it likely moves the total wave function away from the restricted fully symmetric Hilbert space of N dimensions and toward the full 2^N dimensional Hilbert space. However, we attempt to derive an estimate for the scale of the deleterious back-action using a classical back-action model driven by quantum noise on the optical probing field. We estimate that the time-averaging scheme, at worst, only provides an additional squeezing limit near the Heisenberg limit $\Delta\theta_H^2 = 1/N^2$ rad^2. This is far from being a relevant limit for the best current experiments that achieve enhanced phase resolutions of approximately $\Delta\theta^2 \approx 10^4/N^2$ rad^2 with approximately $N = 10^6$ atoms [68, 39].

One explanation of the quantum back-action is that the probe light causes a differential AC Stark shift between the spin states such that $|\uparrow\rangle + |\downarrow\rangle \to |\uparrow\rangle + e^{\imath\psi_i}|\downarrow\rangle$, equivalent to the ith atom's Bloch vector changing its azimuthal angle by ψ_i. Photon shot noise (PSN) of the probing beam causes a noisy, unknown contribution to the phase shift with rms fluctuation $\Delta\psi$ that is equivalent to the observed quantum back-action in the azimuthal angle. The PSN level can be plotted (dotted purple line in Fig. 7.4) in frequency space as a power spectral density of photon number fluctuations in the cavity $S_M = 4M_c/\kappa$ [105], valid for frequencies much less than the cavity linewidth κ, where M_c is the average number of photons in the cavity mode and κ is the cavity linewidth. Stationary atoms sample this PSN in a frequency window centered at zero frequency, with characteristic bandwidth $1/T_{\text{win}}$ (the exact sensitivity function shown in red in Fig. 7.4) However, if an atom moves along the cavity axis, its coupling to the probe field during the premeasurement oscillates as $g_{pi}^2(t) = g_0^2 \sin^2(\pi f_i t + \phi_{pi})$, and it will sample the PSN with a modified transfer function, sensitive at DC (due to the time-averaged component of $g_{pi}^2(t)$) as well as a component oscillating at f_i (shown for two different velocities or f_i in blue in Fig 7.4). In the time domain picture, this is equivalent to the intra-cavity photon number fluctuating on a time scale $1/\kappa$. Atoms at different velocities and

initial positions sample these fluctuations differently. As a reminder, we only consider the back-action of the premeasurement (p) because loss of coherence during or after the final measurement does not affect the desired sensitivity for detecting a phase that is applied between the pre and final measurement.

Given a thermal velocity distribution of atoms, the distribution of coupling oscillation frequencies f_i will be given by a Gaussian probability distribution $P(f_i)$ with standard deviation $2\pi \times \Delta f = 4\pi \sqrt{k_b T_{\text{win}}/(m\lambda_p^2)}$ where k_b is Boltzmann's constant, and m is the mass of ^{87}Rb. The number of sub-ensembles that receive uncorrelated back-action will be of order $N_e \sim \Delta f \times T_{\text{win}}$. If $N_e \gg 1$, the total Bloch vector length will be reduced, leading to a loss of contrast $C = e^{-\Delta\psi^2/2}$. We can write the rms phase shift about the mean due to back-action $\Delta\psi$ as

$$\Delta\psi = \alpha\sqrt{M_r}, \tag{7.18}$$

where M_r is the total number of probe photons reflected from the cavity input mirror during a measurement, assuming a loss-less, single-ended cavity. On resonance, the intra-cavity photon number M_c can be related to M_r by $M_r = M_c(T_{\text{win}}\kappa)/4$. The constant $\alpha = 4g_{\text{rms}}^2/(\kappa\delta_c)$ characterizes the average azimuthal phase shift to an atom's Bloch vector per reflected photon.

Using the Heisenberg uncertainty relation for a collective spin state, $\Delta\theta\Delta\psi \geq 1/N$, the PSN limited spin-noise reduction, ignoring all other noise sources, can be shown to be written

$$R = \frac{1}{\alpha^2 M_r q N}. \tag{7.19}$$

In real experiments, the squeezing is fundamentally limited by contrast loss from free space scattering or diffusion of the Bloch vector due to Raman transitions [32]. However, here we neglect these limits to squeezing and instead focus on the squeezing limit solely due to the contrast loss C from inhomogeneous back-action due to time averaging. In this case, the total squeezing as a function of M_r becomes

$$S = R/C^2 = \frac{e^{\alpha^2 M_r}}{\alpha^2 M_r q N}. \tag{7.20}$$
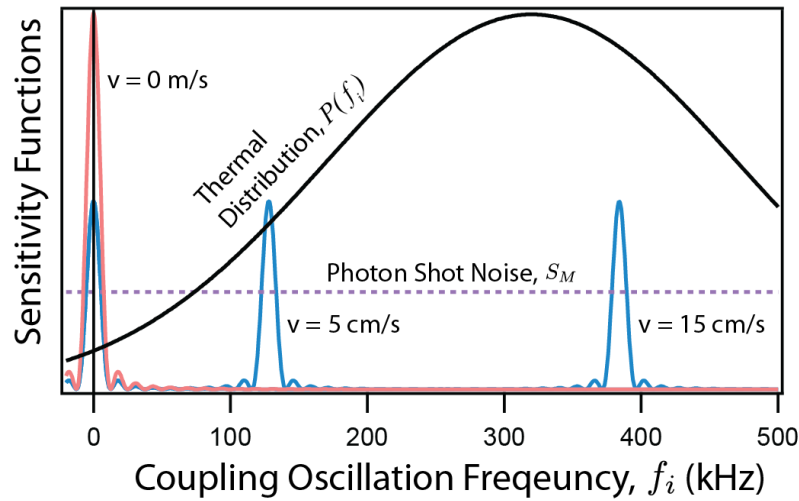
Figure 7.4: Sensitivity of atoms at different velocities to photon shot noise. A moving atom couples to the probe mode with a transfer function (blue) with sensitivity at DC and at a frequency f_i corresponding to its velocity, shown for an atom with velocity 5 cm/s and 15 cm/s. Stationary atoms only couple at DC (red). The distribution of oscillation frequencies is given by the Boltzmann distribution $P(f_i)$ (black). Atoms at different frequencies sample photon shot noise (PSN, purple dash) at different frequencies leading to dephasing that can limit squeezing with time averaging.

which has an optimum value

$$S_{\text{opt}} = \frac{e}{Nq}. \tag{7.21}$$

S_{opt} represents an estimate of the quantum limit to squeezing with our time averaging scheme. However, Equations 20 and 21 show that, for q near 1, the squeezing is only affected by time averaging near the Heisenberg limit.

The physical mechanism and scaling of the squeezing limit (Eq. 21) is quite similar to regular quantum back-action, where every atom receives an identical random phase with an rms magnitude of ψ_{rms} due to photon shot noise in the measurement. In this standard case, since the phase shift is the same for all atoms, the Bloch vector retains its rms extent $J^2 \equiv \langle \hat{J}_x^2 \rangle + \langle \hat{J}_y^2 \rangle \approx N^2/4$. The difference in the time-averaged case is that each subensemble receives a random phase causing a decrease in the collective Bloch vector extent $J^2 < N^2/4$. In this case, the intrinsic phase resolution of the ensemble is lowered, but only when one approaches the Heisenberg limit.

7.5.4   Dephasing from imperfect time averaging

In addition to quantum back-action driven dephasing, there can also be classical dephasing: each atom receives a different average AC Stark shift due to imperfect cycle averaging of the probe standing wave. In realistic experiments, this classical dephasing will usually be much larger than the quantum dephasing described in the previous section.

The phase shift on a single atom can be written, for a single premeasurement window,

$$\psi_i = \int_0^{T_{\text{win}}} dt \frac{g_{pi}^2(t) M_c}{\delta_c} \tag{7.22}$$

where M_c is the average intracavity photon number, taken to be constant for this calculation. To estimate the dephasing due to classical imperfections in the time averaging, we calculate the standard deviation in ψ_i, $\Delta\psi$, over the atomic distribution . The coupling for the ith atom is $g_{pi}^2(t) = g_0^2 \sin^2(\pi f_i t + \phi_{pi})$, with a normalized probability distribution for f_i and ϕ_{pi}, denoted

$P(f_i, \phi_{pi})$.

$$\Delta\psi^2 = \int_0^{2\pi} d\phi_{pi} \int_{-\infty}^{\infty} df_i P(f_i, \phi_{pi})\psi_i^2 - \tag{7.23}$$

$$\left(\int_0^{2\pi} d\phi_{pi} \int_{-\infty}^{\infty} df_i P(f_i, \phi_{pi})\psi_i \right)^2 \tag{7.24}$$

Assuming the phase ϕ_{pi} of the coupling oscillations is random for each atom, the result can be simplified to

$$\Delta\psi^2 = \int_{-\infty}^{\infty} df_i P(f_i) \frac{1}{2} \left(\frac{g_0^2 M_c}{2\pi f_i \delta_c} \right)^2 \sin^2(\pi f_i T_{\text{win}}), \tag{7.25}$$

reducing the contrast after a single premeasurement by $e^{-\Delta\psi^2/2}$. Similar to the uncancelled noise reduction of Eq. 7.17, this result has the interpretation of being due to the phase shift from the final, uncancelled non-integer fraction of an atom's coupling oscillation. However, the result will be slightly modified by the use of a spin-echo pulse for the premeasurement, as in Fig. 7.2 (b), but since the phase of each atom's coupling oscillation changes for each window based on it's velocity, significant spin-echo cancellation of this dephasing is not expected. For our system we estimate that classical dephasing from imperfect time averaging leads to a small contrast loss of less than 1 dB at the optimal squeezing and could be improved to arbitrary levels with better averaging by increasing the number of periods of oscillation in a measurement window while holding the total number of incident photons in the window fixed.

Chapter 8

Conclusion and Future Outlook

Over the course of my graduate studies, my labmates and I have performed a number of experiments to explore how quantum atom-cavity systems can be used to improve precision measurements. I hope that this collection of work will continue to advance the field of quantum science and precision measurement by leading to practical entanglement-enhanced sensors, providing new techniques for building high quality atom-cavity systems, understanding how to generate and understand large amounts of entanglement, and providing new techniques to control precise atomic states.

In general, as atomic sensors become more accurate and precise, we will be able to more sensitively probe the most fundamental principles of the universe, perhaps leading to physics beyond the standard model [61, 156, 7, 175]. Additionally, as atomic experiments become easier to construct and operate, commercialized and miniaturized systems will make their way into industrial applications [80]. Lastly, the ability to control and manipulate quantum systems including entangled states is critically important to the quickly growing field of quantum information science. As we continue to explore and improve the capabilities of atom-cavity systems, I expect advances in quantum communication and quantum simulation to occur as well as advances in precision measurement.

8.1   Future outlook: Spin-squeezed optical lattice clocks

In the near future it may be possible to translate the spin squeezing techniques of this thesis to state-of-the-art optical lattice clocks [115, 66, 121]. Many optical lattice clocks already employ optical cavities to create 1-D optical lattices, and have convenient, dipole-allowed, nearly cycling transitions on which to perform low noise collective probing [121]. An initial proof-of-concept experiment has already been demonstrated in the new strontium experiment in the Thompson lab [121]. Since today's best optical lattice clocks are already significantly limited by quantum noise, and laser-frequency noise from the Dick effect continues to be improved through lower noise lasers [77], and continuous probing schemes [139], spin squeezing has the potential to lead to significant improvements. Increasing atom number to improve quantum noise, on the other hand, may actually be more difficult than generating entanglement since higher atom density leads to unwanted collisional shifts in the clock [71]. However, our technique for generating squeezing fundamentally improves with increasing atom number, so the future of atomic clocks may include both 3D optical lattices for high atom number (small SQL) and very large entanglement enhancements.

8.2   Future outlook: squeezed atom interferometer

Another short term outlook for our work is to demonstrate a proof-of-principle atom interferometer with resolution below the SQL. The work of chapter 7 is a clear first step towards this goal. In particular we could demonstrate a guided interferometer operating inside the optical cavity mode that would not need to perform fluorescence detection, that can be difficult for large ensembles of atoms.

Such an atom interferometer could use Bragg pulses through the cavity in order to drive spin-dependent momentum transfer to the atoms. An experimental diagram that shows the level diagram for the Bragg pulses as well as an experimental sequence is shown below in Fig. 8.1.

In a similar experiment [60], state changing pulses and momentum transfer were accomplished using Raman light pulses. This was possible to do through the cavity since the cavity free spectral
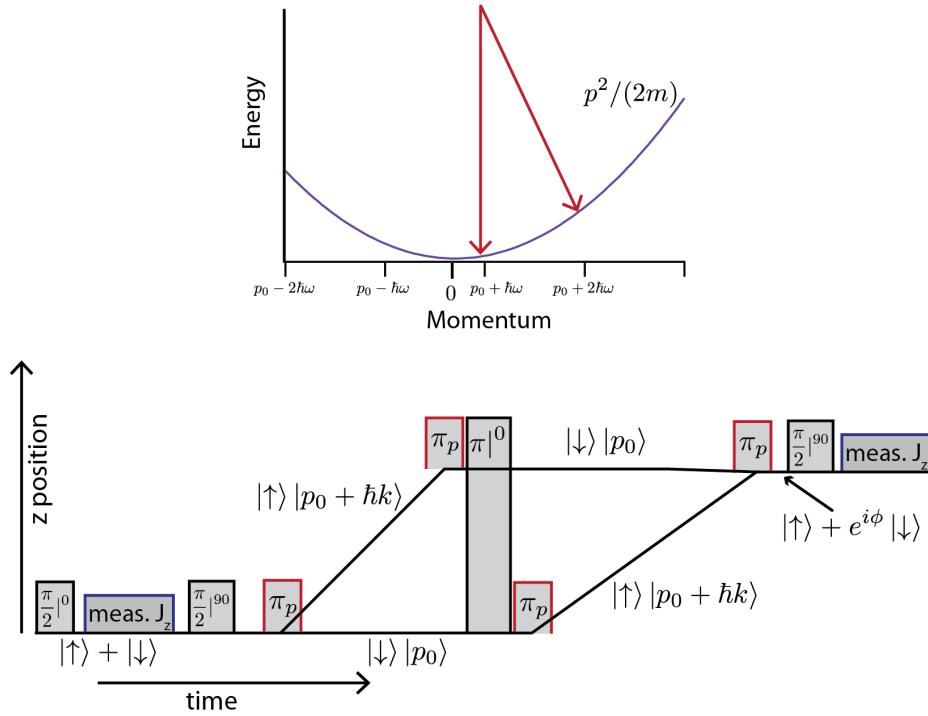
Figure 8.1: a) Momentum transfer diagram for 2-photon Bragg pulses. Two laser beams (red), detuned by the frequency corresponding to 2 quanta of photon momentum change are used to make transitions along the kinetic energy curve of the atom (blue) b) Timing diagram for atom interferometry in a cavity. Atoms' internal states are manipulated by microwave pulses (black and grey) and state-dependent momentum transfers are achieved using 2-photon Bragg pulses (red and grey). The spin-momentum entanglement is used to separate the wave function into different spatial paths leading to a differential phase ϕ, that is subsequently mapped onto the final wave function and read out by a final Ramsey $\pi/2$ pulse. Squeezing is generated by the collective premeasurement of J_z shown with a blue and grey pulse.

range was tuned equal to the hyperfine splitting in the atom. However, in our system, this may not be the case, so I have proposed operating the interferometer with separate microwave spin-changing pulses and Bragg momentum transfers, that can easily be injected into the cavity since the frequency difference between the momentum states is only in the kHz range. An experimental diagram showing a possible atom interferometry sequence and the energy/momentum diagram for the 2-photon Bragg pulses is shown in Fig. 8.1. The interferometer would operate in the z-direction parallel to the cavity axis. Since precise rotations of the Bloch vector have remained challenging in this experiment, operating at lower atom number and higher cavity finesse may be the easiest route to demonstrate a first squeezed interferometer.

As a first proof-of-principle experiment, the evolution time in such a sequence could be very small and one could simply show the ability to generate and read-out momentum-spin entanglement below the standard quantum limit. However, in the future this type of interferometer could be useful in a wide range of atom interferometer applications [9, 135, 141, 131, 61].

8.3   Future outlook: superradiant cooling

Another future outlook for the experiment that is currently being investigated is a collective superradiant cooling mechanism. This phenomenon was recently theoretically introduced in Ref. [177]. While it is certainly unclear whether superradiant cooling will provide a practical or technological advancement to the field of cold atom research, it is clear that this is one of the only collective (could not occur with a single-atom) cooling mechanisms to date and for this reason is of significant scientific value to study.

8.4   Future outlook: Heisenberg limited states

Speculating further for the future, given the recent advances in atom-cavity systems and joint measurement, it is reasonable to believe that we may be able to create maximally-entangled states with Heisenberg-limited phase resolution. Such states could be generated, for example, in a cavity with a single atom cooperativity C much greater than 1. These cavities can be constructed using higher finesse mirrors and/or smaller mode waists. Given our increased ability to engineer high quantum efficiency joint measurements and low technical-noise probing of the optical cavity, this may be possible. However, as the phase resolution on the Bloch sphere continues to improve, state manipulation will continue to be a challenge. For this reason, it may be advisable to first attempt creating maximally entangled states using a smaller atom number, perhaps closer to 10^3 than 10^6.

8.5   Final remarks

Entanglement-enhanced sensors may be among the first practical technologies with no classical analogue. In fact, squeezed states are already being added to a few precision measurements

[57, 121]. As previously mentioned, entangled states are a reasonable avenue toward improving optical lattice atomic clocks and atom interferometers. Additionally, gravitational wave interferometers [57] have demonstrated the use of squeezed light in long baseline interferometry and is expected to implement squeezed light to improve sensitivity of gravitational wave detectors [64].

In addition to using atom-cavity sensors to create spin squeezed states, atom-cavity systems are being explored for other entanglement-enhanced technologies as well. Atoms in cavities can be used to build quantum repeaters to build up quantum networks [35, 29, 146, 15]. They are also being explored for quantum simulation and exploration of highly complex many body physics [117, 82]. They are being used to control optomechanical systems [27], and they are allowing the creation of more exotic entangled states with negative Wigner functions and complex structure [107, 8]

But what comes next? Although it is impossible to definitively predict the future impact of entanglement-enhanced technology, allow me to spend the last paragraph of my thesis in wild speculation. Perhaps one day top down approaches to entanglement generation such as spin squeezing could be used as entanglement resources. This entanglement could be created, manipulated at will, and then shared among large quantum networks. Perhaps large ensembles of atoms in a cavity could be used for analog quantum algorithms, where the probability distribution of the collective spin is manipulated in specific ways to perform algorithms that are difficult for classical computers. Lastly, as has already been proposed, perhaps entangled atomic clocks could be connected in a network [84] to achieve enhanced global timekeeping and synchronization.

I believe the outlook for atom-cavity systems and other quantum technologies is promising, and the most impactful uses of these quantum platforms are yet to come.

Bibliography

[1] BP Abbott, Richard Abbott, TD Abbott, MR Abernathy, Fausto Acernese, Kendall Ackley, Carl Adams, Thomas Adams, Paolo Addesso, RX Adhikari, et al. Observation of gravitational waves from a binary black hole merger. Physical review letters, 116(6):061102, 2016.

[2] David A Anderson, Stephanie A Miller, G Raithel, JA Gordon, ML Butler, and CL Holloway. Optical measurements of strong microwave fields with rydberg atoms in a vapor cell. Physical Review Applied, 5(3):034003, 2016.

[3] A. André, A. S. Sørensen, and M. D. Lukin. Stability of atomic clocks based on entangled atoms. Phys. Rev. Lett., 92:230801, Jun 2004.

[4] J. Appel, P.J. Windpassinger, D. Oblak, U.B. Hoff, N. Kjærgaard, and E.S. Polzik. Mesoscopic atomic entanglement for precision measurements beyond the standard quantum limit. Proc. Natl. Acad. Sci., 106(27):10960–10965, 2009.

[5] T Arpornthip, CA Sackett, and KJ Hughes. Vacuum-pressure measurement using a magneto-optical trap. Physical Review A, 85(3):033420, 2012.

[6] Markus P Baden, Kyle J Arnold, Arne L Grimsmo, Scott Parkins, and Murray D Barrett. Realization of the dicke model using cavity-assisted raman transitions. Physical review letters, 113(2):020408, 2014.

[7] Jacob Baron, Wesley C Campbell, David DeMille, John M Doyle, Gerald Gabrielse, Yulia V Gurevich, Paul W Hess, Nicholas R Hutzler, Emil Kirilov, Ivan Kozyryev, et al. Order of magnitude smaller limit on the electric dipole moment of the electron. Science, 343(6168):269–272, 2014.

[8] Giovanni Barontini, Leander Hohmann, Florian Haas, Jrme Estve, and Jakob Reichel. Deterministic generation of multiparticle entanglement by quantum zeno dynamics. Science, 349(6254):1317–1321, 2015.

[9] B Barrett, A Bertoldi, and P Bouyer. Inertial quantum sensors using light and matter. Physica Scripta, 91(5):053006, 2016.

[10] K. Baumann, C. Guerlin, F. Brennecke, and T. Esslinger. Dicke quantum phase transition with a superfluid gas in an optical cavity. Nature, 464(9):1301, Apr 2010.

[11] Kristian Baumann, Christine Guerlin, Ferdinand Brennecke, and Tilman Esslinger. Dicke quantum phase transition with a superfluid gas in an optical cavity. Nature, 464(7293):1301–1306, April 2010.

[12] N. Behbood, F. Martin Ciurana, G. Colangelo, M. Napolitano, Géza Tóth, R. J. Sewell, and M. W. Mitchell. Generation of macroscopic singlet states in a cold atomic ensemble. Phys. Rev. Lett., 113:093601, Aug 2014.

[13] S Bernon, T Vanderbruggen, R Kohlhaas, A Bertoldi, A Landragin, and P Bouyer. Heterodyne non-demolition measurements on cold atomic samples: towards the preparation of non-classical states for atom interferometry. New Journal of Physics, 13(6):065021, 2011.

[14] Adam T. Black, Hilton W. Chan, and Vladan Vuletić. Observation of collective friction forces due to spatial self-organization of atoms: From rayleigh to bragg scattering. Phys. Rev. Lett., 91:203001, Nov 2003.

[15] Adam T Black, James K Thompson, and Vladan Vuletić. On-demand superradiant conversion of atomic spin gratings into single photons with high efficiency. Physical review letters, 95(13):133601, 2005.

[16] Eric D Black. An introduction to pound–drever–hall laser frequency stabilization. American Journal of Physics, 69(1):79–87, 2001.

[17] B. J. Bloom, T. L. Nicholson, J. R. Williams, S. L. Campbell, M. Bishof, X. Zhang, W. Zhang, S. L. Bromley, and J. Ye. An optical lattice clock with accuracy and stability at the 10^{-18} level. Nature, 506(7486):71–75, February 2014.

[18] J. G. Bohnet, Z. Chen, J. M. Weiner, K. C. Cox, and J. K. Thompson. Relaxation oscillations, stability, and cavity feedback in a superradiant raman laser. Phys. Rev. Lett., 109:253602–253606, Dec 2012.

[19] J. G. Bohnet, K. C Cox, M. A. Norcia, J. M. Weiner, Z. Chen, and J. K. Thompson. Reduced spin measurement back-action for a phase sensitivity ten times beyond the standard quantum limit. Nat. Photon., 8:731–736, July 2014.

[20] Justin G. Bohnet. A Superradiant Laser and Spin Squeezed States: Collective Phenomena in a Rb Cavity QED System for Enhancing Precision Measurements. PhD thesis, JILA and University of Colorado at Boulder, 2014.

[21] Justin G Bohnet, Zilong Chen, Joshua M Weiner, Kevin C Cox, and James K Thompson. Active and passive sensing of collective atomic coherence in a superradiant laser. Physical Review A, 88(1):013826, 2013.

[22] Justin G Bohnet, Zilong Chen, Joshua M Weiner, Kevin C Cox, and James K Thompson. Linear-response theory for superradiant lasers. Physical Review A, 89(1):013806, 2014.

[23] Justin G Bohnet, Zilong Chen, Joshua M Weiner, Dominic Meiser, Murray J Holland, and James K Thompson. A steady-state superradiant laser with less than one intracavity photon. Nature, 484(7392):78–81, 2012.

[24] Justin G Bohnet, Brian C Sawyer, Joseph W Britton, Michael L Wall, Ana Maria Rey, Michael Foss-Feig, and John J Bollinger. Quantum spin dynamics and entanglement generation with hundreds of trapped ions. Science, 352(6291):1297–1301, 2016.

[25] Bohnet, Justin G., Chen, Zilong, Weiner, Joshua M., Cox, Kevin C., Meiser, Dominic, Holland, Murray J., and Thompson, James K. A quasi-continuous superradiant raman laser with ¡ 1 intracavity photon. EPJ Web of Conferences, 57:03003, 2013.

[26] J. Borregaard and A. S. Sørensen. Near-heisenberg-limited atomic clocks in the presence of decoherence. Phys. Rev. Lett., 111:090801, Aug 2013.

[27] Daniel WC Brooks, Thierry Botter, Sydney Schreppler, Thomas P Purdy, Nathan Brahms, and Dan M Stamper-Kurn. Non-classical light generated by quantum-noise-driven cavity optomechanics. Nature, 488(7412):476–480, 2012.

[28] Robert Bücker, Julian Grond, Stephanie Manz, Tarik Berrada, Thomas Betz, Christian Koller, Ulrich Hohenester, Thorsten Schumm, Aurélien Perrin, and Jörg Schmiedmayer. Twin-atom beams. Nat. Phys., 7(8):608–611, 2011.

[29] T Chaneliere, DN Matsukevich, SD Jenkins, S-Y Lan, TAB Kennedy, and A Kuzmich. Storage and retrieval of single photons transmitted between remote quantum memories. Nature, 438(7069):833–836, 2005.

[30] Zilong Chen. Breaking Quantum Limits with Collective Cavity-QED: Generation of Spin Squeezed States via Quantum Non-Demolition Measurements. PhD thesis, JILA and University of Colorado at Boulder, 2013.

[31] Zilong Chen, Justin G. Bohnet, Shannon R. Sankar, Jiayan Dai, and James K. Thompson. Conditional spin squeezing of a large ensemble via the vacuum rabi splitting. Phys. Rev. Lett., 106(13):133601–133604, Mar 2011.

[32] Zilong Chen, Justin G. Bohnet, Joshua M. Weiner, Kevin C. Cox, and James K. Thompson. Cavity-aided nondemolition measurements for atom counting and spin squeezing. Phys. Rev. A, 89:043837, Apr 2014.

[33] Zilong Chen, Justin G. Bohnet, Joshua M. Weiner, and James K. Thompson. General formalism for evaluating the impact of phase noise on bloch vector rotations. Phys. Rev. A, 86:032313, Sep 2012.

[34] Zilong Chen, Justin G. Bohnet, Joshua M. Weiner, and James K. Thompson. A low phase noise microwave source for atomic spin squeezing experiments in 87Rb. Rev. Sci. Instrum., 83(4):044701–044701–5, April 2012.

[35] Kyung Soo Choi, Hui Deng, Julien Laurat, and HJ Kimble. Mapping photonic entanglement into and out of a quantum memory. Nature, 452(7183):67–71, 2008.

[36] Pierre Cladé, Estefania De Mirandes, Malo Cadoret, Saïda Guellati-Khélifa, Catherine Schwob, François Nez, Lucile Julien, and François Biraben. Determination of the fine structure constant based on bloch oscillations of ultracold atoms in a vertical optical lattice. Physical review letters, 96(3):033001, 2006.

[37] K. Colclasure. Mr. babbage, meet mr. lego. IEEE Spectrum, 43(4):26–27, April 2006.

[38] K. C. Cox, J. M. Weiner, G. P. Greve, and J. K. Thompson. Generating entanglement between atomic spins with low-noise probing of an optical cavity. In Frequency Control Symposium the European Frequency and Time Forum (FCS), 2015 Joint Conference of the IEEE International, pages 351–356, April 2015.

[39] Kevin C Cox, Graham P Greve, Joshua M Weiner, and James K Thompson. Deterministic squeezed states with collective measurements and feedback. Physical review letters, 116(9):093602, 2016.

[40] Kevin C Cox, Graham P Greve, Baochen Wu, and James K Thompson. Spatially homogeneous entanglement for matter-wave interferometry created with time-averaged measurements. arXiv preprint arXiv:1608.06234, 2016.

[41] Kevin C. Cox, Matthew A. Norcia, Joshua M. Weiner, Justin G. Bohnet, and James K. Thompson. Reducing collective quantum state rotation errors with reversible dephasing. Applied Physics Letters, 105(26), 2014.

[42] Kevin C Cox, Joshua M Weiner, and James K Thompson. Phase diagram for injection locking a superradiant laser. Physical Review A, 90(5):053845, 2014.

[43] Jean Dalibard and Claude Cohen-Tannoudji. Laser cooling below the doppler limit by polarization gradients: simple theoretical models. JOSA B, 6(11):2023–2045, 1989.

[44] V. DeGiorgio and Marlan O. Scully. Analogy between the laser threshold region and a second-order phase transition. Phys. Rev. A, 2:1170–1177, Oct 1970.

[45] RWP Drever, John L Hall, FV Kowalski, J Hough, GM Ford, AJ Munley, and H Ward. Laser phase and frequency stabilization using an optical resonator. Applied Physics B, 31(2):97–105, 1983.

[46] Albert Einstein, Boris Podolsky, and Nathan Rosen. Can quantum-mechanical description of physical reality be considered complete? Physical review, 47(10):777, 1935.

[47] J. Esteve, C. Gross, A. Weller, S. Giovanazzi, and M. K. Oberthaler. Squeezing and entanglement in a bose-einstein condensate. Nature, 455(7217):1216–1219, October 2008.

[48] Richard P Feynman, Frank L Vernon Jr, and Robert W Hellwarth. Geometrical representation of the schrödinger equation for solving maser problems. Journal of Applied Physics, 28(1):49–52, 1957.

[49] Michael Foss-Feig, Andrew J. Daley, James K. Thompson, and Ana Maria Rey. Steady-state many-body entanglement of hot reactive fermions. Phys. Rev. Lett., 109:230501, Dec 2012.

[50] Crispin Gardiner and Peter Zoller. Quantum noise: a handbook of Markovian and non-Markovian quantum stochastic methods with applications to quantum optics, volume 56. Springer Science & Business Media, 2004.

[51] Marissa Giustina, Marijn AM Versteegh, Sören Wengerowsky, Johannes Handsteiner, Armin Hochrainer, Kevin Phelan, Fabian Steinlechner, Johannes Kofler, Jan-Åke Larsson, Carlos Abellán, et al. Significant-loophole-free test of bells theorem with entangled photons. Physical review letters, 115(25):250401, 2015.

[52] Sarang Gopalakrishnan, Benjamin L. Lev, and Paul M. Goldbart. Frustration and glassiness in spin models with cavity-mediated interactions. Phys. Rev. Lett., 107:277201, Dec 2011.

[53] Sarang Gopalakrishnan, Benjamin L. Lev, and Paul M. Goldbart. Exploring models of associative memory via cavity quantum electrodynamics. Philosophical Magazine, 92(1-3):353–361, 2012.

[54] Peter W. Graham, Jason M. Hogan, Mark A. Kasevich, and Surjeet Rajendran. New method for gravitational wave detection with atomic sensors. Phys. Rev. Lett., 110:171102, Apr 2013.

[55] Joel A. Greenberg, Bonnie L. Schmittberger, and Daniel J. Gauthier. Bunching-induced optical nonlinearity and instability in cold atoms

invited

. Opt. Express, 19(23):22535–22549, Nov 2011.

[56] C. Gross, T. Zibold, E. Nicklas, J. Estve, and M. K. Oberthaler. Nonlinear atom interferometer surpasses classical precision limit. Nature, 464(7292):1165–1169, April 2010.

[57] H. Grote, K. Danzmann, K. L. Dooley, R. Schnabel, J. Slutsky, and H. Vahlbruch. First long-term application of squeezed states of light in a gravitational-wave observatory. Phys. Rev. Lett., 110:181101, May 2013.

[58] V Guarrera, R Szmuk, J Reichel, and P Rosenbusch. Microwave-dressed state-selective potentials for atom interferometry. New Journal of Physics, 17(8):083022, 2015.

[59] JL Hall, L Hollberg, T Baer, and HG Robinson. Optical heterodyne saturation spectroscopy. Applied Physics Letters, 39(9):680–682, 1981.

[60] Paul Hamilton, Matt Jaffe, Justin M Brown, Lothar Maisenbacher, Brian Estey, and Holger Müller. Atom interferometry in an optical cavity. Physical review letters, 114(10):100405, 2015.

[61] Paul Hamilton, Matt Jaffe, Philipp Haslinger, Quinn Simmons, Holger Müller, and Justin Khoury. Atom-interferometry constraints on dark energy. Science, 349(6250):849–851, 2015.

[62] Chris D. Hamley, C. S. Gerving, T. M. Hoang, E. M. Bookjans, and Michael S. Chapman. Spin-nematic squeezed vacuum in a quantum gas. Nat. Phys., 8(4):305–308, February 2012.

[63] Serge Haroche and Jean-Michel Raimond. Exploring the quantum: atoms, cavities, and photons. Oxford university press, 2006.

[64] Gregory M Harry, LIGO Scientific Collaboration, et al. Advanced ligo: the next generation of gravitational wave detectors. Classical and Quantum Gravity, 27(8):084006, 2010.

[65] Bas Hensen, H Bernien, AE Dréau, A Reiserer, N Kalb, MS Blok, J Ruitenberg, RFL Vermeulen, RN Schouten, C Abellán, et al. Loophole-free bell inequality violation using electron spins separated by 1.3 kilometres. Nature, 526(7575):682–686, 2015.

[66] N. Hinkley, J. A. Sherman, N. B. Phillips, M. Schioppo, N. D. Lemke, K. Beloy, M. Pizzocaro, C. W. Oates, and A. D. Ludlow. An atomic clock with 10^{-18} instability. Science, Aug 2013.

[67] M. Hosseini, B.M. Sparkes, G. Campbell, P.K. Lam, and B.C. Buchler. High efficiency coherent optical memory with warm rubidium vapour. Nat. Commun., 2:174, Feb 2011.

[68] O. Hosten, N. J. Engelsen, R. Krishnakumar, and M. A. Kasevich. Measurement noise 100 times lower than the quantum-projection limit using entangled atoms. Nature, 529(7587):505–508, January 2016.

[69] J. Hu, W. Chen, Z. Vendeiro, H. Zhang, and V. Vuletić. Entangled collective-spin states of atomic ensembles under non-uniform atom-light interaction. ArXiv e-prints, October 2015.

[70] Jiazhong Hu, Wenlan Chen, Zachary Vendeiro, Hao Zhang, and Vladan Vuletić. Entangled collective-spin states of atomic ensembles under nonuniform atom-light interaction. Physical Review A, 92(6):063816, 2015.

[71] Tetsuya Ido, Thomas H Loftus, Martin M Boyd, Andrew D Ludlow, Kevin W Holman, and Jun Ye. Precision spectroscopy and density-dependent frequency shifts in ultracold sr. Physical review letters, 94(15):153001, 2005.

[72] Ryotaro Inoue, Shin-Ichi-Ro Tanaka, Ryo Namiki, Takahiro Sagawa, and Yoshiro Takahashi. Unconditional quantum-noise suppression via measurement-based quantum feedback. Phys. Rev. Lett., 110:163602, Apr 2013.

[73] S. Inouye, A. P. Chikkatur, D. M. Stamper-Kurn, J. Stenger, D. E. Pritchard, and W. Ketterle. Superradiant rayleigh scattering from a bose-einstein condensate. Science, 285(5427):571–574, 1999.

[74] WM Itano, JC Bergquist, JJ Bollinger, JM Gilligan, DJ Heinzen, FL Moore, MG Raizen, and DJ Wineland. Quantum projection noise: Population fluctuations in two-level systems. Physical Review A, 47(5):3554, 1993.

[75] G.-B. Jo, Y. Shin, S. Will, T. A. Pasquini, M. Saba, W. Ketterle, D. E. Pritchard, M. Vengalattore, and M. Prentiss. Long phase coherence time and number squeezing of two bose-einstein condensates on an atom chip. Phys. Rev. Lett., 98:030407, Jan 2007.

[76] Hidetoshi Katori. Optical lattice clocks and quantum metrology. Nat. Photon., 5(4):203–210, March 2011.

[77] T Kessler, C Hagemann, C Grebing, T Legero, U Sterr, F Riehle, MJ Martin, L Chen, and J Ye. A sub-40-mhz-linewidth laser based on a silicon single-crystal optical cavity. Nature Photonics, 6(10):687–692, 2012.

[78] Navin Khaneja, Timo Reiss, Cindie Kehlet, Thomas Schulte-Herbrüggen, and Steffen J. Glaser. Optimal control of coupled spin dynamics: design of nmr pulse sequences by gradient ascent algorithms. J. Magn. Reson., Ser A, 172(2):296 – 305, 2005.

[79] Masahiro Kitagawa and Masahito Ueda. Squeezed spin states. Phys. Rev. A, 47:5138–5143, Jun 1993.

[80] J Kitching, EA Donley, S Knappe, M Hummon, AT Dellis, S Kang, Q Li, D Westly, B Roxworthy, VA Aksyuk, et al. Nist on a chip with alkali vapor cells: Initial results. In Precision Electromagnetic Measurements (CPEM 2016), 2016 Conference on, pages 1–2. IEEE, 2016.

[81] Svenja Knappe, Orang Alem, Dong Sheng, and John Kitching. Microfabricated optically-pumped magnetometers for biomagnetic applications. In Journal of Physics: Conference Series, volume 723, page 012055. IOP Publishing, 2016.

[82] Alicia J Kollár, Alexander T Papageorge, Kristian Baumann, Michael A Armen, and Benjamin L Lev. An adjustable-length cavity and bose–einstein condensate apparatus for multimode cavity qed. New Journal of Physics, 17(4):043012, 2015.

[83] MI Kolobov, L Davidovich, E Giacobino, and C Fabre. Role of pumping statistics and dynamics of atomic polarization in quantum fluctuations of laser sources. Physical Review A, 47(2):1431, 1993.

[84] Peter Komar, Eric M Kessler, Michael Bishof, Liang Jiang, Anders S Sørensen, Jun Ye, and Mikhail D Lukin. A quantum network of clocks. Nature Physics, 10(8):582–587, 2014.

[85] IK Kominis, TW Kornack, JC Allred, and MV Romalis. A subfemtotesla multichannel atomic magnetometer. Nature, 422(6932):596–599, 2003.

[86] H. Krauter, D. Salart, C. A. Muschik, J. M. Petersen, Heng Shen, T. Fernholz, and E. S. Polzik. Deterministic quantum teleportation between distant atomic objects. Nat Phys, 9(7):400–404, July 2013.

[87] Hanna Krauter, Christine A. Muschik, Kasper Jensen, Wojciech Wasilewski, Jonas M. Petersen, J. Ignacio Cirac, and Eugene S. Polzik. Entanglement generated by dissipation and steady state entanglement of two macroscopic objects. Phys. Rev. Lett., 107:080503, Aug 2011.

[88] A. Kuzmich, N. P. Bigelow, and L. Mandel. Atomic quantum non-demolition measurements and squeezing. EPL (Europhysics Letters), 42(5):481, 1998.

[89] T. D. Ladd, F. Jelezko, R. Laflamme, Y. Nakamura, C. Monroe, and J. L.s O'Brien. Quantum computers. Nature, 464(7285):45–53, March 2010.

[90] Roy Lang. Injection locking properties of a semiconductor laser. Quantum Electronics, IEEE Journal of, 18(6):976–983, 1982.

[91] Jongmin Lee, Geert Vrijsen, Igor Teper, Onur Hosten, and Mark A Kasevich. Many-atom–cavity qed system with homogeneous atom–cavity coupling. Optics letters, 39(13):4005–4008, 2014.

[92] D. Leibfried, M. D. Barrett, T. Schaetz, J. Britton, J. Chiaverini, W. M. Itano, J. D. Jost, C. Langer, and D. J. Wineland. Toward Heisenberg-limited spectroscopy with multiparticle entangled states. Science, 304(5676):1476–1478, 2004.

[93] D. Leibfried, E. Knill, S. Seidelin, J. Britton, R. B. Blakestad, J. Chiaverini, D. B. Hume, W. M. Itano, J. D. Jost, C. Langer, R. Ozeri, R. Reichle, and D. J. Wineland. Creation of a six-atom /'schrodinger cat/' state. Nature, 438(7068):639–642, Dec 2005.

[94] U. Leonhardt. Measuring the Quantum State of Light. Cambridge Studies in Modern Optics. Cambridge University Press, 1997.

[95] Ian D. Leroux, Monika H. Schleier-Smith, and Vladan Vuletić. Implementation of cavity squeezing of a collective atomic spin. Phys. Rev. Lett., 104:073602, Feb 2010.

[96] Ian D. Leroux, Monika H. Schleier-Smith, and Vladan Vuletić. Orientation-dependent entanglement lifetime in a squeezed atomic clock. Phys. Rev. Lett., 104:250801, Jun 2010.

[97] Igor Lesanovsky and Wolf von Klitzing. Time-averaged adiabatic potentials: Versatile matter-wave guides and atom traps. Phys. Rev. Lett., 99:083001, Aug 2007.

[98] Jr-Shin Li and Navin Khaneja. Control of inhomogeneous quantum ensembles. Phys. Rev. A, 73:030302, Mar 2006.

[99] Wei Li, Ning Hua Zhu, Li Xian Wang, Jian Hong Ke, Shuo Fu Chen, Xiao Qiong Qi, Bang Hong Zhang, and Liang Xie. Frequency-pushing effect in single-mode diode laser subject to external dual-beam injection. Quantum Electronics, IEEE Journal of, 46(5):796–803, May 2010.

[100] Qian Lin, Mackenzie A Van Camp, Hao Zhang, Branislav Jelenković, and Vladan Vuletić. Long-external-cavity distributed bragg reflector laser with subkilohertz intrinsic linewidth. Optics letters, 37(11):1989–1991, 2012.

[101] B Lücke, M Scherer, J Kruse, L Pezzé, F Deuretzbacher, P Hyllus, O Topic, J Peise, W Ertmer, J Arlt, L Santos, A Smerzi, and C Klempt. Twin matter waves for interferometry beyond the classical limit. Science, 334(6057):773–6, November 2011.

[102] Bernd Lücke, Jan Peise, Giuseppe Vitagliano, Jan Arlt, Luis Santos, Géza Tóth, and Carsten Klempt. Detecting multiparticle entanglement of dicke states. Phys. Rev. Lett., 112:155304, Apr 2014.

[103] Bernd Lücke, Jan Peise, Giuseppe Vitagliano, Jan Arlt, Luis Santos, Géza Tóth, and Carsten Klempt. Detecting multiparticle entanglement of dicke states. Phys. Rev. Lett., 112:155304, Apr 2014.

[104] Gonzalo Manzano, Fernando Galve, Gian Luca Giorgi, Emilio Hernndez-Garca, and Roberta Zambrini. Synchronization, quantum correlations and entanglement in oscillator networks. Sci. Rep., 3:–, March 2013.

[105] Florian Marquardt, Joe P. Chen, A. A. Clerk, and S. M. Girvin. Quantum theory of cavity-assisted sideband cooling of mechanical motion. Phys. Rev. Lett., 99:093902, Aug 2007.

[106] M. J. Martin, D. Meiser, J. W. Thomsen, Jun Ye, and M. J. Holland. Extreme nonlinear response of ultranarrow optical transitions in cavity qed for laser stabilization. Phys. Rev. A, 84:063813, Dec 2011.

[107] Robert McConnell, Hao Zhang, Jiazhong Hu, Senka Cuk, and Vladan Vuletic. Entanglement with negative wigner function of almost 3,000 atoms heralded by one photon. Nature, 519(7544):439–442, March 2015.

[108] D. Meiser and M. J. Holland. Steady-state superradiance with alkaline-earth-metal atoms. Phys. Rev. A, 81(3):033847, Mar 2010.

[109] D. Meiser, Jun Ye, D. R. Carlson, and M. J. Holland. Prospects for a millihertz-linewidth laser. Phys. Rev. Lett., 102(16):163601–163604, Apr 2009.

[110] H.J. Metcalf and P. van der Straten. Laser Cooling and Trapping. Graduate Texts in Contemporary Physics. Springer New York, 2001.

[111] V. Meyer, M. A. Rowe, D. Kielpinski, C. A. Sackett, W. M. Itano, C. Monroe, and D. J. Wineland. Experimental demonstration of entanglement-enhanced rotation angle estimation using trapped ions. Phys. Rev. Lett., 86:5870–5873, Jun 2001.

[112] Finn Mogensen, Henning Olesen, and Gunnar Jacobsen. Locking conditions and stability properties for a semiconductor laser with external light injection. Quantum Electronics, IEEE Journal of, 21(7):784–793, 1985.

[113] Thomas Monz, Philipp Schindler, Julio T. Barreiro, Michael Chwalla, Daniel Nigg, William A. Coish, Maximilian Harlander, Wolfgang Hänsel, Markus Hennrich, and Rainer Blatt. 14-qubit entanglement: Creation and coherence. Phys. Rev. Lett., 106:130506, Mar 2011.

[114] W. Muessel, H. Strobel, D. Linnemann, D. B. Hume, and M. K. Oberthaler. Scalable spin squeezing for quantum-enhanced magnetometry with bose-einstein condensates. Phys. Rev. Lett., 113:103004, Sep 2014.

[115] TL Nicholson, SL Campbell, RB Hutson, GE Marti, BJ Bloom, RL McNally, W Zhang, MD Barrett, MS Safronova, GF Strouse, et al. Systematic evaluation of an atomic clock at 2 [times] 10-18 total uncertainty. Nature communications, 6, 2015.

[116] D. Nigg, M. Müller, E. A. Martinez, P. Schindler, M. Hennrich, T. Monz, M. A. Martin-Delgado, and R. Blatt. Quantum computations on a topologically encoded qubit. Science, 345(6194):302–305, 2014.

[117] Jia Ningyuan, Alexandros Georgakopoulos, Albert Ryou, Nathan Schine, Ariel Sommer, and Jonathan Simon. Observation and characterization of cavity rydberg polaritons. Physical Review A, 93(4):041802, 2016.

[118] Atsushi Noguchi, Kenji Toyoda, and Shinji Urabe. Generation of Dicke states with phonon-mediated multilevel stimulated raman adiabatic passage. Phys. Rev. Lett., 109:260502, Dec 2012.

[119] M. A. Norcia and J. K. Thompson. Strong Coupling on a Forbidden Transition in Strontium and Nondestructive Atom Counting. ArXiv e-prints, June 2015.

[120] Matthew A Norcia and James K Thompson. Cold-strontium laser in the superradiant crossover regime. Physical Review X, 6(1):011025, 2016.

[121] Matthew A Norcia and James K Thompson. Strong coupling on a forbidden transition in strontium and nondestructive atom counting. Physical Review A, 93(2):023804, 2016.

[122] Matthew A Norcia, Matthew N Winchester, Julia RK Cline, and James K Thompson. Superradiance on the millihertz linewidth strontium clock transition. arXiv preprint arXiv:1603.05671, 2016.

[123] G. L. Oppo, A. Politi, G. L. Lippi, and F. T. Arecchi. Frequency pushing in lasers with injected signal. Phys. Rev. A, 34:4000–4007, Nov 1986.

[124] A. Pikovsky, M. Rosenblum, and J. Kurths. Synchronization: A Universal Concept in Nonlinear Sciences. University Press, 2003.

[125] Arkaday Pikovsky, Michael Rosenblum, and Jaergen Kurths. Phase synchronization in regular and chaotic systems. International Journal of Bifurcation and Chaos, 10(10):2291–2305, 2000.

[126] John Preskill. Quantum computing and the entanglement frontier. arXiv preprint arXiv:1203.5813, 2012.

[127] I. I. Rabi, S. Millman, P. Kusch, and J. R. Zacharias. The molecular beam resonance method for measuring nuclear magnetic moments. the magnetic moments of $_3Li^6$, $_3Li^7$ and $_9F^{19}$. Phys. Rev., 55:526–535, Mar 1939.

[128] Worawarong Rakreungdet, Jae Hoon Lee, Kim Fook Lee, Brian E. Mischuck, Enrique Montano, and Poul S. Jessen. Accurate microwave control and real-time diagnostics of neutral-atom qubits. Phys. Rev. A, 79:022316, Feb 2009.

[129] Norman F. Ramsey. A molecular beam resonance method with separated oscillating fields. Phys. Rev., 78:695–699, Jun 1950.

[130] Florentin Reiter, L. Tornberg, Göran Johansson, and Anders S. Sørensen. Steady-state entanglement of two superconducting qubits engineered by dissipation. Phys. Rev. A, 88:032317, Sep 2013.

[131] C. Jess Riedel. Direct detection of classically undetectable dark matter through quantum decoherence. Phys. Rev. D, 88:116005, Dec 2013.

[132] Max F. Riedel, Pascal Böhi, Yun Li, Theodor W. Hänsch, Alice Sinatra, and Philipp Treutlein. Atom-chip-based generation of entanglement for quantum metrology. Nature, 464(7292):1170–1173, April 2010.

[133] D. Riste, M. Dukalski, C. A. Watson, G. de Lange, M. J. Tiggelman, Ya. M. Blanter, K. W. Lehnert, R. N. Schouten, and L. DiCarlo. Deterministic entanglement of superconducting qubits by parity measurement and feedback. Nature, 502(7471):350–354, October 2013.

[134] N. Roch, M. E. Schwartz, F. Motzoi, C. Macklin, R. Vijay, A. W. Eddins, A. N. Korotkov, K. B. Whaley, M. Sarovar, and I. Siddiqi. Observation of measurement-induced entanglement and quantum trajectories of remote superconducting qubits. Phys. Rev. Lett., 112:170501, Apr 2014.

[135] G. Rosi, F. Sorrentino, L. Cacciapuoti, M. Prevedelli, and G. M. Tino. Precision measurement of the newtonian gravitational constant using cold atoms. Nature, 510(7506):518–521, June 2014.

[136] C. A. Sackett, D. Kielpinski, B. E. King, , C. Langer, V. Meyer, C. J. Myatt, M. Rowe, Q. A. Turchette, W. M. Itano, D. J. Wineland, and C. Monroe. Experimental entanglement of four particles. Nature, 404:256, March 2000.

[137] CA Sackett, David Kielpinski, BE King, C Langer, V Meyer, CJ Myatt, M Rowe, QA Turchette, WM Itano, DJ Wineland, et al. Experimental entanglement of four particles. Nature, 404(6775):256–259, 2000.

[138] A. L. Schawlow and C. H. Townes. Infrared and optical masers. Phys. Rev., 112:1940–1949, Dec 1958.

[139] M Schioppo, RC Brown, WF McGrew, N Hinkley, RJ Fasano, K Beloy, TH Yoon, G Milani, D Nicolodi, JA Sherman, et al. Ultra-stable optical clock with two cold-atom ensembles. arXiv preprint arXiv:1607.06867, 2016.

[140] Monika H. Schleier-Smith, Ian D. Leroux, and Vladan Vuletić. States of an ensemble of two-level atoms with reduced quantum uncertainty. Phys. Rev. Lett., 104:073604, Feb 2010.

[141] D. Schlippert, J. Hartwig, H. Albers, L. L. Richardson, C. Schubert, A. Roura, W. P. Schleich, W. Ertmer, and E. M. Rasel. Quantum test of the universality of free fall. Phys. Rev. Lett., 112:203002, May 2014.

[142] R. J. Sewell, M. Koschorreck, M. Napolitano, B. Dubost, N. Behbood, and M. W. Mitchell. Magnetic sensitivity beyond the projection noise limit by spin squeezing. Phys. Rev. Lett., 109:253605, Dec 2012.

[143] Lynden K Shalm, Evan Meyer-Scott, Bradley G Christensen, Peter Bierhorst, Michael A Wayne, Martin J Stevens, Thomas Gerrits, Scott Glancy, Deny R Hamel, Michael S Allman, et al. Strong loophole-free test of local realism. Physical review letters, 115(25):250402, 2015.

[144] Jacob F. Sherson, Hanna Krauter, Rasmus K. Olsson, Brian Julsgaard, Klemens Hammerer, Ignacio Cirac, and Eugene S. Polzik. Quantum teleportation between light and matter. Nature, 443(7111):557–560, October 2006.

[145] Anthony E. Siegman. Lasers. University Science Books, Sausalito, CA, first edition edition, May 1986.

[146] Jonathan Simon, Haruka Tanji, James K Thompson, and Vladan Vuletić. Interfacing collective atomic excitations and single photons. Physical review letters, 98(18):183601, 2007.

[147] TB Simpson, JM Liu, KF Huang, and K Tai. Nonlinear dynamics induced by external optical injection in semiconductor lasers. Quantum and Semiclassical Optics: Journal of the European Optical Society Part B, 9(5):765, 1997.

[148] S. Slama, S. Bux, G. Krenz, C. Zimmermann, and Ph. W. Courteille. Superradiant rayleigh scattering and collective atomic recoil lasing in a ring cavity. Phys. Rev. Lett., 98:053603, Feb 2007.

[149] A. Sørensen, L.-M. Duan, J. I. Cirac, and P. Zoller. Many-particle entanglement with bose-einstein condensates. Nature, 409(6816):63–66, January 2001.

[150] Anders S. Sørensen and Klaus Mølmer. Entanglement and extreme spin squeezing. Phys. Rev. Lett., 86:4431–4434, May 2001.

[151] Matthias Steffen and Roger H. Koch. Shaped pulses for quantum computing. Phys. Rev. A, 75:062326, Jun 2007.

[152] Philipp Strack and Subir Sachdev. Dicke quantum spin glass of atoms and photons. Phys. Rev. Lett., 107:277202, Dec 2011.

[153] Barbara M Terhal. Quantum error correction for quantum memories. Reviews of Modern Physics, 87(2):307, 2015.

[154] L K Thomsen, S Mancini, and H M Wiseman. Continuous quantum nondemolition feedback and unconditional atomic spin squeezing. J. Phys. B: At., Mol. Opt. Phys., 35(23):4937, 2002.

[155] L. K. Thomsen, S. Mancini, and H. M. Wiseman. Spin squeezing via quantum feedback. Phys. Rev. A, 65:061801, Jun 2002.

[156] GM Tino, L Cacciapuoti, K Bongs, Ch J Bordé, P Bouyer, H Dittus, W Ertmer, A Görlitz, M Inguscio, A Landragin, et al. Atom interferometers and optical atomic clocks: New quantum sensors for fundamental physics experiments in space. Nuclear Physics B-Proceedings Supplements, 166:159–165, 2007.

[157] Boyan T. Torosov and Nikolay V. Vitanov. Smooth composite pulses for high-fidelity quantum information processing. Phys. Rev. A, 83:053420, May 2011.

[158] Emanuele G. Dalla Torre, Sebastian Diehl, Mikhail D. Lukin, Subir Sachdev, and Philipp Strack. Keldysh approach for nonequilibrium phase transitions in quantum optics: Beyond the dicke model in optical cavities. Phys. Rev. A, 87:023831, Feb 2013.

[159] QA Turchette, CS Wood, BE King, CJ Myatt, D Leibfried, WM Itano, C Monroe, and DJ Wineland. Deterministic entanglement of two trapped ions. Physical Review Letters, 81(17):3631, 1998.

[160] R. Tycko, H. M. Cho, E. Schneider, and A. Pines. Composite pulses without phase distortion. J. Magn. Reson., Ser A, 61(1):90 – 101, 1985.

[161] Götz S. Uhrig. Keeping a quantum bit alive by optimized π-pulse sequences. Phys. Rev. Lett., 98:100504, Mar 2007.

[162] Ichiro Ushijima, Masao Takamoto, Manoj Das, Takuya Ohkubo, and Hidetoshi Katori. Cryogenic optical lattice clocks. Nature Photonics, 9(3):185–189, 2015.

[163] Henning Vahlbruch, Moritz Mehmet, Simon Chelkowski, Boris Hage, Alexander Franzen, Nico Lastzka, Stefan Goßler, Karsten Danzmann, and Roman Schnabel. Observation of squeezed light with 10-db quantum-noise reduction. Phys. Rev. Lett., 100:033602, Jan 2008.

[164] Georgios Vasilakis, Heng Shen, Kasper Jensen, Misha Balabas, Daniel Salart, Bing Chen, and Eugene Simon Polzik. Generation of a squeezed state of an oscillator by stroboscopic back-action-evading measurement. Nature Physics, 11(5):389–392, 2015.

[165] Brian Vlastakis, Gerhard Kirchmair, Zaki Leghtas, Simon E. Nigg, Luigi Frunzio, S. M. Girvin, Mazyar Mirrahimi, M. H. Devoret, and R. J. Schoelkopf. Deterministically encoding quantum information using 100-photon schrdinger cat states. Science, 342(6158):607–610, 2013.

[166] Vladan Vuletić, James K. Thompson, Adam T. Black, and Jonathan Simon. External-feedback laser cooling of molecular gases. Phys. Rev. A, 75:051405, May 2007.

[167] Stefan Walter, Andreas Nunnenkamp, and Christoph Bruder. Quantum synchronization of a driven self-sustained oscillator. Phys. Rev. Lett., 112:094102, Mar 2014.

[168] Ying-Ju Wang, Dana Z. Anderson, Victor M. Bright, Eric A. Cornell, Quentin Diot, Tetsuo Kishimoto, Mara Prentiss, R. A. Saravanan, Stephen R. Segal, and Saijun Wu. Atom michelson interferometer on a chip using a bose-einstein condensate. Phys. Rev. Lett., 94:090405, Mar 2005.

[169] W. Wasilewski, K. Jensen, H. Krauter, J. J. Renema, M. V. Balabas, and E. S. Polzik. Quantum noise limited and entanglement-assisted magnetometry. Phys. Rev. Lett., 104:133601, Mar 2010.

[170] Joshua M. Weiner. Synchronization and Sensing with Steady State Superradiance and Spin Squeezing. PhD thesis, JILA and University of Colorado at Boulder, 2015.

[171] Joshua M Weiner, Kevin C Cox, Justin G Bohnet, Zilong Chen, and James K Thompson. Superradiant raman laser magnetometer. Applied Physics Letters, 101(26):261107, 2012.

[172] S. Wimperis. Broadband, narrowband, and passband composite pulses for use in advanced nmr experiments. J. Magn. Reson., Ser A, 109(2):221 – 231, 1994.

[173] D. J. Wineland, J. J. Bollinger, W. M. Itano, and D. J. Heinzen. Squeezed atomic states and projection noise in spectroscopy. Phys. Rev. A, 50:67–88, Jul 1994.

[174] D. J. Wineland, J. J. Bollinger, W. M. Itano, F. L. Moore, and D. J. Heinzen. Spin squeezing and reduced quantum noise in spectroscopy. Phys. Rev. A, 46(11):R6797–R6800, 1992.

[175] CS Wood, SC Bennett, Donghyun Cho, BP Masterson, JL Roberts, CE Tanner, and CE Wieman. Measurement of parity nonconservation and an anapole moment in cesium. Science, 275(5307):1759–1763, 1997.

[176] Saijun Wu, Edward Su, and Mara Prentiss. Demonstration of an area-enclosing guided-atom interferometer for rotation sensing. Phys. Rev. Lett., 99:173201, Oct 2007.

[177] Minghui Xu, Simon B Jäger, S Schütz, J Cooper, Giovanna Morigi, and MJ Holland. Supercooling of atoms in an optical resonator. Physical review letters, 116(15):153002, 2016.

[178] Minghui Xu, DA Tieri, EC Fine, James K Thompson, and MJ Holland. Synchronization of two ensembles of atoms. Physical review letters, 113(15):154101, 2014.

[179] Bo Yan, Steven A. Moses, Bryce Gadway, Jacob P. Covey, Kaden R. A. Hazzard, Ana Maria Rey, Deborah S. Jin, and Jun Ye. Observation of dipolar spin-exchange interactions with lattice-confined polar molecules. Nature, 501:521, Sep 2013.

[180] Hao Zhang, Robert McConnell, Senka Ćuk, Qian Lin, Monika H. Schleier-Smith, Ian D. Leroux, and Vladan Vuletić. Collective state measurement of mesoscopic ensembles with single-atom resolution. Phys. Rev. Lett., 109:133603, Sep 2012.

Appendix A

Homodyne and Heterodyne Detection

For all of the experiments in this thesis, we wish to make phase or frequency measurements of an optical field used to probe the optical cavity or emitted from the atoms inside the optical cavity. To do this, we overlap the emitted field with another local oscillator (LO) beam used as a phase reference, and perform optical interferometry. There are generally two possible ways to do this. The first is for the measured field and LO to have the same frequency and measure the direct DC interference. This is known as homodyne detection. The second option is to detune the measured beam from the LO and observe oscillations in the interference between them, allowing a simultaneous measurement of both the laser's amplitudes and relative phases. This is known as heterodyne detection.

We have used both heterodyne and homodyne detection to measure cavity fields for various experiments. Heterodyne is often considered easier since it does not require as strong phase stability between the probe and LO, there is an infinite dynamic range for phase excursions, and the signals lie away from DC where technical 1/f noise sources can be troublesome. On the other hand, heterodyne detection also leads to a sub-optimal measurement of the phase of the emitted light since half the time the heterodyne effectively measures the phase quadrature and half the time the amplitude of the emitted light. This leads to an effective loss of 50% of the emitted information.

In recent experiments (Chapters 6,7), a homodyne measurement was used to perform an entanglement-generating joint measurement of atoms in a cavity as well as to calibrate the power in the probing beam. For this reason, and since the factors of two that determine the size of these

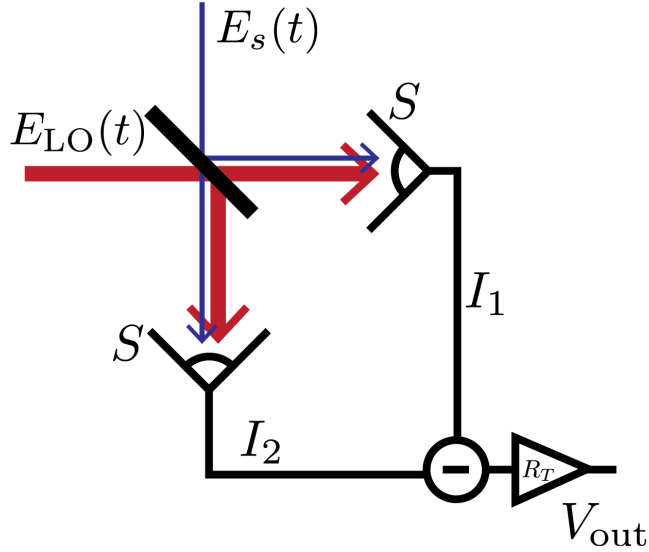interference signals have caused difficulty in the past, I will derive the size of homodyne signals here.

Figure A.1: Homodyne detection. A signal field $E_s(t)$ (blue) and strong local oscillator field $E_{LO}(t)$ (red) are overlapped on a 50/50 beamsplitter and measured on a detector with sensitivity S [Amps/Watt]. The signals are then subtracted and sent through a transimpedance amplifier with gain R_t [Ohms]. The output voltage, V_{out} can be used either as a measurement of the signal amplitude or signal phase, depending on the phase ϕ between the signal and LO.

As shown in Fig. A.1, the signal and LO beam are overlapped on a 50/50 beamsplitter and detected on a balanced homodyne detector. The signal beam and LO beam can be written, for this analysis, as classical electric fields with peak amplitudes E_s and E_{LO}.

$$E_s(t) = E_s \sin(\omega t + \phi) \tag{A.1}$$

$$E_{LO}(t) = E_{LO} \sin(\omega t) \tag{A.2}$$

The photocurrents $I_1(t)$ and $I_2(t)$ that would be generated on an infinite bandwidth detector on each arm are given by a constant ϵ^2 which converts squared electric fields into photo-current.

$$I_1(t) = \frac{\epsilon^2}{2} \left[E_s^2 \sin^2(\omega t + \phi) + E_{LO}^2 \sin^2(\omega t) + 2E_{LO}E_s \sin(\omega t + \phi) \sin(\omega t) \right] \tag{A.3}$$

$$I_2(t) = \frac{\epsilon^2}{2} \left[E_s^2 \sin^2(\omega t + \phi) + E_{LO}^2 \sin^2(\omega t) - 2E_{LO}E_s \sin(\omega t + \phi) \sin(\omega t) \right] \tag{A.4}$$

The final terms in $I_1(t)$ and $I_2(t)$ must differ by a sign due to energy conservation requirements in the beamsplitter.

The products of oscillating signals in $I_1(t)$ and $I_2(t)$ can be rewritten in terms of sums and differences.

$$I_1(t) = \frac{\epsilon^2}{2}\left[E_s^2 \sin^2(\omega t + \phi) + E_{LO}^2 \sin^2(\omega t) + E_{LO}E_s \cos(\phi) - E_{LO}E_s \cos(2\omega + \phi)\right] \tag{A.5}$$

$$I_2(t) = \frac{\epsilon^2}{2}\left[E_s^2 \sin^2(\omega t + \phi) + E_{LO}^2 \sin^2(\omega t) - E_{LO}E_s \cos(\phi) + E_{LO}E_s \cos(2\omega + \phi)\right]. \tag{A.6}$$

Since photodetectors do not have the bandwidth to directly measure the optical frequency of the beam ω, the measured difference of the two photocurrents $\bar{I}_{\text{diff}}$ also includes a time average of the oscillations, signified as an over bar. The cos terms which oscillate rapidly at freqeuency ω will quickly average to zero, and the $\sin^2$ terms will simple become DC offsets which cancel in the difference. The result of the time average is,

$$\bar{I}_{\text{diff}} = \overline{(I_1 - I_2)} = \epsilon^2 E_s E_{LO} \cos\phi. \tag{A.7}$$

The only term that remains from $I_1(t)$ and $I_2(t)$ is the DC interference between the signal and LO. Additionally, the conversion constant ϵ can be re-written in terms of the sensitivity of the photodiode when the electric fields are re-written in terms of the average optical power in the signal and LO beams P_s and P_{LO} and the photodetector's sensitivity S in units of Amps per Watt. This relation can be easily derived by considering the effect of a single beam (here labeled "a") incident on a single photodetector using $\bar{I}_a = SP_a = \epsilon^2 E_a^2/2$. The final homodyne signal, in terms of measured quantities V_{out}, R_t, S, and optical powers, is found by substituting E_s and E_{LO} by their average powers P_s and P_{LO} as measured on a DC photodiode and multiplying by the transimpedance gain R_t.

$$V_{\text{out}} = R_t \bar{I}_{\text{diff}} = 2R_t S \sqrt{P_s P_{LO}} \cos(\phi). \tag{A.8}$$

When performing heterodyne detection, one finds the exact same solution where ϕ now becomes a function of time $\phi \to \phi(t)$.

Appendix B

Feedback Loops

For the optical and electrical elements of our experiment to work in concert requires a number of feedback loops used for laser frequency, amplitude, and temperature stabilization, as well as dynamic control and synchronization of the optical and rf signals required in an experimental sequence. Inserting PID (Proportional-Integral-Differential) feedback loops has become a general purpose tool in the lab. In this section, I will review a simplified feedback theory and useful information about the standard loop filter circuits most commonly used for feedback in our lab.
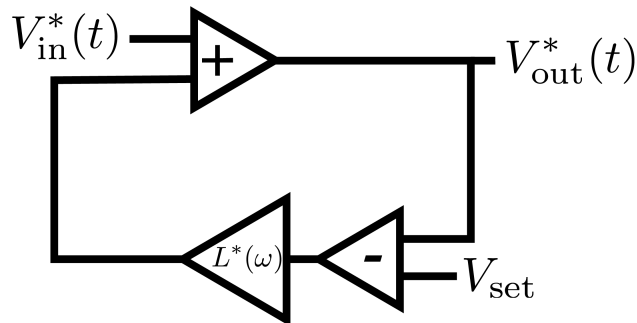
B.1   Feedback model

Figure B.1: Simple system with feedback. In order to stabilize a noisy input voltage $V_{\text{in}}^*(t)$, one can compare the voltage to a set point, V_{set} and apply feedback by multiplying the difference by large gain $L^*(\omega)$.

A simple steady-state model of feedback can elucidate the most important results for design-

ing feedback loops. Assume there is an AC signal $V_{\text{in}}^*(t)$ represented in the complex plane that we wish to stabilize. I assume that this signal, presumed to be a voltage, is a constant oscillation with a complex amplitude V_{in}^*, $V_{\text{in}}^*(t) = V_{\text{in}}^* e^{i\omega t}$. In order to stabilize $V_{\text{in}}^*(t)$ to a constant real value V_{set}, we apply feedback through a loop filter with a complex, frequency dependent gain labeled, $L^*(\omega)$.

The steady state output voltage V_{out}^* can be found by solving the recursive equation for the feedback loop,

$$V_{\text{out}}^* = V_{\text{in}}^*(t) + (V_{\text{out}}^* - V_{\text{set}}) \times L^*(\omega). \tag{B.1}$$

The equation has a solution,

$$V_{\text{out}}^* = \frac{V_{\text{in}}^*(t) - V_{\text{set}} L^*(\omega)}{1 - L^*(\omega)} \tag{B.2}$$

If $L^*(\omega)$ is very large, $V_{\text{out}}^* \to V_{\text{set}}$ as desired; the feedback successfully suppresses the noise at frequency ω. However, in reality, the system will be subjected to a continuum of noise at all frequencies ω. For the feedback to work properly, therefore, the system must be well behaved at all ω. In particular, the most important point is at the unity gain frequency ω_1 such that $|L^*(\omega_1)| \equiv 1$. The feedback will actually amplify noise near frequencies ω_1 unless $L^*(\omega_1)$ is negative or imaginary, that is, unless $\text{Re}[L^*(\omega_1)] < 0$. Therefore, the optimization of a feedback loop is this: maximize the gain L and feedback bandwdith ω_1 while still making sure that the phase shifts around ω_1 (called loss of phase margin) are sufficiently small to avoid positive feedback at the unity gain frequency. Positive feedback begins to occur when the loss of phase margin surpasses $90°$. Often, phase losses slightly larger than $90°$ are allowable, but lead to a small amount of noise gain (and therefore a visible noise bump in the spectrum) near the unity gain frequency.

B.2 Loop filters

Loop filters are built to allow a large amount of tunability in the amplitude and bandwidth of $L^*(\omega)$. PID loop filters have a constant, integral $L^*(\omega) \propto 1/\omega$, and differential gain term $L^*(\omega) \propto \omega$ that allow one to craft the most optimal feedback. Importantly, integrators give a large gain boost

TJ011-A3 Parameter Ranges	
Proportional Gain	-50 to 20 dB
PI1	15 kHz to 7 MHz
PI2	20 kHz to 10 MHz
D	20 kHz to 10 MHz
Lead Span	×3.2 to ×10 (trimpot)
DC Gain	20 to 1000 (trimpot)

Table B.1: Ranges for setting for the JILA TJ011-A3 high speed loop filter.

at low frequencies but also cause a 90° phase lag. Differentiators cause a 90° phase advance and are usually used to correct for some loss of phase margin at high frequency. One of the most common problems for a feedback loop is when the feedback crosses unity gain with two integrators, and therefore a 180° phase shift, causing the loop to go into positive feedback and oscillate out of control.

For reference, the high speed JILA-built loop filters most commonly used in the Thompson lab have transfer functions decided by various frequency corners that are represented below in Fig. B.2. Corner freqeuncies are set by the PI1, PI2, DC gain, D, and Lead span settings. In the TJ011-A3 (most recent) version of the JILA high speed loop filters, the loop filter settings can be adjusted by the amount shown in Table B.1. The DC gain limitation on the integrators can be engaged (using a jumper) on one or two of the integrators. importantly, since real systems of lasers and electronics also have their own transfer functions, in order to predict the performance of a feedback loop one must multiply $L^*(\omega)$ times the gain of the rest of the system.

B.3 Example: beatnote lock between 2 lasers

As a specific example of a feedback loop in our lab, consider the most common application: phase locking two lasers together with an offset frequency. This is performed using a Hittite HMC440 phase freqeuncy detector (PFD) that is sensitive to both frequency and phase errors between the two lasers. When viewed as freqeuncy feedback, the phase detection can be viewed as an additional integrator in the system that integrates frequency errors into phase errros. For this reason, often only one integrator is necessary to achieve a high quality phase lock between
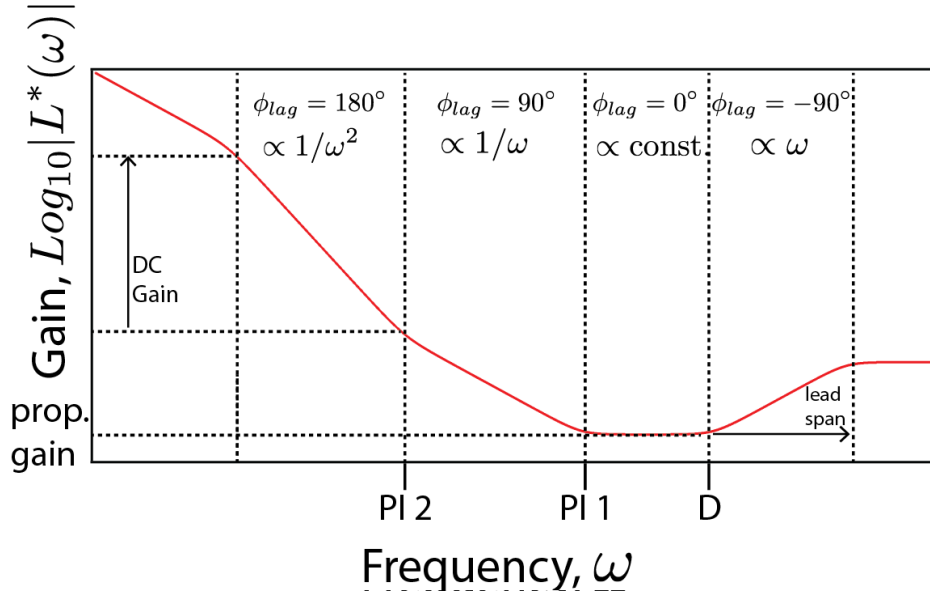
Figure B.2: Transfer function parameters of JILA high speed loop filters. The gain profile $L^*(\omega)$ is designed to have high gain at low frequencies and then can be optimized to achieve the highest feedback bandwidth on the system without losing phase margin.

the two lasers. The feedback settings for an example laser beatnote phase lock are shown in Table B.2. The resulting power spectrum of interference between the two laser, as normally viewed on a spectrum analyzer in the lab, is shown in Fig. B.3. The feedback is seen to effectively remove power from the background Lorentzian power-spectrum between the two lasers and concentrate the majority of the power within a phase-locked carrier that appears as a delta function on the center of the spectrum analyzer. The approximate unity gain frequency of 1 MHz is seen as the location of the "shoulders" of the phase lock. The fact that these shoulders do not peak strongly indicates sufficient phase margin at the unity gain freqeuncy.

As an additional note, one observed difficulty in setting up phase locks using the HMC440 PFDs is the need for high signal to noise in the phase frequency detector. Empirically we observe that greater than 40 dB of signal to noise between the carrier and the noise floor (measured in a 3MHz spectrum anaylzer bandwidth), is usually needed for high quality phase lock.

Example Beatnote Lock Settings

G1	0 dB
G2	−10 dB
PI1	150 kHz
PI2	Off
D	100 kHz

Table B.2: Example settings for a beatnote lock. The additional parameters DC gain and lead span are continuously adjusted using potentiometers. For this setup they were tuned near their maximum values.
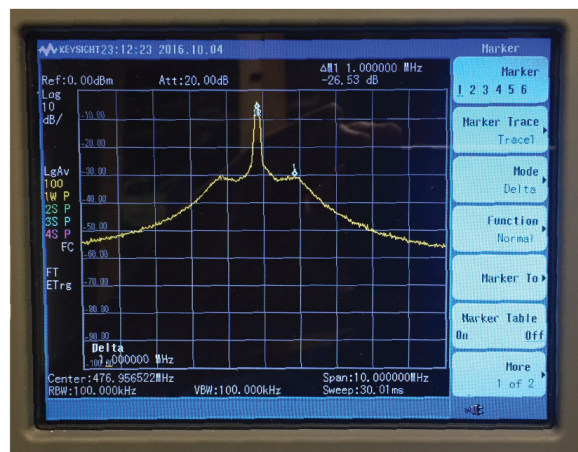

Figure B.3: Power spectrum of interference between two beatnote-locked lasers as normally viewed on a spectrum analyzer and taking 100 averages. The majority of the laser power resides in a phased-locked carrier that appears as a delta function in the power spectrum. The unity gain bandwidth is indicated by the shoulders of the distributition, measured with markers to be 1 MHz away from the carrier.